CHALMERS
UNIVERSITY OF TECHNOLOGY

CNG-Electric Hybrid Powertrain for Light Commercial Vehicle

A Technical Evaluation of CNG Internal Combustion Engine, CNG-Electric Hybrid Series and Parallel Powertrains

Master's Thesis 2025

Shashank Chikmagalur Yogeshkumar

Akash Jagadish Kamini

Department of Mechanics and Maritime Sciences

Chalmers University of Technology

Gothenburg, Sweden 2025

Master's Thesis 2025

A Technical Evaluation of CNG Internal Combustion Engine, CNG-Electric Hybrid Series and Parallel Powertrains

Shashank Chikmagalur Yogeshkumar
Akash Jagadish Kamini

CHALMERS
UNIVERSITY OF TECHNOLOGY

Department of Mechanics and Maritime Sciences
Chalmers University of Technology
Gothenburg, Sweden 2025

CNG-Electric Hybrid Powertrain for Light Commercial Vehicle
A Technical Evaluation of CNG Internal Combustion Engine, CNG-Electric Hybrid Series and Parallel Powertrains

Examiner: Prof. Peter Dahlander, Department of Mechanics and Maritime Sciences
Supervisor: Emma Grunditz, Researcher, Department of Electrical Engineering

Master's Thesis 2025

Department of Mechanics and Maritime Sciences

Chalmers University of Technology

SE-412 96 Gothenburg

Telephone +46 31 772 1000

Cover: Illustration of a van representing the selected Light Commercial Vehicle (LCV) used as the model for powertrain design. The image was created using an image editor for conceptual visualization purposes.

Abstract

This master's thesis presents a comprehensive technical evaluation of Compressed Natural Gas (CNG)-electric hybrid powertrains for Light Commercial Vehicles (LCVs), addressing the critical challenge of sustainable urban logistics through advanced simulation and control strategy analysis. Using Siemens Simcenter Amesim, three powertrain architectures conventional CNG Internal Combustion Engine (ICE), series hybrid, and parallel hybrid are rigorously compared across standardized Worldwide Harmonized Light Vehicles Test Cycle (WLTC) and Real Driving Emissions (RDE) cycles, as well as dynamic performance tests.

The study integrates sophisticated component models including a Mean Value Engine Model (MVEM) for the CNG engine, Permanent Magnet Synchronous Motors (PMSMs) with Field-Oriented Control, and an Equivalent Consumption Minimization Strategy (ECMS) for real-time energy management. Battery State of Charge (SoC) windows are optimized for each configuration: 55–65% for series hybrids (minimizing degradation) and 20–65% for parallel hybrids (maximizing electric range). Three-Way Catalytic Converters (3WCC) and regenerative braking systems are incorporated to enhance emissions reduction and energy recovery.

Results demonstrate that the parallel hybrid configuration achieves superior overall performance, delivering 18–28% fuel savings (4.15–5.89 kg/100 km) and 23–28% CO_2 reduction (89.8–126.7 g/km) compared to the conventional ICE baseline, while maintaining robust dynamic performance (0–100 km/h in 12.0 s). The series hybrid excels in acceleration response (7.78 s) and achieves 70% CO reduction under steady-state RDE operation through constant-speed generator operation at peak efficiency (38% brake thermal efficiency). However, elevated CO emissions across all configurations (15–26 g/km, exceeding Euro 6 limits) highlight the need for enhanced aftertreatment strategies, specifically secondary air injection systems.

The parallel hybrid emerges as the optimal near-term solution for mixed-duty LCV operations, combining direct mechanical coupling, adaptive ECMS control (average power split ratio 0.67), and effective regenerative braking (approximately 15% energy recovery) to achieve the lowest load sensitivity and most balanced efficiency-performance trade-off.

This work provides actionable insights for fleet operators, policymakers, and automotive engineers pursuing sustainable LCV electrification strategies. With targeted improvements including enhanced aftertreatment, machine learning-augmented ECMS, and optimized battery sizing through probabilistic modeling CNG-electric hybrids demonstrate potential for improved total emission reductions, positioning them as viable bridge technologies supporting EU Green Deal objectives and enabling decarbonized urban logistics by 2030.

Keywords: Battery Electric Vehicle, Compressed Natural Gas, Electric Hybrid, Emissions Reduction, Equivalent Consumption Minimization Strategy, Fuel Consumption, Light Commercial Vehicle, Parallel Hybrid, Regenerative Braking, Series Hybrid, Internal Combustion Engine, Energy Management

Acknowledgements

We would like to express our sincere gratitude to our examiner and supervisor,Prof. Peter Dahlander, for his invaluable guidance, encouragement, and insightful feedback throughout this thesis. His expertise and constructive input have been essential in shaping the work and bringing it to completion.

Our heartfelt thanks also go to our supervisor, Emma Grunditz, for her continuous support and for sharing her knowledge in the field of electrical engineering. Her patience, clarity, and practical advice have been of great help whenever we faced challenges during the project.

We are grateful to the Department of Mechanics and Maritime Sciences at Chalmers University of Technology for providing the necessary resources, facilities, and an inspiring academic environment in which this thesis could be carried out.

Last but not least, we owe our deepest gratitude to our families and friends. Their unwavering encouragement, understanding, and ability to remind us of what truly matters in life have been our greatest source of motivation and balance throughout this journey.

Shashank Chikmagalur Yogeshkumar, Akash Jagadish Kamini
Gothenburg,2025

List of Acronyms

LCV	Light Commercial Vehicle
HEV	Hybrid Electric Vehicle
CNG	Compressed Natural Gas
ICE	Internal Combustion Engine
ECU	Engine Control Unit
EM	Electric Motor
MVEM	Mean Value Engine Model
LHV	Lower Heating Value
ECMS	Equivalent Consumption Minimization Strategy
SoC	State of Charge
PMSM	Permanent Magnet Synchronous Motor
FOC	Field-Oriented Control
WLTC	Worldwide Harmonized Light Vehicles Test Cycle
FTP	Federal Test Procedure
RDE	Real Driving Emissions

Contents

List of Acronyms viii

1 Introduction 1
- 1.1 Background . . . 1
- 1.2 Problem Statement . . . 4
- 1.3 Objectives of the Study . . . 4
- 1.4 Delimitations . . . 4

2 Theory 5
- 2.1 Powertrain Configurations . . . 5
  - 2.1.1 Conventional ICE Powertrain . . . 5
  - 2.1.2 Series and Parallel Hybrid Powertrain Configurations . . . 6
- 2.2 Powertrain Components . . . 9
  - 2.2.1 Mean Value Engine Model (MVEM) . . . 9
    - 2.2.1.1 Torque Calculations . . . 9
    - 2.2.1.2 Efficiency Metrics . . . 10
    - 2.2.1.3 Air and Fuel Flow Dynamics . . . 12
    - 2.2.1.4 Specific Fuel Consumption . . . 13
  - 2.2.2 Electric Machine . . . 13
  - 2.2.3 Modeling of Lithium-Ion Batteries . . . 17
    - 2.2.3.1 Model Simplification for Drive Cycle Simulation . . . 18
  - 2.2.4 Modeling of Inverter . . . 19
    - 2.2.4.1 Voltage Modulation . . . 19
    - 2.2.4.2 Power Relationships . . . 19
    - 2.2.4.3 Semiconductor-Based Power Loss Model . . . 20
    - 2.2.4.4 Temperature Dependence . . . 20
    - 2.2.4.5 Switching Losses . . . 21
    - 2.2.4.6 Total Inverter Losses . . . 21
    - 2.2.4.7 Parallel Device Configuration . . . 21
  - 2.2.5 Transmission . . . 21
  - 2.2.6 Exhaust System . . . 22
- 2.3 Drive System Modeling and Selection for Light Commercial Vehicles . 23

2.4 Control Strategies for Hybrid Vehicles . . . 25
2.5 Drive Cycles . . . 27
2.5.1 Worldwide Harmonized Light Vehicles Test Cycle (WLTC) . . . 27
2.5.2 Real Driving Emissions (RDE) . . . 28
2.6 Performance Tests . . . 29
2.6.1 Acceleration Time . . . 29
2.6.2 Top Speed Test . . . 30

3 Methodology **31**
3.1 Components and its Parameters . . . 31
3.1.1 Driver Model Configuration . . . 31
3.1.2 Vehicle Dynamics Model . . . 32
3.1.3 Gearbox/Transmission Model . . . 33
3.1.4 Engine Model . . . 34
3.1.5 Exhaust System . . . 36
3.1.6 Inverter Model . . . 36
3.1.6.1 Modulation Strategy . . . 36
3.1.6.2 Device Technology Selection . . . 37
3.1.6.3 Device Configuration and Parameter Calculation . . . 37
3.1.6.4 Reference Current Justification . . . 38
3.1.6.5 Switching Loss Energy . . . 38
3.1.6.6 Implemented Parameters . . . 39
3.1.7 Electric Machine Model . . . 39
3.2 Field-Oriented Control Subsystem for Electric Machines . . . 41
3.3 Mass Configuration and Payload Standardization . . . 42
3.4 Battery Sizing for Hybrid Configurations . . . 43
3.4.1 Battery Cell Specification and Electrical Model . . . 43
3.4.1.1 Open Circuit Voltage Model . . . 43
3.4.1.2 Battery Electrical Model . . . 43
3.4.2 Series Hybrid Battery Sizing . . . 44
3.4.2.1 Sizing Methodology . . . 44
3.4.2.2 State of Charge Window . . . 45
3.4.3 Parallel Hybrid Battery Sizing . . . 45
3.4.3.1 Sizing Methodology . . . 45
3.4.3.2 State of Charge Window . . . 46
3.5 Simulation Setup . . . 47
3.5.1 Conventional CNG Model . . . 47
3.5.2 Series Hybrid Model . . . 49
3.5.3 Parallel Hybrid Model . . . 52

4 Results **55**
4.1 Conventional ICE . . . 55
4.1.1 Engine Analysis . . . 57
4.1.2 Transmission Control . . . 61
4.1.3 Fuel Consumption Analysis . . . 61
4.1.4 Emissions Performance . . . 63
4.1.5 Performance Test . . . 66

4.2 Series Hybrid . . . 69
4.2.1 Engine Analysis . . . 70
4.2.2 Electric Machine Analysis . . . 71
4.2.3 Battery SOC Analysis . . . 73
4.2.4 Fuel Consumption Analysis . . . 74
4.2.5 Emissions Performance . . . 76
4.2.6 Performance Test . . . 80
4.3 Parallel Hybrid . . . 83
4.3.1 Power Distribution . . . 83
4.3.2 Engine Analysis . . . 84
4.3.3 Electric Machine Analysis . . . 85
4.3.4 Battery SOC Analysis . . . 87
4.3.5 Transmission Control . . . 89
4.3.6 Fuel Consumption Analysis . . . 89
4.3.7 Emissions Performance . . . 91
4.3.8 Performance Test . . . 94

5 Discussion and Conclusions **97**
5.1 Fuel Consumption . . . 97
5.2 Emissions (CO, CO_2, and NO_x) . . . 98
5.3 Dynamic Performance . . . 99
5.4 Energy Management . . . 100
5.5 Overall Trends and Configuration Comparison . . . 102
5.6 Advantages and Drawbacks . . . 102
5.7 Best Powertrain Selection . . . 104
5.8 Comparison with Real-World Examples . . . 104
5.9 Future Optimization Recommendations . . . 106
5.10 Conclusions . . . 108

A Supplementary Data **109**
A.1 Power Profiles for different powertrain during acceleration test . . . 109

Bibliography **113**

1

Introduction

1.1 Background

Light Commercial Vehicles (LCVs) are specialized vehicles designed for efficient transport of goods and services in urban, suburban, and regional environments. These vehicles are integral to global logistics, e-commerce, and small business operations. The transport sector as a whole accounts for approximately 29% of global carbon dioxide (CO_2) emissions from energy sources, and LCVs represent a significant portion of these emissions within the road transport category. This underscores the need for sustainable solutions to reduce their environmental impact [1, 2]. The rapid growth of e-commerce and urbanization has heightened demand for LCVs that optimize fuel efficiency, minimize emissions, and perform reliably across diverse conditions, including urban stop-and-go traffic, highway operations, and rural variable-terrain routes [3].

Widely utilized LCV models, such as the Ford Transit, Mercedes-Benz Sprinter, Volkswagen Transporter, and Renault Kangoo, are valued for their versatility, spacious cargo capacity, modular configurations, and maneuverability. Predominantly powered by conventional internal combustion engines (ICEs) using diesel or gasoline, these vehicles reflect the market's dependence on fossil fuels, yet present opportunities for adopting hybrid systems and alternative fuels to meet stringent regulatory and environmental requirements.

Compressed Natural Gas (CNG), including renewable biomethane, offers significant environmental, economic, and operational benefits compared to conventional liquid fuels for light commercial vehicles (LCVs). Primarily composed of methane (CH_4) with typical purity above 90%, CNG exhibits a high research octane number (RON) of approximately 120, which allows higher compression ratios and improved thermal efficiency in spark-ignited engines [4]. Stored at pressures of 200–250 bar, CNG possesses a lower volumetric energy density (about 9 MJ/L) than gasoline (about

32–35 MJ/L), necessitating larger storage tanks, but it provides a higher gravimetric energy content (about 50–55 MJ/kg), which helps offset this limitation when optimized for weight [5, 6].

CNG elevated autoignition temperature (540–600 °C) and relatively narrow flammability limits (4.4–15% by volume in air) enhance operational safety, reducing the risk of unintentional ignition. Its gaseous form and low density (0.65–0.72 kg/m^3) allow rapid dispersion in the event of leaks, unlike denser liquid fuels [7, 8]. In tank-to-wheel (TTW) terms, methane combustion emits approximately 50–56 g CO_2/MJ compared to 70–75 g CO_2/MJ for gasoline representing a 20–25% reduction in CO_2 emissions per unit of delivered energy [3, 5, 9, 10]. CNG engines also typically produce substantially lower particulate matter (PM) mass and particle number emissions often more than 80–90% lower than diesel while nitrogen oxides (NO_x) levels are generally reduced, depending on engine and aftertreatment configuration [9, 10, 11].

Economically, CNG continues to provide meaningful operating cost advantages. According to the European Alternative Fuels Observatory (EAFO), average CNG fuel costs across EU countries are approximately Euro 5–9 per 100 km, compared with Euro 7–13 for gasoline vehicles, resulting in savings of up to 40–50% depending on regional pricing and tax structures [16]. Renewable biomethane, produced via anaerobic digestion of organic waste, further improves the carbon profile, with global production estimated around 9–12 billion m^3 in recent years and an EU growth target of 35 billion m^3/year by 2030 [12, 13, 14].

Property	**CNG**	**Gasoline**	**Units**
Main composition	CH_4 ($\geq$90%)	C_5–C_{12} hydrocarbons	–
Octane rating (RON)	$\approx$120	87–95	–
Energy density (volumetric)	9.0–9.2	32–35	MJ/L
Energy content (gravimetric)	50–55	44–46	MJ/kg
Autoignition temperature	540–600	250–400	°C
Flammability range	4.4–15	1–7.6	vol.% in air
Density at STP	0.65–0.72	720–760	kg/m^3
CO_2 emissions (TTW)	50–56	70–75	g/MJ

Table 1.1: Tank-to-wheel (TTW) comparison of key fuel properties for CNG and gasoline in vehicular applications.

Biomethane compatible infrastructure, shared with existing natural gas networks, and potential integration with hybrid-electric powertrains make CNG a technically and economically viable transition fuel for LCV fleets striving for reduced operating

costs and compliance with stringent Euro 6 and forthcoming Euro 7 standards.

However, CNG adoption is not without challenges. The lower volumetric energy density requires larger, heavier storage cylinders (typically 50–100 kg for 20–30 kg CNG capacity), reducing payload capacity by 5%–15% compared to diesel equivalents and increasing vehicle curb weight by 100–200 kg [6, 8]. CNG engines exhibit 10%–20% lower power output due to reduced volumetric efficiency from gaseous fuel induction, necessitating engine sizing adjustments that impact vehicle dynamics [4, 10]. Initial vehicle costs are 15%–25% higher due to specialized components, though lifecycle savings typically recover this premium within 30,000–50,000 km for fleet operators [3, 6].

Despite these benefits and challenges, research on CNG-electric hybrid powertrains tailored for LCVs remains limited. While hybrid technologies have been extensively studied for heavier vehicles like buses, light-duty applications combining CNG's low-emission profile with electric efficiency under mixed driving conditions are underexplored [23, 24]. This study aims to address these gaps, informing policymakers and industry stakeholders on sustainable powertrain solutions for LCVs.

CNG-electric hybrid powertrains combine CNG's environmental benefits with electric propulsion efficiency, offering a promising approach to enhance performance and sustainability across diverse LCV operating scenarios, positioning CNG as a bridge fuel in the transition to low-carbon mobility.

For our study, we have selected Siemens Simcenter AMESim, a robust multi-domain simulation platform that enables detailed modeling of mechanical, electrical, and thermal interactions in hybrid powertrains, including fuel-specific behaviors like those of CNG across standardized drive cycles such as WLTC and real-world conditions like RDE [29]. The integration of all the platform libraries supports the analysis of various configurations including series, parallel, and conventional ICE while accurately capturing transient behaviors for different drive cycles.

AMESim's modular framework enables comprehensive evaluation of fuel consumption, emissions, and performance critical for hybrid powertrain analysis. Compared to MATLAB Simscape, which demands extensive customization for multi-domain modeling despite strengths in control design, or AVL CRUISE, which lacks flexibility for custom configurations, AMESim offers a balanced integration of automotive-specific tools and multi-physics simulation [25, 26]. Its computational rigor supports detailed analysis of LCV powertrains, ensuring accurate performance and emissions assessments [27, 28].

1.2 Problem Statement

The foremost challenge for LCVs is to achieve optimal fuel efficiency and minimal emissions across a spectrum of operating conditions, encompassing urban stop-and-go traffic, highway cruising, and rural routes with variable terrains. Conventional ICE vehicles, dependent on petroleum-based fuels, demonstrate reduced efficiency in urban environments due to suboptimal low-speed performance, resulting in elevated fuel consumption and emissions [7]. Existing hybrid powertrains, which integrate ICE and electric motor technologies, often lack comprehensive evaluation tailored to the specific demands of LCVs, such as mixed driving profiles and variable load conditions [17].

1.3 Objectives of the Study

This study seeks to design and evaluate conventional CNG engine and CNG-electric hybrid powertrains for LCVs, with a focus on optimizing performance, fuel efficiency, and emissions reduction across urban, highway, and rural routes with variable terrains. Utilizing Siemens Simcenter AMESim, the research compares conventional ICE configuration, series, and parallel hybrid architectures. The specific objectives are as follows:

1. Selection of the components for the design of three powertrain configurations and capture their dynamic behaviors.
2. To conduct parametric tuning to determine the optimal parameter settings for a fixed powertrain configuration within the AMESim environment.
3. To evaluate the adaptability of these powertrains to a range of operating conditions.
4. To assess engine control strategies for the ICE powertrain and Equivalent Consumption Minimization Strategy (ECMS) supervisors for hybrid powertrains, quantifying fuel consumption and CO/NO_x emissions using standardized drive cycles.
5. To identify the most effective powertrain based on performance metrics across varying conditions and standardized cycles.

1.4 Delimitations

This study is subject to the following constraints:

1. Limitation to one standard driving cycle and one real-world driving cycle, excluding extreme off-road scenarios.
2. Restriction to the evaluation of only two control algorithms.
3. Exclusion of a detailed cost analysis, with emphasis placed on technical performance and emissions; economic feasibility is deferred for future investigation.

2

Theory

This chapter establishes the theoretical foundation for a Compressed Natural Gas (CNG)-electric hybrid powertrain, addressing CNG engine modeling, battery and electric motor modeling parameters, energy management strategies, torque calculation techniques, and efficiency maps. This groundwork underpins the simulation framework detailed in Chapter 3 [27, 7, 18].

2.1 Powertrain Configurations

Powertrain configurations determine the mechanisms for power generation and transmission to the wheels, significantly impacting the performance and emissions profiles of light commercial vehicles (LCVs). This section examines three primary configurations: Conventional Internal Combustion Engine (ICE), Series Hybrid, and Parallel Hybrid. Each configuration exhibits unique characteristics in efficiency, control complexity, and adaptability to diverse driving conditions, with a comparative analysis presented in Table 2.1.

2.1.1 Conventional ICE Powertrain

The conventional internal combustion engine (ICE) powertrain represents the foundational architecture for propulsion in light commercial vehicles (LCVs), particularly those adapted for compressed natural gas (CNG) as a fuel source. In this configuration, a CNG-fueled (ICE) serves as the primary energy converter, transforming chemical energy from CNG combustion into mechanical work, which is subsequently delivered as torque to the drive wheels via a mechanical transmission system. This direct drive approach, illustrated in Figure 2.1, relying solely on the engine's output to meet vehicle demands across diverse operating conditions. At its core, the CNG ICE operates on the principles of spark-ignition internal combustion, Similar to a gasoline engine but optimized for gaseous fuel. CNG, primarily composed of methane (CH_4, >90% by volume), is stored in high-pressure cylinders (typically 200–250 bar) and regulated to engine intake pressures (approximately 5–10 bar). The combustion

process follows the Otto cycle, comprising four strokes: intake, compression, power, and exhaust. During the intake stroke, a controlled air–CNG mixture (air-fuel ratio ≈ 14.5:1 for stoichiometric combustion) enters the cylinders. Compression (compression ratio 10:1–12:1) raises the mixture temperature, followed by spark ignition to initiate rapid exothermic combustion,represented by the reaction:

$$CH_4 + 2O_2 \rightarrow CO_2 + 2H_2O + \text{heat} \tag{2.1}$$

The expansion of combustion gases drives the piston, generating reciprocating motion that is converted to rotary torque via the crankshaft. Owing to CNG's high octane rating , higher compression ratios than gasoline engines are achievable while mitigating knock.

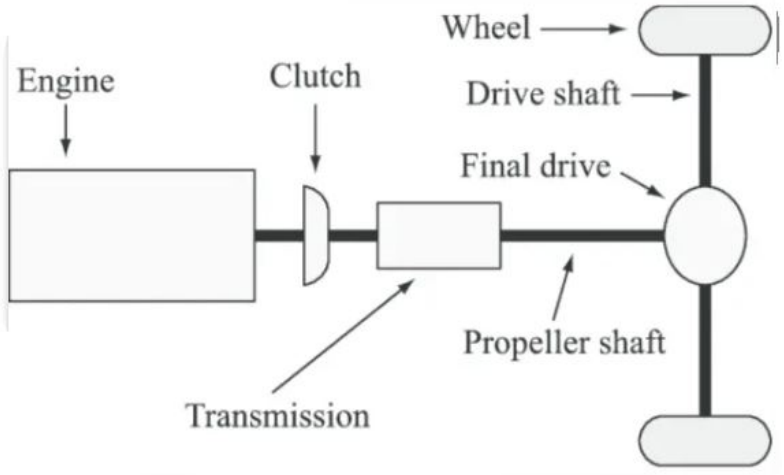

Figure 2.1: Schematic of Conventional ICE Powertrain Configuration

2.1.2 Series and Parallel Hybrid Powertrain Configurations

Hybrid powertrain configurations for LCVs include series and parallel architectures, each characterized by distinct power generation and transmission mechanisms. In the series hybrid configuration, the CNG internal combustion engine (ICE) is mechanically decoupled from the drivetrain, as depicted in Figure 2.2. The ICE drives a generator to produce electrical energy, which powers one electric motors (EMs) to propel the wheels. This design allows the ICE to operate at optimal efficiency points, independent of vehicle speed, enhancing performance under variable load conditions. Regenerative braking recovers kinetic energy, though multiple energy conversion stages (mechanical to electrical to mechanical) may reduce efficiency during prolonged high-speed operation [30]. In the parallel hybrid configuration, power is delivered to the wheels by the ICE, EM, or both via a shared mechanical linkage, such as a transmission or gearbox, as shown in Figure 2.3. This architecture offers operational flexibility, with the ICE dominating during high-speed highway driving and the EM enhancing efficiency in low-speed or stop-and-go scenarios. Power-split control introduces moderate complexity compared to series hybrids, requiring advanced coordination, yet it adapts effectively across diverse driving cycles. Industry standards

classify parallel hybrid designs into P0–P4 categories based on the positioning and coupling of the EM and ICE [27]. Architecturally, series hybrids rely on an electrical power path, converting ICE mechanical energy into electricity via a generator. This introduces conversion losses but ensures smooth torque delivery and enhanced regenerative braking efficiency (typically 60%–70%), making them suitable for urban environments with frequent start-stop cycles, such as LCV delivery operations [31, 32]. Parallel hybrids offer dual power paths mechanical and electrical enabling direct torque transmission from the ICE, minimizing energy losses under specific conditions. They achieve High efficiencies with EM assistance due to reduced conversion penalties, though they may engage the ICE more frequently. Control system requirements reflect these architectural differences. Series hybrids demand moderate control complexity, focusing on generator–battery–EM coordination to maintain battery state-of-charge (SoC) and optimize energy distribution [31]. Parallel hybrids require sophisticated control strategies to manage power splitting, clutch engagement, and seamless blending of ICE and EM outputs, increasing system intricacy [33].

Types	Features	Modes	Power Paths
Series hybrid	Driving force provided only by motor	Electric drive	
		Working of engine and motor	
		Energy recovery	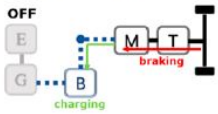

Figure 2.2: Schematic Representation of Series Hybrid Configuration

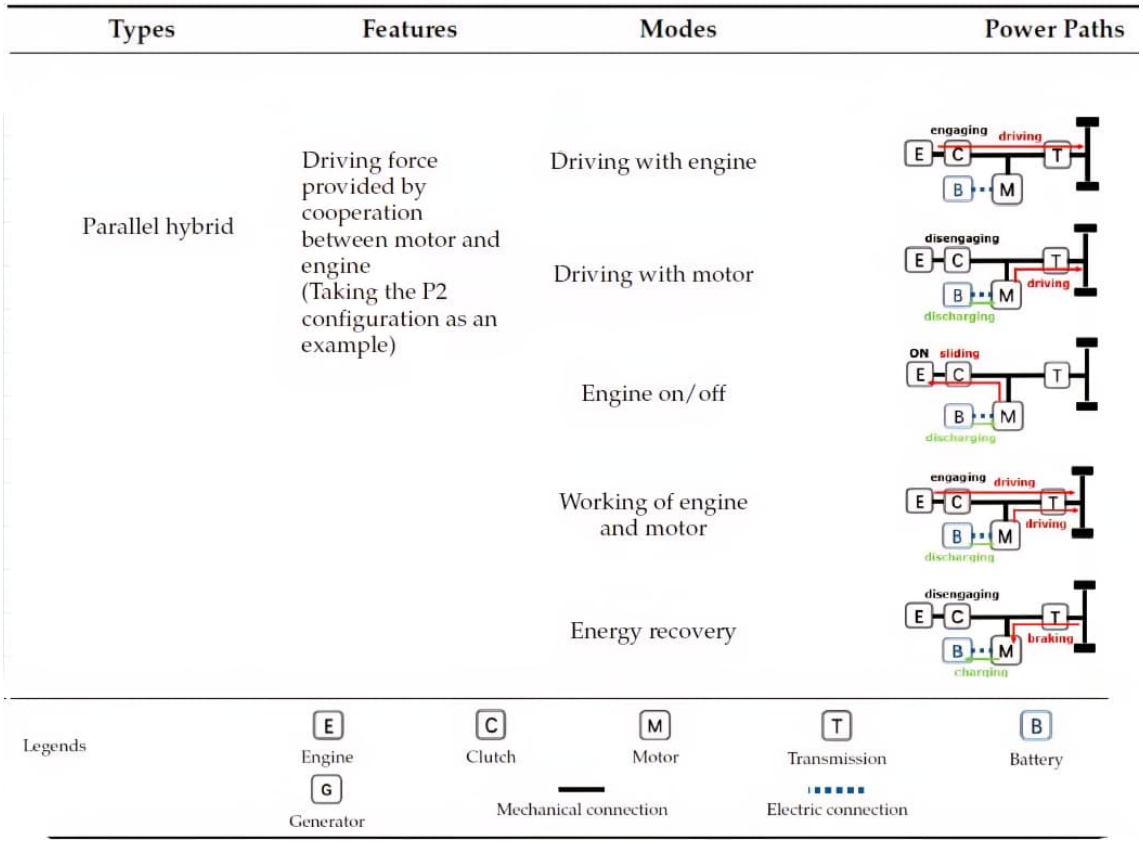

Figure 2.3: Schematic Representation of Parallel Hybrid Configuration

Table 2.1: Comparative Analysis of Series and Parallel Hybrid Powertrains for LCVs

Characteristic	**Series Hybrid**	**Parallel Hybrid**
Architecture	ICE-driven generator powers EM for wheel propulsion	ICE and/or EM drive wheels via gearbox
Power Transmission	Electrical path exclusively	Mechanical and/or electrical paths
Efficiency	60%–70% (urban, regenerative focus)	70%–90% (variable, load-dependent)
Control Complexity	Moderate (generator–battery–EM coordination)	High (torque splitting and blending)
Urban Performance	60%–70% (optimized for stop–go cycles)	70%–80% (EM-assisted efficiency)
Highway Performance	60%–70% (conversion-limited)	85%–90% (mechanical drive dominant)
Load Adaptability	EM-based power allocation	Direct torque integration

2.2 Powertrain Components

The powertrain integrates components responsible for generating and delivering torque to the vehicle's wheels, including the engine, transmission, clutch, driveshaft, electric machine, and energy storage system. These elements are engineered to enhance performance and efficiency in hybrid LCV applications, as detailed below.

2.2.1 Mean Value Engine Model (MVEM)

The Mean Value Engine Model (MVEM) simplifies engine dynamics by averaging in-cylinder properties over a cycle, striking a balance between computational efficiency and accuracy for hybrid powertrain simulations. This model captures critical performance metrics, including torque production, fuel consumption, and efficiency parameters, through lookup tables derived from experimental dynamometer testing . The MVEM's ability to deliver real-time data makes it well-suited for control system design and system-level analysis in hybrid light commercial vehicles (LCVs), where rapid adaptation to varying loads is critical [27].

2.2.1.1 Torque Calculations

The indicated torque ($T_{\text{ind}}(t)$, N m) is computed as:

$$T_{\text{ind}}(t) = \frac{E_{\text{indicated}}(t) \cdot \frac{N(t)}{120} - W_{\text{pump}}(t) - W_{\text{loss}}(t)}{N(t) \cdot \frac{2\pi}{60}}, \tag{2.2}$$

where:

- $E_{\text{indicated}}(t) = p_{\text{imep}}(t) \cdot V_{\text{cyl}}$ (J), with $p_{\text{imep}}(t)$ (Pa) as the indicated mean effective pressure and $V_{\text{cyl}} = 0.449\,\text{L}$ as the per-cylinder displacement volume,
- $N(t)$ (rad/s) represents engine speed, with a stall speed of 1.047 rad/s (10 RPM),
- $W_{\text{pump}}(t) = \frac{N(t) \cdot V_{\text{cyl}} \cdot (p_{\text{exhaust}}(t) - p_{\text{intake}}(t))}{120} \cdot \eta_{\text{vol}}(t)$ (J/s) accounts for pumping losses,
- $W_{\text{loss}}(t) = \eta_{\text{exh}}(t) \cdot \frac{N(t)}{120} \cdot V_{\text{cyl}} \cdot \Big(0.1 \cdot (p_{\text{exhaust}}(t) - p_{\text{intake}}(t)) + 0.35 \cdot p_{\text{intake}}(t) \cdot \frac{N(t)}{N_{\max}}\Big)$ (J/s) represents frictional and auxiliary losses.

The net engine torque ($T_e(t)$, N m) is:

$$T_e(t) = \eta_{\text{mech}} \cdot T_{\text{ind}}(t), \tag{2.3}$$

where η_{mech} (dimensionless) denotes mechanical efficiency, accounting for losses in mechanical components.

2.2.1.2 Efficiency Metrics

The CNG engine's performance is characterized by three key efficiency metrics: volumetric efficiency (η_{vol}), indicated efficiency (η_{ind}), and exhaust efficiency (η_{exh}). These metrics, derived from lookup tables based on dynamometer testing provide a comprehensive assessment of the engine's operational efficiency across various conditions, enabling precise optimization for hybrid powertrain applications.

Volumetric Efficiency Volumetric efficiency (η_{vol}, dimensionless) quantifies the engine's ability to induct air into the cylinders relative to its theoretical maximum capacity:

$$\eta_{\text{vol}} = \frac{120 \cdot Q_{\text{intake}}}{N \cdot V_d \cdot \rho_{\text{intake}}}, \tag{2.4}$$

where Q_{intake} (kg/s) is the intake air mass flow rate, $V_d = 1.796\,\text{L}$ is the total engine displacement, and $\rho_{\text{intake}} = 1.226\,\text{kg/m}^3$ is the intake air density at 20 °C. A representative value is $\eta_{\text{vol}} = 0.85$ at an intake manifold pressure (p_{im}) of 1.5 bar and engine speed (N) of 209.44 rad/s (2000 RPM). The volumetric efficiency map, with intake manifold pressure (p_{im}, bar) on the x-axis, engine speed (N, rad/s) on the y-axis, and η_{vol} (dimensionless) on the z-axis, is generated from experimental dynamometer testing or high-fidelity CFD simulations. It achieves a peak of 0.92 at $N = 209.44\,\text{rad/s}$, $p_{\text{im}} = 1.5\,\text{bar}$, reflecting optimal air induction in the mid-speed range ($N = 150\,\text{rad/s}$ to $300\,\text{rad/s}$, $p_{\text{im}} = 0.8\,\text{bar}$ to $1.5\,\text{bar}$), where η_{vol} ranges from 0.85 to 0.92, ideal for urban and highway driving. At low speeds ($N < 150\,\text{rad/s}$) and high intake pressures ($p_{\text{im}} > 1.2\,\text{bar}$), η_{vol} exceeds 0.90 due to enhanced air filling from ram effects, while at high speeds ($N > 300\,\text{rad/s}$) with low intake pressures ($p_{\text{im}} < 0.8\,\text{bar}$), it drops below 0.75 due to intake dynamics limitations.

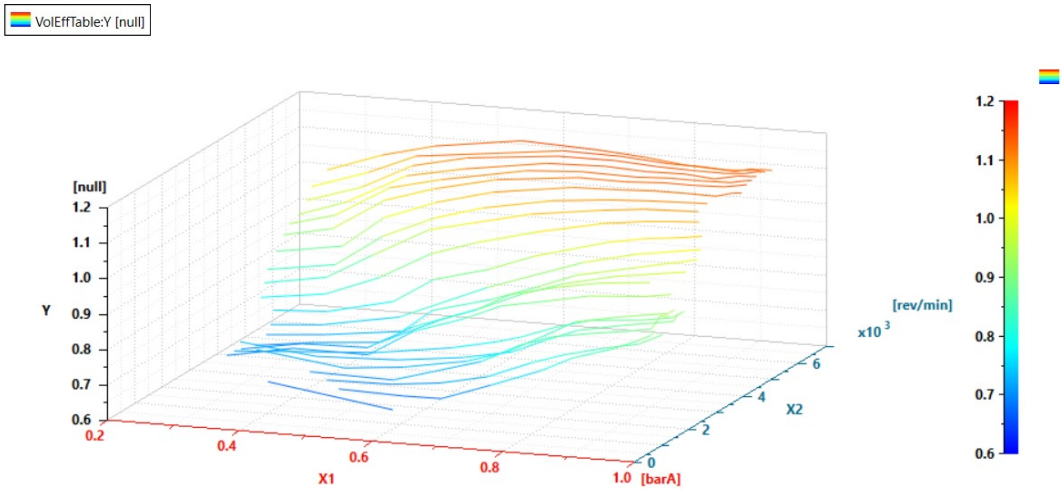

Figure 2.4: Volumetric Efficiency Lookup Table (η_{vol}, dimensionless, z-axis) vs. Engine Speed (N, rad/s, y-axis) and Intake Manifold Pressure (p_{im}, bar, x-axis)

Indicated Efficiency Indicated efficiency (η_{ind}, ranging from 0.25 to 0.35) quantifies the thermodynamic efficiency of converting fuel chemical energy into mechanical work:

$$\eta_{\text{ind}} = \frac{p_{\text{imep}} \cdot V_d \cdot N}{120 \cdot Q_{\text{fuel}} \cdot \text{LHV}}, \tag{2.5}$$

where p_{imep} (bar) is the indicated mean effective pressure, Q_{fuel} (kg/s) is the fuel mass flow rate, and LHV = 47.7 MJ/kg is the lower heating value of CNG. The indicated efficiency map, with engine load on the x-axis, engine speed (N, rad/s) on the y-axis, and η_{ind} (dimensionless) on the z-axis, is derived from dynamometer testing or CFD simulations. It peaks at 0.35 at $N = 150$ rad/s to 250 rad/s (1500–2400 RPM) under moderate to high load conditions, achieving a brake thermal efficiency of 35.2% at approximately 2000 RPM and 50% load. This "efficiency island" is a critical target for hybrid supervisory control strategies to minimize fuel consumption, with efficiency dropping to 0.25 at low loads due to throttling losses and decreasing by 5%–8% at high speeds due to increased heat transfer losses. The map's integration into the MVEM ensures precise fuel consumption predictions with high computational efficiency and accuracy validated against steady-state data across 120 operating points.

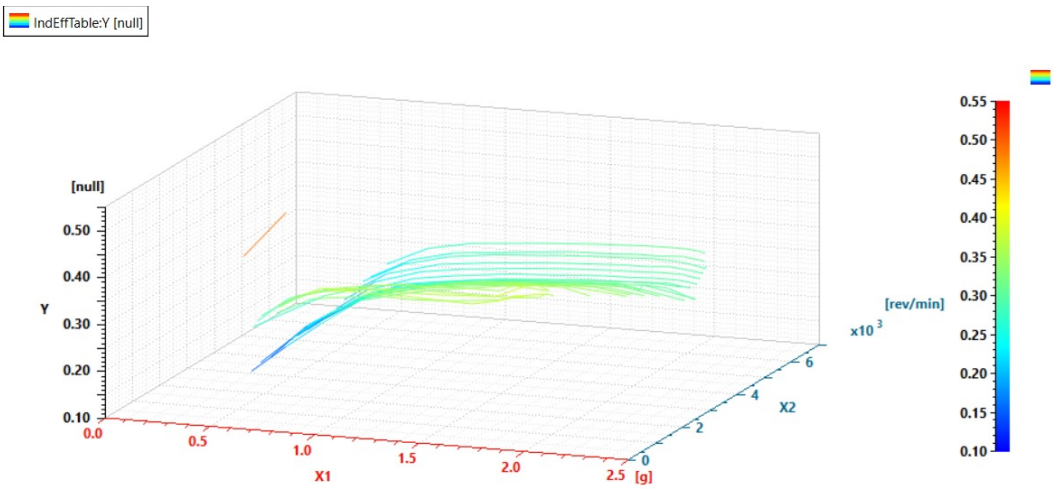

Figure 2.5: Lookup Table for Indicated Efficiency, Mapping Engine Speed (N, rad/s) on the x-axis, Brake Mean Effective Pressure (BMEP, bar) on the y-axis, and Indicated Efficiency (η_{ind}, dimensionless) on the z-axis

Exhaust Efficiency Exhaust efficiency (η_{exh}, ranging from 0.2 to 0.4) measures the proportion of fuel energy lost as exhaust gases:

$$\eta_{\text{exh}} = \frac{H_{\text{exh}} - H_{\text{im}}}{Q_{\text{fuel}} \cdot \text{LHV}}, \tag{2.6}$$

where H_{exh} and H_{im} (J/s) are the exhaust and intake enthalpy flow rates, respectively. The exhaust efficiency map, with engine load on the x-axis, engine speed (N, rad/s) on the y-axis, and η_{exh} (dimensionless) on the z-axis, is generated from

experimental data. It peaks at 0.40 at full load and 2000 RPM, corresponding to exhaust temperatures of 550–650°C, optimal for three-way catalytic converter (3WCC) light-off and sustained NOx conversion efficiency (>95% at $\lambda = 1.0$). Operating characteristics include high-load conditions ($\eta_{\text{exh}} = 0.35 - 0.40$) with elevated exhaust temperatures enhancing catalytic performance, cruise conditions ($N = 150\,\text{rad/s}$ to $250\,\text{rad/s}$, $\eta_{\text{exh}} = 0.28 - 0.32$) with moderate temperatures (450–550°C) maintaining catalytic efficiency, and idle or low-load conditions ($\eta_{\text{exh}} < 0.22$) with cooler exhaust (300–400°C), posing challenges for 3WCC light-off during cold starts. The map's integration into the MVEM, using a hierarchical lookup process with bilinear interpolation, ensures smooth transitions during transient operation, achieving computational efficiency and accuracy.

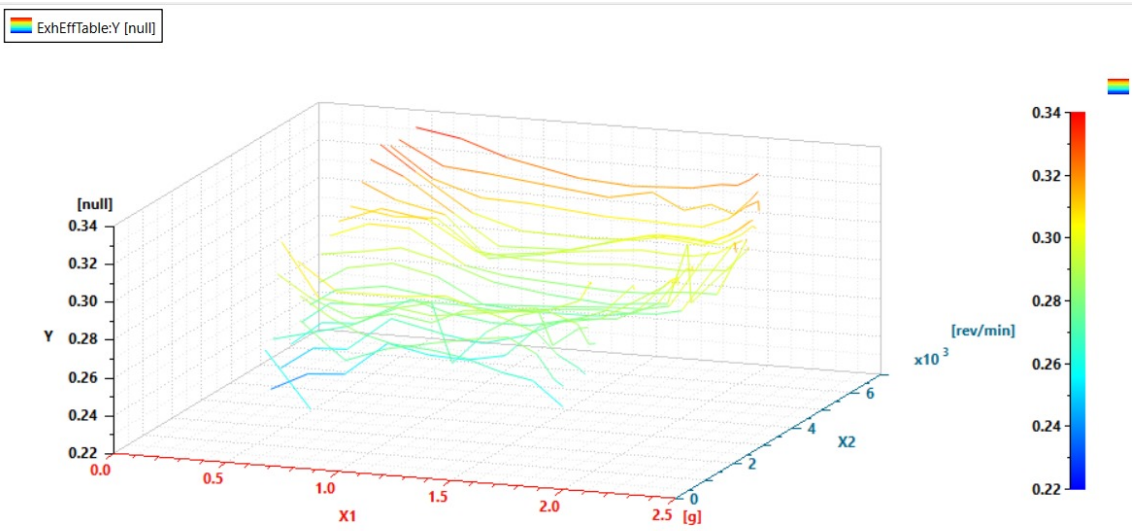

Figure 2.6: Lookup Table for Exhaust Efficiency, Mapping Engine Speed (N, rad/s) on the x-axis, Brake Mean Effective Pressure (BMEP, bar) on the y-axis, and Exhaust Efficiency (η_{exh}, dimensionless) on the z-axis

2.2.1.3 Air and Fuel Flow Dynamics

The air mass flow rate ($\dot{m}_{\text{air}}(t)$, kg/s) is calculated as:

$$\dot{m}_{\text{air}}(t) = \rho_{\text{air}} \cdot V_d \cdot \frac{N(t)}{120} \cdot \eta_{\text{vol}}(p_{\text{im}}(t), N(t)), \tag{2.7}$$

where $\rho_{\text{air}} = 1.226\,\text{kg/m}^3$ is the air density at 20 °C. The instantaneous fuel mass flow rate ($\dot{m}_{\text{fuel}}(t)$, kg/s) is:

$$\dot{m}_{\text{fuel}}(t) = \frac{\dot{m}_{\text{air}}(t)}{\lambda(t) \cdot AFR_{\text{stoich}}}, \tag{2.8}$$

where $\lambda(t)$ is the relative air-fuel ratio (typically near 1 for stoichiometric operation to optimize catalytic converter efficiency), and $AFR_{\text{stoich}} = 17.2$ is the stoichiometric

air-fuel ratio for CNG, reflecting its methane-dominated composition. Total fuel consumption over a drive cycle is:

$$m_{\text{fuel}} = \int_{t_0}^{t_f} \dot{m}_{\text{fuel}}(t)\, dt. \tag{2.9}$$

2.2.1.4 Specific Fuel Consumption

Specific fuel consumption (SFC, g/kWh) quantifies engine efficiency in terms of fuel consumed per unit of power output:

$$\text{SFC}(t) = \frac{\dot{m}_{\text{fuel}}(t) \cdot 3600}{P_e(t)}, \tag{2.10}$$

where $P_e(t)$ (kW) is the engine power output. SFC is a pivotal metric for assessing fuel economy and CO_2 emissions in engine, particularly in hybrid configurations, where it informs energy management strategies to optimize the balance between CNG engine and electric motor operation.

2.2.2 Electric Machine

The electric machine (EM), a Permanent Magnet Synchronous Motor (PMSM), serves as both a motor for propulsion and a generator for regenerative braking. Selected for its high efficiency, compact size, and high power density, the PMSM is ideal for LCVs. It generates a rotating magnetic field via three-phase stator windings, powered by an inverter, synchronized with permanent magnets in the rotor to produce torque, eliminating rotor excitation current and reducing energy losses [38, 39]. The Permanent Magnet Synchronous Machine (PMSM) considered in this study is modeled using the quasi-static component. This model assumes a balanced three-phase system and uses current space phasors as inputs. Electrical inductive dynamics are neglected, making the model suitable for steady-state or slowly varying performance studies. All electrical quantities are expressed in the d-q reference frame. The rotor relative speed, ω_{dif} [rad/s], and the electrical rotor angle, θ_e [rad], are related to the mechanical speed and the number of pole pairs p through the relations:

$$\omega_e = p \cdot \omega_{\text{dif}}, \qquad \frac{d\theta_e}{dt} = -\omega_{\text{dif}}. \tag{2.11}$$

Here, ω_e is the electrical angular speed, ω_{dif} is the rotor relative speed, θ_e is the electrical rotor angle, and p is the number of pole pairs. The machine is reversible: when ω_{dif} and the electromagnetic torque T_{em} [N m] have the same sign, the machine operates as a motor, whereas opposite signs indicate generator operation. The total stator phase resistance R_s [Ω] consists of a DC component $R_{s,\text{DC}}$, which depends on the winding temperature T_w [°C], and an AC component $R_{s,\text{AC}}$, which accounts for frequency-dependent effects such as skin and proximity effects. The DC part is calculated as:

$$R_{s,\text{DC}} = R_{\text{ref}} \cdot F_T(T_w), \qquad F_T(T_w) = 1 + \alpha_T(T_w - T_{\text{ref}}), \tag{2.12}$$

where R_{ref} [Ω] is the reference stator resistance at the reference temperature T_{ref} [°C], and α_T [1/°C] is the temperature coefficient of the conductor. The AC part can be represented either using a resistance factor depending on current, speed, and temperature:

$$R_{s,\text{AC}} = R_{\text{ref}} \cdot F_{\text{AC}}(I, \omega, T_w), \tag{2.13}$$

or derived from AC losses:

$$R_{s,\text{AC}} = \frac{P_{\text{AC}}}{I^2}, \tag{2.14}$$

where I [A] is the stator current magnitude, ω [rad/s] is the rotor speed, and P_{AC} [W] is the AC loss power. The stator flux linkages in the d-q frame, Ψ_{sd} and Ψ_{sq} [Wb], are obtained from either lookup tables and include a correction for the stator end-winding inductance l_{sew} [H]. They are computed as:

$$\Psi_{sd} = \Psi_d(\text{Isd, Isq}) + l_{\text{sew}} \cdot \text{Isd}, \qquad \Psi_{sq} = \Psi_q(\text{Isd, Isq}) + l_{\text{sew}} \cdot \text{Isq}, \tag{2.15}$$

where Isd and Isq [A] are the stator currents on the d and q axes, respectively, and Ψ_d, Ψ_q are the flux linkages obtained from the magnetic characterization tables. Assuming quasi-static electrical behavior, the stator voltages in the d-q frame are computed as:

$$U_{sd} = R_s I_{sd} - \omega_e \Psi_{sq}, \qquad U_{sq} = R_s I_{sq} + \omega_e \Psi_{sd}, \tag{2.16}$$

where U_{sd} and U_{sq} [V] are the d- and q-axis stator voltages. These voltages can then be converted into phase and line-to-neutral quantities using standard Park and Clarke transformations. The model includes machine losses. The stator copper (Joule) losses are calculated as:

$$P_{\text{copper}} = R_s \left(I_{sd}^2 + I_{sq}^2 \right), \tag{2.17}$$

where P_{copper} [W] represents the energy dissipated in the stator windings. Iron losses, P_{iron} [W], are evaluated as a function of d-q currents and rotor speed using tables or expressions:

$$P_{\text{iron}} = \delta h_{\text{iron}}(I_{sd}, I_{sq}, \omega_{\text{dif}}). \tag{2.18}$$

These iron losses are used to determine the effective currents, which represent the portion of stator current that contributes to torque production after accounting for core losses:

$$I_{d,\text{eff}} = I_{sd} - I_{c,d}, \qquad I_{q,\text{eff}} = I_{sq} - I_{c,q}, \qquad I_{c,d/q} = \frac{P_{\text{iron}}}{\omega_{\text{dif}}}. \tag{2.19}$$

Finally, the electromagnetic torque is computed using the flux linkages and effective currents, subtracting the effect of iron losses:

$$T_{\text{em}} = p \cdot (\Psi_{sd} I_{sq} - \Psi_{sq} I_{sd}) - \frac{P_{\text{iron}}}{\omega_{\text{dif}}}. \tag{2.20}$$

The first term corresponds to the torque generated by the interaction between stator flux linkages and currents, while the second term accounts for the torque reduction due to iron losses. This continuous quasi-static PMSM model therefore incorporates the effects of stator resistance (both DC and AC components), flux linkages obtained

from FEM or lookup tables, and iron losses, providing an accurate representation of machine voltage, current, torque, and efficiency under steady-state or slowly varying operating conditions.

For accurate modeling of the PMSM in hybrid powertrain simulations, lookup tables derived from experimental data are employed to capture non-linear behaviors that are challenging to express analytically. These tables enable efficient computation of key parameters such as power losses and torque limits under varying operating conditions, ensuring the model reflects real-world performance constraints. The power losses in the motor, which include copper losses, iron losses (hysteresis and eddy current), and mechanical losses (friction and windage), are mapped as a function of output torque and rotational speed. This lookup table allows for the estimation of efficiency at specific operating points, which is crucial for energy management strategies. Higher losses occur at elevated torques and speeds due to increased current demands and magnetic field interactions.

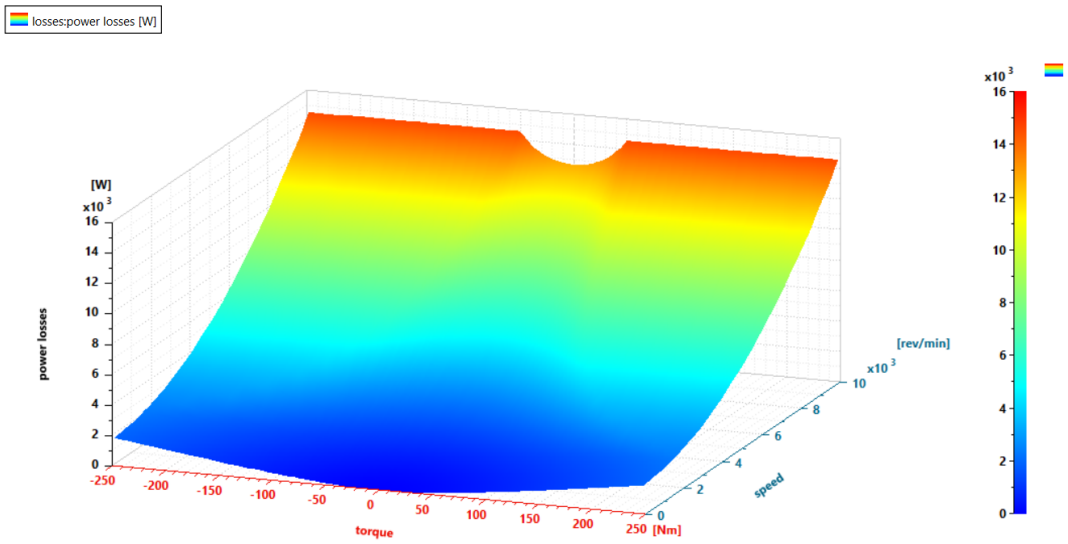

Figure 2.7: Lookup Table for Power Losses in the Motor, Mapping Torque (T, N m) on the x-axis, Speed (N, RPM) on the y-axis, and Power Losses (P_{loss}, W) on the z-axis.

The maximum torque lookup table defines the upper torque boundary of the PMSM, influenced by the DC bus voltage and motor speed. At lower speeds, torque is limited by current constraints to prevent overheating, while at higher speeds, field weakening is applied to extend the operating range, reducing available torque. Voltage variations, such as those from battery SoC fluctuations, further modulate this limit. This table is essential for determining feasible torque requests during motoring mode and preventing overcurrent conditions.

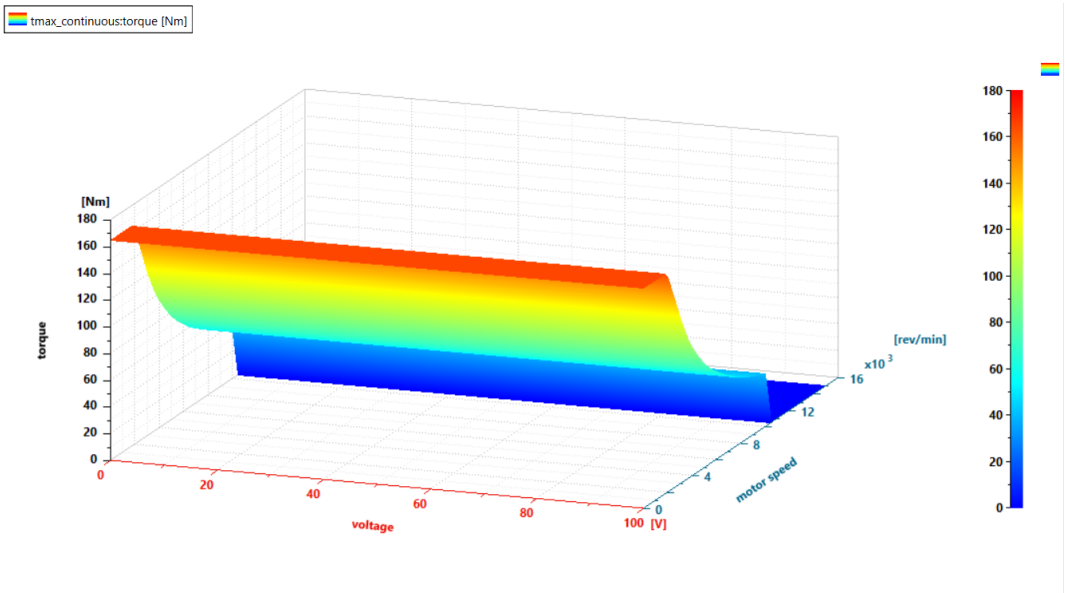

Figure 2.8: Lookup Table for Maximum Torque in the Motor, Mapping Voltage (V, V) on the x-axis, Motor Speed (N, RPM) on the y-axis, and Maximum Torque ($T_{\max}$, N m) on the z-axis.

Conversely, the minimum torque lookup table specifies the lower torque boundary, primarily relevant for generator mode during regenerative braking. Negative torque values indicate energy recovery, with limits imposed by voltage, speed, and system stability to avoid excessive battery charging currents or mechanical stress. This table supports the simulation of braking dynamics and energy recuperation efficiency in hybrid configurations.

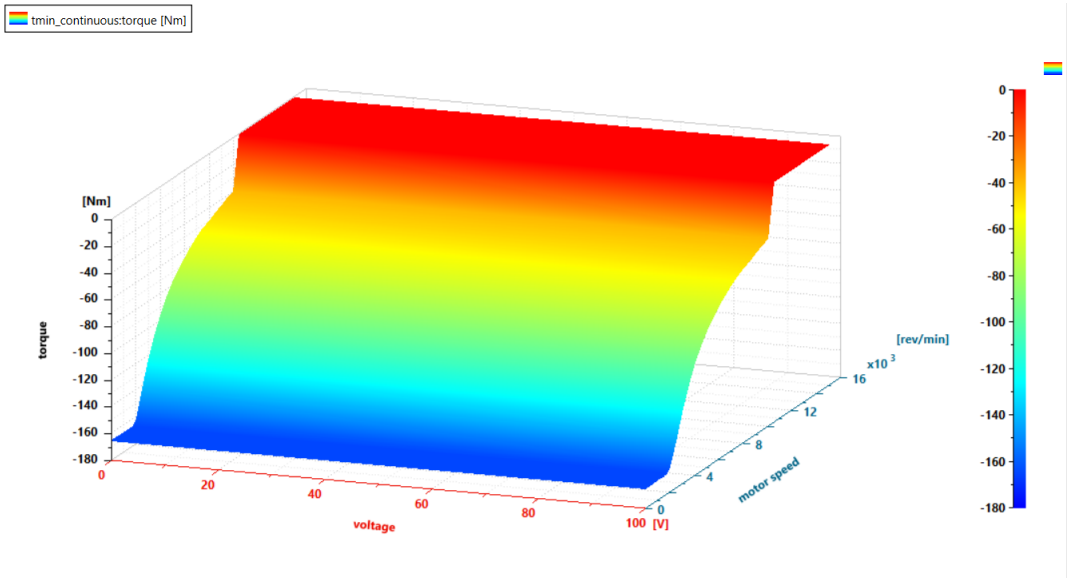

Figure 2.9: Lookup Table for Minimum Torque in the Motor, Mapping Voltage (V, V) on the x-axis, Motor Speed (N, RPM) on the y-axis, and Minimum Torque (T_{min}, N m) on the z-axis.

These lookup tables are interpolated during simulations to provide continuous values, enhancing the fidelity of the PMSM model while maintaining computational efficiency. They are typically generated from manufacturer data sheets and can be adjusted for specific motor designs in LCV applications [38, 39].

2.2.3 Modeling of Lithium-Ion Batteries

Lithium-ion batteries describe the main electrochemical and electrical behaviors through networks of resistors, capacitors, and voltage sources [43]. These models provide a good compromise between accuracy and computational efficiency, allowing prediction of terminal voltage, internal losses, and state-of-charge (SoC) evolution in system-level simulations.

In the adopted model, the battery pack is represented as an assembly of identical cells connected in series and parallel. Each cell is modeled by an open-circuit voltage (OCV) source dependent on SoC, an ohmic resistance R_{ohm} accounting for instantaneous voltage drop, and one or more parallel RC branches that reproduce dynamic voltage responses related to charge-transfer and diffusion phenomena. The charge-transfer branch, defined by R_{ct} and C_{ct}, captures short-term polarization effects, while additional diffusion branches ($R_{\text{diff}}[i], C_{\text{diff}}[i]$) describe slower transients associated with lithium-ion transport within the electrodes. The index i refers to each diffusion time constant, typically with $i = 1, 2, \ldots, N_{\text{RC}}$.

The terminal voltage of the battery is expressed as the difference between the equilibrium open-circuit voltage and the total voltage drops across the resistive and capacitive elements,

$$U = \mathrm{OCV}_{\mathrm{eq}} - \left(\Delta U_{\mathrm{ohm}} + \Delta U_{\mathrm{ct}} + \sum_i \Delta U_{\mathrm{diff}}[i] + \Delta U_{\mathrm{add}} + \Delta U_{\mathrm{hyst}} \right), \tag{2.21}$$

where ΔU_{add} and ΔU_{hyst} represent additional voltage contributions due to connector losses and hysteresis effects, respectively.

The dynamic behavior of each polarization branch follows a first-order differential equation. For the charge-transfer and diffusion elements, the voltage transient ΔU_x evolves as

$$\frac{d(\Delta U_x)}{dt} = -\frac{\Delta U_x}{R_x C_x} - \frac{I}{C_x}, \tag{2.22}$$

where $x \in \{\mathrm{ct}, \mathrm{diff}[i]\}$, and I is the applied current, defined as positive during discharge.

The state of charge represents the remaining capacity of the battery and changes according to the applied current as

$$\frac{d\mathrm{SoC}}{dt} = -\frac{I}{Q_{\mathrm{nom}}}, \tag{2.23}$$

where Q_{nom} is the nominal capacity expressed in coulombs.

For scaling to pack level, cell parameters are adapted according to the series and parallel configuration:

$$R_{\mathrm{pack}} = R_{\mathrm{cell}} \cdot \frac{n_s}{n_p}, \quad C_{\mathrm{pack}} = C_{\mathrm{cell}} \cdot \frac{n_p}{n_s}, \tag{2.24}$$

where n_s and n_p are the number of series and parallel cells, respectively. This scaling is applied to all resistive and capacitive parameters in the equivalent circuit.

2.2.3.1 Model Simplification for Drive Cycle Simulation

For drive cycle simulations where computational efficiency is critical and transient dynamics occur over timescales much longer than the RC time constants, a simplified zero-order model may be employed. In this case, the battery is represented only by the OCV and ohmic resistance:

$$V_{\mathrm{terminal}} = V_{\mathrm{OCV}}(\mathrm{SoC}) - I \cdot R_{\mathrm{ohm}} \tag{2.25}$$

This simplification is valid when:

- Drive cycle power transients are slow relative to charge-transfer dynamics (typically $\tau_{\text{ct}} < 10$ s)

- Steady-state voltage and power losses are the primary quantities of interest

- Computational speed is prioritized over capturing fast transient behavior

The ohmic resistance R_{ohm} in the simplified model effectively represents the combined effect of all resistive elements at steady state. This approach is commonly adopted in system-level vehicle simulation tools [43].

Model parameters including OCV characteristics and resistance values are functions of SoC, temperature, and current, typically identified from manufacturer datasheets. The specific parameter values and model implementation used in this study are detailed in Section 3.4.

This equivalent circuit formulation provides a physically interpretable yet computationally efficient framework for simulating the electrical dynamics of lithium-ion battery packs in electric vehicle powertrains [43].

2.2.4 Modeling of Inverter

The inverter converts DC power from the battery into three-phase AC voltage for the electric machine using a quasi-static model of a two-level voltage-source inverter (VSI) [19, 20, 21]. This approach neglects high-frequency switching effects and focuses on steady-state relationships among voltage, current, and power.

2.2.4.1 Voltage Modulation

The RMS phase voltage is limited by the DC input voltage U_{in} and modulation strategy:

$$U_{\text{rms,max}} = U_{\text{dcToUrms}} \cdot U_{\text{in}} \tag{2.26}$$

where U_{dcToUrms} is the voltage utilization ratio. For sinusoidal pulse-width modulation (SPWM), $U_{\text{dcToUrms}} = 1/(2\sqrt{2}) \approx 0.354$, whereas for space vector PWM (SVPWM) or third-harmonic injection PWM (THIPWM), it increases to $1/\sqrt{6} \approx 0.408$.

2.2.4.2 Power Relationships

The instantaneous power on the AC side can be expressed as:

$$P = 3VI\cos(\theta_V - \theta_I) \tag{2.27}$$

where V and I are the RMS phase voltage and current, and $\theta_V - \theta_I$ is the phase difference. The current on the DC side follows from power balance:

$$I_{\text{in}} = \frac{P + \Phi_h}{U_{\text{in}}} \tag{2.28}$$

where Φ_h represents the total power dissipated as heat in the inverter.

2.2.4.3 Semiconductor-Based Power Loss Model

Energy conversion in the inverter generates heat due to conduction and switching losses within the semiconductor devices. Conduction Losses The conduction loss mechanisms differ fundamentally between device types:

MOSFETs exhibit purely resistive losses when conducting:

$$P_{\text{cond,MOSFET}} = I_{\text{RMS}}^2 \cdot R_{\text{DS(on)}}(T_j) \tag{2.29}$$

where I_{RMS} is the root-mean-square current through the device and $R_{\text{DS(on)}}(T_j)$ is the drain-source on-resistance at junction temperature T_j. Note that MOSFETs do not have a threshold voltage component in their conduction losses—the characteristic is purely resistive.

IGBTs exhibit a combined voltage-drop and resistive characteristic:

$$P_{\text{cond,IGBT}} = V_{\text{CE0}} \cdot I_{\text{avg}} + r_{\text{CE}} \cdot I_{\text{RMS}}^2 \tag{2.30}$$

where V_{CE0} is the collector-emitter threshold voltage, I_{avg} is the average current, and r_{CE} is the differential on-state resistance. At high currents, the threshold voltage term becomes negligible, and since typically $r_{\text{CE}} < R_{\text{DS(on)}}$ for silicon devices of comparable voltage rating, IGBTs generally have lower conduction losses than Si MOSFETs at high continuous currents.

Freewheeling Diodes (external or body diodes):

$$P_{\text{cond,diode}} = V_F \cdot I_{\text{avg}} + r_d \cdot I_{\text{RMS}}^2 \tag{2.31}$$

where V_F is the forward voltage drop and r_d is the diode differential resistance.

2.2.4.4 Temperature Dependence

MOSFET on-resistance increases with temperature:

$$R_{\text{DS(on)}}(T_j) = R_{\text{DS(on)},25°\text{C}} \cdot [1 + \alpha_R(T_j - 25)] \tag{2.32}$$

IGBT threshold voltage typically decreases slightly with temperature, resulting in relatively stable conduction losses.

2.2.4.5 Switching Losses

The power dissipated during switching transitions is:

$$P_{\text{sw}} = f_{\text{sw}} \cdot (E_{\text{on}} + E_{\text{off}}) \tag{2.33}$$

where f_{sw} is the switching frequency, and E_{on}, E_{off} are the turn-on and turn-off energy losses per cycle. These energies are provided in manufacturer datasheets at reference conditions (I_{ref}, U_{ref}, T_{ref}) and scale with operating conditions as:

$$E_{\text{sw}}(I, U, T_j) = E_{\text{sw,ref}} \cdot \left(\frac{I}{I_{\text{ref}}}\right) \cdot \left(\frac{U}{U_{\text{ref}}}\right) \cdot [1 + k_T(T_j - T_{\text{ref}})] \tag{2.34}$$

The reference conditions specified in datasheets are critical for accurate loss estimation. IGBTs exhibit significant tail current during turn-off due to minority carrier recombination, contributing substantially to switching losses. MOSFETs, especially SiC types, have negligible tail current and faster switching transitions.

2.2.4.6 Total Inverter Losses

For a three-phase inverter with six switches (upper and lower switches in three phase legs):

$$P_{\text{inv,total}} = \sum_{i=1}^{6} (P_{\text{cond,switch},i} + P_{\text{cond,diode},i} + P_{\text{sw},i}) \tag{2.35}$$

The distribution of losses between switch and diode depends on power factor and modulation strategy.

2.2.4.7 Parallel Device Configuration

High-power inverters typically use multiple devices in parallel per switch position to achieve required current ratings. For N parallel devices, the effective resistance per switch position is:

$$R_{\text{DS(on),leg}} = \frac{R_{\text{DS(on),device}}}{N} \tag{2.36}$$

In practice, current imbalance due to device tolerances and thermal gradients requires a derating factor of typically 5–10%.

2.2.5 Transmission

The transmission transfers torque from the power sources (ICE or EM) to the wheels, adapting speed and torque to meet driving demands. In hybrid configurations, it accommodates multiple inputs, often using clutches or torque converters for seamless

transitions. A fixed gear ratio is used in this study to simplify design and ensure consistent torque delivery. The relationships are:

$$T_{\text{out}}(t) = r_g \cdot T_{\text{in}}(t) \cdot \eta_t(t), \tag{2.37}$$

$$\omega_{\text{out}}(t) = \frac{\omega_{\text{in}}(t)}{r_g}, \tag{2.38}$$

where $T_{\text{out}}(t), T_{\text{in}}(t)$ (N m) are output and input torques, $\omega_{\text{out}}(t), \omega_{\text{in}}(t)$ (rad/s) are output and input speeds, r_g (dimensionless) is the gear ratio, and $\eta_t(t)$ (dimensionless) is transmission efficiency [27, 45].

2.2.6 Exhaust System

The exhaust system in a CNG-powered vehicle manages combustion byproducts to meet Euro 6 emission standards while maintaining performance. It includes the exhaust manifold, Three-Way Catalytic Converter (3WCC), muffler, and tailpipe. The 3WCC reduces CO, HC, and NOx through oxidation and reduction reactions using catalysts (platinum, palladium, rhodium). Ceria (CeO_2) stabilizes air-fuel ratio fluctuations, ensuring efficient operation near stoichiometric conditions ($\lambda \approx 1$) [7, 8]. Key reactions in the 3WCC are:

- CO oxidation: $2CO + O_2 \rightarrow 2CO_2$
- HC oxidation (methane): $CH_4 + 2O_2 \rightarrow CO_2 + 2H_2O$
- NOx reduction: $2NO + 2CO \rightarrow N_2 + 2CO_2$ or $2NO + 2H_2 \rightarrow N_2 + 2H_2O$

The 3WCC requires a light-off temperature (250–300°C) for effective operation, with lower temperatures reducing efficiency during cold starts. Oxygen sensors provide feedback to the engine control unit (ECU). The reaction rate for pollutant i (CO, HC, or NOx) (kg/s) is:

$$\dot{m}_i(t) = -k_i(T(t)) \cdot C_i(t) \cdot C_{\text{O}_2}(t) \cdot \theta_{\text{Ce}}(t), \tag{2.39}$$

where $k_i(T(t))$ follows the Arrhenius form ($k_i = Ae^{-E_a/RT}$), and oxygen storage dynamics are:

$$\frac{d\theta_{\text{Ce}}(t)}{dt} = k_{\text{ox}}(T(t)) \cdot C_{\text{O}_2}(t) \cdot (1 - \theta_{\text{Ce}}(t)) - k_{\text{red}}(T(t)) \cdot C_{\text{CO}}(t) \cdot \theta_{\text{Ce}}(t). \tag{2.40}$$

Exhaust temperature and flow influence thermal behavior, with catalyst aging modeled for long-term simulations [8].

2.3 Drive System Modeling and Selection for Light Commercial Vehicles

The drive system layout front-wheel drive (FWD), rear-wheel drive (RWD), all-wheel drive (AWD), and four-wheel drive (4WD) significantly influences vehicle performance, handling, and cargo capacity in LCVs. The dynamics and efficiency are governed by propulsion force distribution, analyzed using vehicle models [45, 25]. For longitudinal longitudinal motion on level ground, the equation of motion is:

$$F_{\text{trac}}(t) = F_{\text{res}}(t) + m\frac{dv(t)}{dt}, \tag{2.41}$$

where:

- $F_{\text{trac}}(t)$ (N) = tractive force at wheels,
- $F_{\text{res}}(t)$ (N) = total resistive force,
- $m\frac{dv(t)}{dt}$ (N) = inertial force from acceleration.

The total resistive force (N) is:

$$F_{\text{res}}(t) = F_{\text{cl}}(t) + F_{\text{aero}}(t) + F_{\text{roll}}(t), \tag{2.42}$$

where:

- $F_{\text{cl}}(t)$ (N) = climb resistance,
- $F_{\text{aero}}(t)$ (N) = aerodynamic drag,
- $F_{\text{roll}}(t)$ (N) = rolling friction forces.

Tractive force relates to torque as:

$$F_{\text{trac}}(t) = \frac{T_{\text{wheel}}(t)}{r_w}, \tag{2.43}$$

where $T_{\text{wheel}}(t)$ (N m) is wheel torque and r_w (m) is wheel radius. The effective vehicle mass m_{veh} (kg) accounts for rotational inertia:

$$m_{\text{veh}} = m + m_{\text{add}} + \frac{n_{\text{front}} \cdot J_{W_{\text{front}}}}{R^2_{W_{\text{front}}}} + \frac{n_{\text{rear}} \cdot J_{W_{\text{rear}}}}{R^2_{W_{\text{rear}}}}, \tag{2.44}$$

where:

- m (kg) = vehicle base mass,
- m_{add} (kg) = additional mass,
- $n_{\text{front}}, n_{\text{rear}}$ = number of wheels,
- $J_{W_{\text{front}}}, J_{W_{\text{rear}}}$ (kgm^2) = moments of inertia,
- $R_{W_{\text{front}}}, R_{W_{\text{rear}}}$ (m) = wheel radii.

Aerodynamic drag (N) is:

$$F_{\text{aero}}(t) = \frac{1}{2} \cdot \rho_{\text{air}} \cdot S_x \cdot C_x \cdot (v(t) + v_{\text{wind}})^2, \tag{2.45}$$

where:

- $\rho_{\text{air}} = 1.225\,\text{kg/m}^3$ = air density,
- S_x (m^2) = frontal area,
- C_x = drag coefficient,
- $v(t), v_{\text{wind}}$ (m/s) = vehicle and wind velocities.

Rolling friction force (N) is:

$$F_{\text{roll}}(t) = (m + m_{\text{add}}) \cdot g \cdot (f + k \cdot v(t) + w \cdot v(t)^2) \cdot \cos\left(\arctan\left(\frac{\alpha}{100}\right)\right), \tag{2.46}$$

where:

- $g = 9.81\,\text{m/s}^2$ = gravitational acceleration,
- f, k, w = rolling resistance coefficients,

- α = road gradient percentage.

2.4 Control Strategies for Hybrid Vehicles

The Equivalent Consumption Minimization Strategy (ECMS) is a real-time energy management strategy used in hybrid electric vehicles to optimally distribute power between the internal combustion engine (ICE) and the electric machine (EM). Its main objective is to minimize total energy consumption while maintaining the battery's state of charge (SOC) close to its nominal value [27, 48]. ECMS evaluates, at each instant, the cost of using fuel and electrical energy and determines the power split that minimizes the total energy cost. The overall goal of ECMS is expressed through a cost function, which represents the total fuel-equivalent energy consumption over a driving cycle. This cost function is defined as:

$$J = \int_{t_0}^{t_f} \dot{m}_{\text{fuel,eq}}(t)\, dt, \tag{2.47}$$

where:

- J = total equivalent fuel consumption over the drive cycle,
- t_0, t_f = start and end times of the driving cycle,
- $\dot{m}_{\text{fuel,eq}}(t)$ (grams per second) = instantaneous equivalent fuel consumption rate.

The instantaneous equivalent fuel consumption rate $\dot{m}_{\text{fuel,eq}}(t)$ combines the actual fuel consumption by the ICE and the electrical energy used by the battery, converted into equivalent fuel units using an equivalence factor $s(t)$:

$$\dot{m}_{\text{fuel,eq}}(t) = \dot{m}_{\text{fuel}}(t) + s(t)\frac{P_{\text{elec}}(t)}{\text{LHV}}, \tag{2.48}$$

where:

- $\dot{m}_{\text{fuel}}(t)$ (grams per second) = fuel mass flow rate of the ICE,
- $P_{\text{elec}}(t)$ (watts) = electrical power from/to the battery (positive when discharging, negative when charging),
- LHV (joules per gram) = lower heating value of the fuel,

- $s(t)$ (grams per joule) = instantaneous equivalence factor converting electrical energy into fuel-equivalent units.

The instantaneous equivalence factor $s(t)$ accounts for the efficiency losses in the battery and the electric machine, and its value differs depending on whether the battery is being discharged or charged:

$$s(t) = \begin{cases} \dfrac{s_0}{\eta_{\text{chg}}(t) \cdot \eta_{\text{em}}(t)}, & \text{discharging}, \\ s_0 \cdot \eta_{\text{chg}}(t) \cdot \eta_{\text{em}}(t), & \text{charging}, \end{cases} \tag{2.49}$$

where:

- s_0 (grams per joule) = nominal equivalence factor, representing the baseline conversion between electrical and fuel energy,
- $\eta_{\text{chg}}(t)$ = battery charging efficiency,
- $\eta_{\text{em}}(t)$ = electric machine efficiency.

For real-time control, ECMS uses an *instantaneous Hamiltonian* $H(t)$, which represents the total equivalent energy cost at each instant:

$$H(t) = \dot{m}_{\text{fuel}}(t) \cdot \text{LHV} + s(t) \cdot P_{\text{elec}}(t), \tag{2.50}$$

where:

- $H(t)$ (watts) = instantaneous energy cost,
- $\dot{m}_{\text{fuel}}(t) \cdot \text{LHV}$ = energy rate supplied by fuel,
- $s(t) \cdot P_{\text{elec}}(t)$ = equivalent energy rate from electrical power.

At every time step, the controller selects the torque split between ICE and EM that minimizes $H(t)$, subject to powertrain constraints. In this way, ECMS achieves real-time optimization while approximating the minimization of the total cost function J over the drive cycle. The nominal equivalence factor s_0 is a crucial parameter in ECMS, as it defines the baseline trade-off between fuel and electrical energy. If s_0 is too low, the controller relies too heavily on the battery, causing excessive SOC

depletion. If s_0 is too high, the ICE dominates, reducing overall efficiency. An analytical estimate of s_0 can be obtained from the average ICE efficiency $\eta_{\text{eng,avg}}$ and the lower heating value of the fuel:

$$s_0 = \frac{1}{\eta_{\text{eng,avg}} \cdot \text{LHV}}. \tag{2.51}$$

For example, for a CNG engine with $\eta_{\text{eng,avg}} = 0.33$ and $\text{LHV}_{\text{CNG}} = 50 \times 10^6$ J/kg, the nominal equivalence factor is approximately:

$$s_0 \approx 6 \times 10^{-8} \text{ grams per joule.} \tag{2.52}$$

To achieve charge-sustaining operation, s_0 is refined iteratively. The final SOC should match the initial SOC after a driving cycle In summary, ECMS provides a systematic framework to minimize energy consumption in hybrid vehicles. By combining fuel and electrical energy into a single equivalent metric through the equivalence factor s_0 and minimizing the instantaneous Hamiltonian, the strategy optimally allocates power between ICE and EM. Accurate determination and calibration of the nominal equivalence factor s_0 ensure charge-sustaining operation, optimal fuel economy, and efficient hybrid vehicle performance.

2.5 Drive Cycles

Drive cycles are standardized speed–time profiles replicating real-world driving conditions for evaluating vehicle performance, fuel efficiency, and emissions. Two cycles are used: the Worldwide Harmonized Light Vehicles Test Cycle (WLTC) and the Real Driving Emissions (RDE) procedure.

2.5.1 Worldwide Harmonized Light Vehicles Test Cycle (WLTC)

Overview: The WLTC, developed by UNECE, represents urban, suburban, and highway driving for laboratory-based type approval testing of fuel consumption, emissions, and hybrid powertrain behavior. Distance, Duration, and Speed The WLTC spans 23.27 km over 1800 s (30 minutes), with 13% idling time. It includes four phases—Low, Medium, High, and Extra-High with a maximum speed of 131.3 km/h. Driving environment proportions are:

- Urban: 8.66 km (37.24%), 0 km/h to 60 km/h, frequent stops.
- Rural: 7.14 km (30.73%), 60 km/h to 80 km/h, moderate cruising.
- Highway: 7.45 km (32.03%), 80 km/h to 131 km/h, sustained acceleration.

Purpose: The WLTC evaluates vehicle performance, fuel consumption, and emissions in controlled conditions, suitable for studying hybrid powertrain transitions and emission-control strategies.

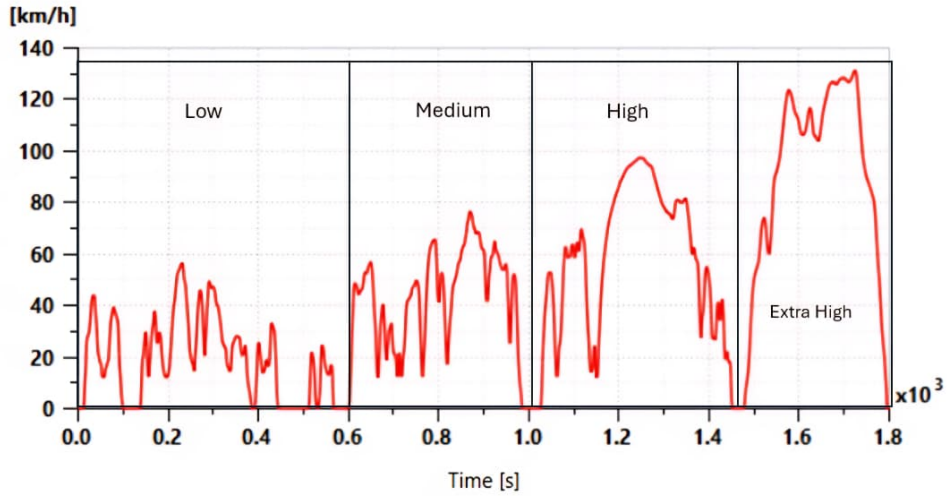

Figure 2.10: Velocity Profile of the WLTC Drive Cycle

2.5.2 Real Driving Emissions (RDE)

Overview: The RDE procedure measures real-world emissions (CO_2, NOx, CO, particulate matter) using Portable Emissions Measurement Systems (PEMS) without a fixed speed–time profile.The Copenhagen-based RDE route was implemented using the Simcenter Amesim RDE module [35], which supports importing cycles from OSE Road [36] and the TNO Random Cycle Generator [37]. Distance, Duration, and Speed The selected RDE test (Copenhagen-based) lasts 114.8 min over 105.26 km, with:

- Urban: 44.52 km (42.29%), 0 km/h to 60 km/h, average speed 15 km/h to 40 km/h.
- Rural: 30.73 km (29.19%), 60 km/h to 90 km/h.
- Highway: 30.01 km (28.51%), above 90 km/h, up to 145 km/h, with at least 5 min above 100 km/h.

Dynamicity is evaluated using Relative Positive Acceleration (RPA) (m/s^2) and velocity-acceleration product ($v \cdot a_{pos}$) ($km/hm/s^2$).

Purpose: The RDE assesses emissions and hybrid powertrain performance under real-world conditions, evaluating torque response to dynamic load demands.

Figure 2.11: RDE Copenhagen Drive Cycle map

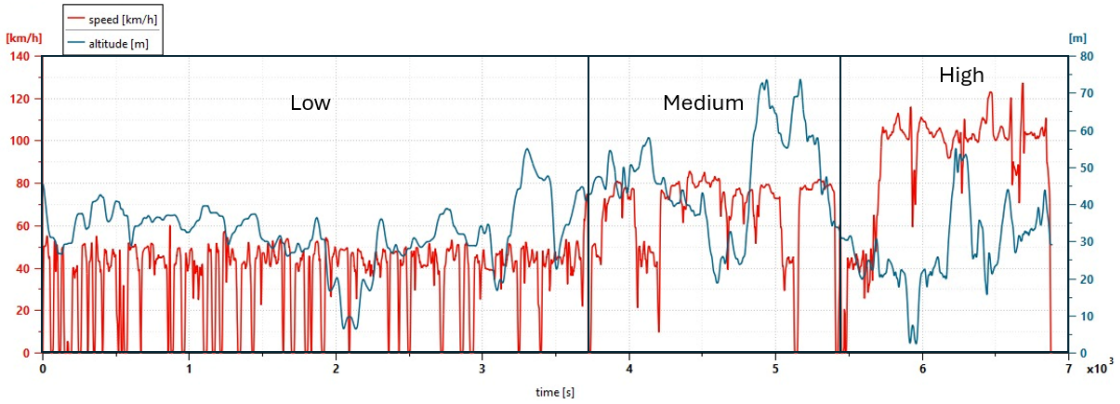

Figure 2.12: Velocity and altitude Profile of the RDE Copenhagen Drive Cycle

2.6 Performance Tests

2.6.1 Acceleration Time

This test evaluates the 0–100 km/h acceleration time, a key metric for assessing torque delivery and powertrain responsiveness. Tests are conducted on a flat, dry road under

standard atmospheric conditions (air density $\rho = 1.225\,\mathrm{kg/m^3}$, temperature 20 °C, and sea-level pressure). The vehicle mass m_{veh} includes curb weight. Acceleration begins from rest using optimal launch control. The acceleration time t is derived from longitudinal vehicle dynamics:

$$t = \int_0^{100} \frac{m_{\mathrm{veh}}}{F_{\mathrm{trac}}(v) - F_{\mathrm{res}}(v)}\, dv, \tag{2.53}$$

where $F_{\mathrm{trac}}(v)$ and $F_{\mathrm{res}}(v)$ (N) represent the tractive and resistive forces, respectively, over the velocity range $v = 0$–100 km/h (27.78 m/s). This integral quantifies how net propulsion varies with speed, reflecting torque delivery and traction efficiency.

2.6.2 Top Speed Test

The top speed test measures the vehicle's maximum sustainable velocity, defined by the balance between available propulsion power and resistive losses:

$$P_{\mathrm{avail}}(t) = F_{\mathrm{res}}(v_{\mathrm{max}}) \cdot v_{\mathrm{max}}, \tag{2.54}$$

where P_{avail} (W) is the total available power from the internal combustion engine (ICE) and the electric motor (EM), and F_{res} is the total resistive force. The test is performed on a flat under the same loading and environmental conditions as the acceleration test. The vehicle is gradually accelerated to v_{max} and held steady for 30 s within a tolerance of ±1 km/h. At v_{max}, acceleration is zero, and available power equals resistive power.

3

Methodology

This chapter outlines the simulation methodology for evaluating Compressed Natural Gas (CNG)-electric hybrid powertrains for Light Commercial Vehicles (LCVs) using Siemens Simcenter AMESim. The simulations assess fuel consumption, CO_2 and NO_x emissions, and system efficiency under standardized test conditions: the Worldwide Harmonized Light Vehicles Test Cycle (WLTC), Real Driving Emissions (RDE) Copenhagen cycle, and a 0–100 km/h acceleration test, as referenced in Chapter 2. A simplified driveline model balances computational efficiency and accuracy for analyzing energy consumption, emissions, and vehicle dynamics. Custom models and control strategies are implemented to simulate realistic LCV operation across urban, highway, and rural environments.

3.1 Components and its Parameters

The simulation framework models key powertrain components to compare CNG-electric hybrid configurations (series and parallel) with conventional internal combustion engine (ICE) and battery electric vehicle (BEV) systems. The components are tailored for LCVs with a 0.9 ton payload, focusing on practical implementation in AMESim.

3.1.1 Driver Model Configuration

To ensure realistic driver–vehicle interactions in simulations, a simplified yet physically meaningful driver model was configured. Parameters were selected based on their influence on transient response, energy recovery, and cycle tracking accuracy. In hybrid light commercial vehicles (LCVs), anticipation and transition dynamics strongly affect how effectively regenerative braking and torque blending occur both of which determine the observed fuel economy and emission trends under WLTC and RDE conditions.

The selected configuration is designed to emulate a predictive, human like driving

pattern suitable for standardized cycles. An anticipation time of 1 s allows the driver model to react smoothly to upcoming speed changes. Transition ramps for acceleration and braking are applied to reduce abrupt torque changes and to facilitate realistic blending between electric and combustion torque [35, 41, 42]. These parameters provide a consistent and reproducible setup for assessing vehicle operating strategies under WLTC and RDE conditions.

Table 3.1: Key Driver Model Parameters for Hybrid LCV Simulation

Parameter	**Setting**
Anticipation time	1 s
Cycle type	WLTC or RDE
Accel. transition time	0.2 s
Brake transition time	1 s
Brake release anticipation	0.5 s
Initial position	Forward

3.1.2 Vehicle Dynamics Model

The vehicle dynamics model was implemented using the standard Longitudinal Vehicle block in Simcenter Amesim to simulate the forward motion of a light commercial vehicle (LCV) under longitudinal forces. A front-wheel-drive (FWD) configuration was assumed for all powertrain variants (CNG–electric hybrid, ICE). The model converts driver inputs into axle torques, wheel speeds, and vehicle acceleration while accounting for aerodynamic drag, rolling resistance, and road gradient (0–5% for RDE). Lateral and yaw dynamics were neglected to prioritize computational efficiency for cycle-based evaluations such as WLTC and RDE.

A quasi-static formulation was adopted, solving the net force balance at 0.01 s time steps, as explained in Section 2.3. Aerodynamic and rolling parameters were selected to reflect typical high-profile LCV characteristics. The drag coefficient and frontal area are representative of standard LCV geometries, while the rolling resistance coefficient ($C_s = 0.015$) governs low-speed vehicle behavior. Wheel inertias represent unsprung mass effects relevant to torque transfer and regenerative braking modeling. The front-axle braking torque limit ensures appropriate braking behavior and integration with hybrid regenerative strategies.

Table 3.2: Key Vehicle Dynamics Parameters for LCV Model

Parameter	Implemented Value
Drag coefficient (C_x)	0.35
Frontal area (S_x)	$2.5\,\mathrm{m}^2$
Front/rear wheel inertia	$1.5\,\mathrm{kg\,m}^2$
Max front braking torque	3000 N m
Front/rear wheel radius	0.35m
Air temperature	20 °C
Air density	$1.226\,\mathrm{kg\,m}^{-3}$
Air pressure	1.049 25 bar

3.1.3 Gearbox/Transmission Model

The gearbox model employs AMESim's standard Discrete Gearbox block to represent a five-speed manual transmission used in the parallel hybrid and conventional CNG configurations of the light commercial vehicle (LCV). For the series hybrid layout, the mechanical transmission is replaced by a fixed single-speed reducer with a gear ratio of 9.3, providing direct torque transfer from the traction motor to the front axle. This differentiation ensures accurate modeling of each powertrain topology while maintaining a consistent vehicle dynamics interface.

The gearbox manages ratio selection, torque multiplication, and efficiency losses during shifts. Primary-shaft inertia is neglected for computational efficiency, while secondary-shaft dynamics and clutch synchronization are retained. Gear ratios span from 3.07:1 in first to 0.755:1 in fifth, with a final-drive ratio of 3.166:1. A viscous friction coefficient of 0.1 governs clutch smoothness, and a constant efficiency of 0.98 is assumed for all gears.

In the parallel and conventional configurations, the five-speed transmission reproduces typical LCV drivability under WLTC and RDE cycles. The low first-gear ratio (3.07) enables strong launch torque for payload operation. Higher gears progressively lower engine speed, with the fifth-gear overdrive (0.755) supporting efficient cruising. The constant 0.98 efficiency ensure smooth, durable shifts (<0.5 s) and accurate transient behavior. For the series hybrid, the fixed 9.3:1 reducer eliminates shift events, emphasizing low-speed torque delivery and regenerative braking recovery suited to stop-and-go city cycles.

Table 3.3: Gearbox and Reducer Parameters for Hybrid LCV Simulation

Parameter	Implemented Value
1st gear ratio	3.07
2nd gear ratio	1.84
3rd gear ratio	1.31
4th gear ratio	0.97
5th gear ratio	0.755
Axle reduction ratio	3.166
Gear efficiency (all gears)	0.98
Axle velocity switch tolerance	2 rev/min
Series Hybrid Fixed reduction ratio (reducer)	9.3

3.1.4 Engine Model

The engine model employs a Mean Value Engine Model (MVEM) from AMESim's Internal Combustion Engine library, adapted for a Compressed Natural Gas (CNG) spark-ignition engine in light commercial vehicle (LCV) hybrids. It represents a 1.8 L, four-cylinder unit (449 cm^3 per cylinder) , simulating quasi-steady-state behavior for torque production, fuel consumption, and emissions under transient cycles such as WLTC and RDE.

The core combustion submodel incorporates reaction kinetics to model ignition delay, flame propagation, and heat release, tailored to CNG's high octane and lean-burn capability ($\lambda = 1.0$–1.6). A quasi-dimensional approach accounts for turbulence and flame front dynamics, calibrated via lookup tables for volumetric, indicated, and exhaust efficiencies. These tables, described in Chapter 2, are derived from steady-state dynamometer tests and enable accurate predictions of brake specific fuel consumption . Pumping losses and internal delays are neglected for computational efficiency.

Key parameters configure the MVEM for CNG operation, with lookup tables providing 3D maps . These ensure cycle-specific fidelity, such as lean-burn NOx reduction. Heat rejection is evaluated via energy balance, and emissions models extend Zeldovich kinetics. Spark advance, equivalence ratio, and burned gas corrections are neglected to simplify baseline kinetics, while thermal thresholds limit cold-start effects.

Table 3.4: MVEM Engine Parameter Values and Lookup Tables

Parameter	**Implemented Value**
Number of cylinders	4
Accounting for internal delays	No
Accounting for pumping losses	No
Volumetric efficiency map	Look-up table
Exhaust energy fraction map	Look-up table
Indicated efficiency map	Look-up table
Cylinder displacement	449 cm^3
Maximum engine speed	6000 rev/min
High temperature threshold	80 °C
Low temperature threshold	20 °C
Throttle shaft diameter	8 mm
Throttle bore diameter	60 mm
Flow coefficient	0.72
Total intake manifold volume	6 L
Fuel heating value	47 700 kJ/kg
Fuel density	0.717 kg/m^3
Engine displacement	1.796 L (1.8 L)
Engine stall rotary velocity	10 rev/min
Engine mass	50 kg
Engine material	Aluminum (Al)
Exhaust thermal mass	1 kg
Exhaust material	Pure Aluminum (Al)
Catalytic converter length	37.5 mm
Catalytic converter diameter	144 mm
Catalyst wall thickness	0.118 mm
Number of catalysts	3
Coolant specific heat	4189 J/kg K

Inputs:

- Driver and Control Signals: Throttle position (0–1 normalized), spark advance [deg BTDC], and equivalence ratio (λ) from the supervisory controller.

- Environmental Feedback: Intake manifold pressure [bar], temperature [K], and exhaust backpressure, affecting volumetric efficiency.

- Cycle and State Inputs: Engine speed [rpm], load torque [Nm], and state-of-charge flags for hybrid mode switching (e.g., engine shutdown below 1,500 rpm).

3.1.5 Exhaust System

The Three-Way Catalytic Converter (3WCC) submodel, integrated with a 12-gas model (N_2, O_2, CO_2, H_2O, CO, H_2, NO, NO_2, NH_3, C, CH_4, HCO, OH, H), simulates CO and NO_x reduction at stoichiometric air/fuel ratios. An aluminum thermal capacitance element maintains exhaust temperatures between 400–600°C, with oxygen storage adjusted dynamically. The system incorporates three compact 3WCCs (each 37.5 mm long, 144 mm diameter) to enhance reduction of CO, NO_x, and unburned hydrocarbons (particularly CH_4). This configuration increases catalytic surface area and residence time, ensuring Euro 6 compliance across all driving conditions while distributing thermal loads and providing redundancy.

Table 3.5: MVEM Engine Exhaust and Cooling System Parameters

Parameter	**Implemented Value**
Exhaust thermal mass	1 kg
Exhaust material	Pure Aluminum (Al)
Catalytic converter length	37.5 mm
Catalytic converter · diameter	144 mm
Catalyst wall thickness	0.118 mm
Number of catalysts	3
Coolant specific heat	4189 J/Kg K

3.1.6 Inverter Model

The inverter model represents a three-phase voltage-source inverter interfacing the battery with the PMSM . The implementation follows the semiconductor-based loss model framework established in Section 2.2.4, with specific parameter selections.

3.1.6.1 Modulation Strategy

Third-Harmonic Injection PWM (THIPWM) was selected as the modulation strategy. As established in Section 2.2.4, THIPWM achieves $U_{\text{dcToUrms}} = 1/\sqrt{6} \approx 0.408$ compared to sinusoidal PWM's $1/(2\sqrt{2}) \approx 0.354$, providing approximately 15% higher voltage utilization from the DC bus. This translates to either higher output power at a given DC voltage or reduced current requirements for a target power level, both beneficial for efficiency and thermal management.

The switching frequency was set to 5 kHz, which is typical for automotive traction inverters in this power class. This frequency balances switching losses (which increase linearly with frequency per the equation $P_{\text{sw}} = f_{\text{sw}} \cdot E_{\text{sw}}$ from Section 2.2.4) against control bandwidth and acoustic noise considerations.

3.1.6.2 Device Technology Selection

SiC MOSFETs were selected for this application despite the general principle stated in Section 2.2.4 that IGBTs have lower conduction losses at high currents. The selection rationale addresses this apparent contradiction:

Section 2.2.4 explains that IGBTs typically have lower conduction losses than Si MOSFETs at high continuous currents because the IGBT's threshold voltage V_{CE0} becomes negligible and the differential resistance r_{CE} is typically lower than Si MOSFET $R_{DS(on)}$ values. However, SiC MOSFET technology achieves on-resistances 3–5× lower than Si MOSFETs of comparable voltage rating, fundamentally changing this trade-off.

At the selected 5 kHz switching frequency, switching losses contribute 40—50% of total inverter losses. As discussed in Section 2.2.4, MOSFETs (particularly SiC types) have negligible tail current during turn-off, whereas IGBTs exhibit substantial tail current due to their bipolar nature. This gives MOSFETs a significant advantage in switching losses. When conduction and switching losses are summed across the operating range, SiC MOSFETs provide lower total losses for this 50 kW, 400 V, 5 kHz application.

3.1.6.3 Device Configuration and Parameter Calculation

The inverter uses 4 SiC MOSFETs in parallel per switch position, resulting in 24 total MOSFETs (6 switch positions × 4 devices). This parallel configuration is necessary to achieve the required current rating while using commercially available discrete devices.

Target devices are 650 V SiC MOSFETs with individual on-resistance of approximately 10 mΩ at 25°C. Examples include devices similar to Wolfspeed C3M0120090J or ROHM SCT3040KL series [46, 47]. The 650 V rating provides adequate margin for the 400 V DC bus plus transients.

Following the parallel device equation from Section 2.2.4, the theoretical equivalent resistance is:

$$R_{DS(on),leg} = \frac{R_{DS(on),device}}{N} = \frac{10\ \text{m}\Omega}{4} = 2.5\ \text{m}\Omega \tag{3.1}$$

However, current sharing among parallel devices is imperfect due to device parameter tolerances (±10–20% on $R_{DS(on)}$) and temperature gradients.Accounting for 5% current imbalance increases effective resistance to 2.62 mΩ:

$$R_{DS(on),leg,actual} = 2.5\ \text{m}\Omega \times 1.05 = 2.62\ \text{m}\Omega \tag{3.2}$$

This value is used in the conduction loss calculation $P_{\text{cond,MOSFET}} = I_{\text{RMS}}^2 \cdot R_{\text{DS(on)}}$ from Section 2.2.4.

External SiC Schottky diodes (4 per switch position) are added in parallel with the MOSFETs. While MOSFETs include integral body diodes, these silicon-based body diodes in SiC MOSFETs have poor reverse recovery characteristics. The external SiC Schottky diodes bypass the body diodes during freewheeling, improving switching performance. The diode parameters ($V_F = 0.9$ V, $r_d = 3.0$ mΩ) are used in the diode conduction loss equation from Section 2.2.4.

3.1.6.4 Reference Current Justification

The reference current of 300 A requires explanation as it is significantly higher than the continuous operating current. This value serves two distinct purposes:

First, it represents the datasheet reference condition at which switching loss data is specified. Manufacturer datasheets provide switching energy values (E_{on}, E_{off}) at specific test conditions. The AMESim loss model uses these reference conditions to scale losses to actual operating points using the scaling equation from Section 2.2.4. Using 300 A as the reference aligns with typical datasheet test conditions for high-power SiC MOSFETs.

Second, it represents the peak transient current capability required for traction applications. The continuous operating current at 50 kW is calculated as:

- DC side: $I_{\text{DC}} = 50{,}000/(0.97 \times 400) = 129$ A
- AC side RMS: $I_{\text{RMS}} = 50{,}000/(3 \times 163) = 102$ A
- AC side peak: $I_{\text{peak}} = 102 \times \sqrt{2} = 144$ A

However, traction inverters must provide peak torque for hard acceleration, which requires current capability 2–2.5× the continuous rating for short durations (5–10 seconds). Therefore: $I_{\text{peak,transient}} = 144 \times 2.1 = 300$ A. This is standard industry practice for automotive traction inverters.

3.1.6.5 Switching Loss Energy

The switching loss energy $E_{\text{sw,ref}} = 3.5$ mJ represents the combined turn-on and turn-off energy for one switch position (4 parallel devices) at the reference conditions

(300 A, 400 V, 25°C). From typical SiC MOSFET datasheets, individual devices exhibit approximately 0.875 mJ combined switching energy at these conditions. For 4 parallel devices: $4 \times 0.875 = 3.5$ mJ per switch position. This value is then scaled to actual operating conditions using the switching loss equation from Section 2.2.4.

3.1.6.6 Implemented Parameters

The complete parameter set is summarized in Table 3.6. All parameters implement the theoretical equations from Section 2.2.4.

Table 3.6: Inverter Model Parameters Implemented

Parameter	**Value**	**Reference**
PWM scheme	THIPWM	Voltage utilization $U_{\text{dcToUrms}} = 1/\sqrt{6}$
Switching frequency	5 kHz	Used in $P_{\text{sw}} = f_{\text{sw}} \cdot E_{\text{sw}}$
Devices per switch	4 parallel MOSFETs	Parallel configuration equation
Total MOSFETs	24 devices	6 positions × 4 devices
Individual $R_{\text{DS(on)}}$	10 mΩ @ 25°C	650V SiC MOSFET
Parallel $R_{\text{DS(on),leg}}$	2.62 mΩ @ 25°C	Used in $P_{\text{cond}} = I^2R$
Temperature coefficient α_R	0.003 /°C	Temperature dependence equation
Diode V_F	0.9 V	External SiC Schottky
Diode r_d	3.0 mΩ	Used in $P_{\text{cond,diode}}$ equation
$E_{\text{sw,ref}}$	3.5 mJ/cycle	At reference conditions, per position
I_{ref}	300 A	Datasheet reference & peak transient
U_{ref}	400 V	DC bus voltage
Continuous RMS current	102 A	At 50 kW rated power
Peak phase current	144 A	$= \sqrt{2} \times 102$ A
$I_{\text{max,solver}}$	$1{\times}10^6$ A	Numerical solver limit only

The loss model scales switching energy with actual operating current and voltage using the equations from Section 2.2.4, enabling accurate efficiency prediction across the vehicle drive cycle operating range.

3.1.7 Electric Machine Model

The Permanent Magnet Synchronous Machine (PMSM) model was implemented to represent hybrid light commercial vehicle (LCV) operation, supporting both motoring and generating modes. The machine has four pole pairs, which define the relationship between electrical and mechanical rotor speed and influence torque ripple. The d–q flux linkages (Ψ_d, Ψ_q) are obtained from lookup tables and cross-coupling effects, enabling accurate computation of electromagnetic torque.

The stator windings are star-connected, with negligible end-winding inductance. Stator resistance is temperature-dependent and implemented as $R_s(T_w) = R_{\text{ref}} \cdot (1 + \alpha_T(T_w - T_{\text{ref}}))$, where $R_s(T_w)$ is the effective electrical resistance [Ω] of the stator windings as a function of winding temperature T_w [°C] is winding temperature, R_{ref} [Ω] is the baseline stator resistance measured at the reference temperature $T_{\text{ref}} = 25$ °C, and $\alpha_T = 0.00393$ 1/°C is the temperature coefficient of copper, reflecting the physical properties of the stator conductors.

AC losses, arising from skin and proximity effects at higher electrical frequencies, are approximated by an empirical scaling factor applied to the temperature-corrected stator resistance, $R_s^{\text{AC}}(f_e, T_w) = k_{\text{AC}}(f_e) \cdot R_s(T_w)$, where $R_s^{\text{AC}}(f_e, T_w)$ [Ω] is the frequency-adjusted stator resistance incorporating both temperature and electrical frequency f_e [Hz] effects (related to mechanical rotor speed ω_m by $f_e = (p/2) \cdot (\omega_m/(2\pi))$, with $p = 4$), and $k_{\text{AC}}(f_e)$ is a dimensionless empirical multiplier (derived from experimental data for the winding geometry) that scales the base resistance to approximate non-uniform current distribution in conductors.

This provides a computationally efficient first-order representation of frequency-dependent losses without detailed electromagnetic simulations. Iron losses, including hysteresis and eddy-current contributions, are considered for rotor speeds above 100 rev/min and are computed using empirical formulas as functions of d–q currents and rotor speed.

Model inputs include electrical angle and current references (I_d, I_q) from the Field-Oriented Control (FOC), phase voltages and rotor position from the inverter, winding temperature T_w for resistance and AC/iron loss scaling, and mode flags and torque limits from the Electric Machine look up table. The key parameters and scaling rationale for the PMSM model are summarized in Table 3.7. Both the electric traction motor and the generator were modelled based on the explanations and parameter data presented in Table 3.7

Table 3.7: PMSM Model Parameters and Scaling Rationale

Category	**Parameter**	**Value / Description**
Pole Pairs	Electrical pole pairs	4
Winding	Connection	Star
Stator Resistance	Base value	$R_{\text{ref}} = 0.051964$ Ω at 25°C
Temperature Scaling	R_s factor	$1 + \alpha_T(T_w - 25)$, $\alpha_T = 0.00393$ 1/°C

Both the electric traction motor and the generator were modeled based on the explanations and parameter data presented in Table 3.7

3.2 Field-Oriented Control Subsystem for Electric Machines

The Field-Oriented Control (FOC) subsystem for the Permanent Magnet Synchronous Motor (PMSM) was designed as a modular architecture, integrating a current vector controller, a three-phase inverter model, and the motor model. This design balances realistic motor behavior with computational efficiency for hybrid vehicle simulations. A schematic of the subsystem is shown in Figure 3.1, illustrating the interaction between the control unit, inverter, and motor.

The core of the subsystem is the current vector controller, implemented using dual Proportional-Integral (PI) controllers to regulate the d-axis and q-axis currents. The controller computes the optimal current vector to deliver the commanded torque while ensuring adherence to physical constraints, including maximum current ($I_{\max}$), maximum voltage ($U_{\max}$), and rotor speed limits. Coordinate transformations, including Clarke and Park transformations, convert three-phase abc signals into the rotating dq0 frame, decoupling torque and flux for independent control. Phase-to-line and line-to-phase conversions ensure compatibility between measurements and control requirements, while the homopolar component remains unused for balanced star winding operation.

An average three-phase inverter model was incorporated to convert the DC bus voltage to the AC voltages required for motor operation. This model calculates power losses for efficiency analysis while avoiding the computational cost of simulating switching transients, providing a practical balance between accuracy and simulation speed.

The FOC subsystem provides precise and independent control of torque and flux, which is critical for hybrid vehicles where torque must be dynamically blended with the internal combustion engine. Constraint handling prevents thermal and electrical overload, ensuring safe operation across a wide range of driving conditions. The system naturally transitions between constant torque and constant power regions, implementing field weakening at high speeds to maintain efficiency and extend operational range. Real-time adaptability to variations in DC bus voltage, battery state-of-charge, and motor temperature ensures consistent torque delivery and reliable system performance under dynamic conditions.

In summary, the subsystem was constructed to provide fast, accurate, and safe torque control, while enabling hybrid vehicles to operate efficiently across diverse driving scenarios. Its modular design ensures both high simulation fidelity and practical applicability for potential real-world implementation.

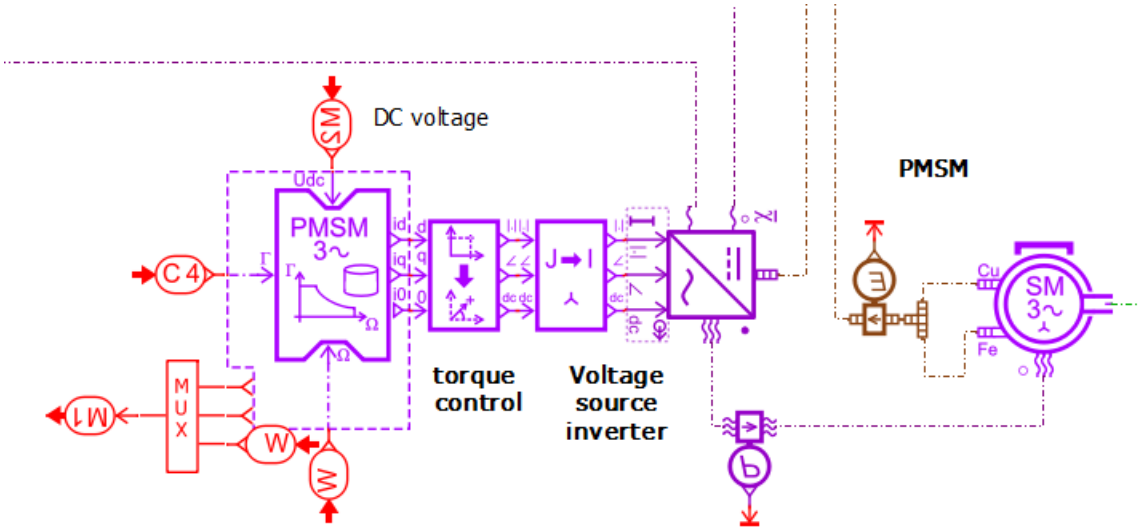

Figure 3.1: Schematic of the Field-Oriented Control (FOC) subsystem for the PMSM

3.3 Mass Configuration and Payload Standardization

Curb weights of 1,600 kg for the conventional CNG, 1,800 kg for the parallel hybrid, and 2,000 kg for the series hybrid configurations were selected, each with a standardized 900 kg payload. These values represent realistic medium-sized commercial LCVs while maintaining compliance with the Light Commercial Vehicle (LCV) classification limit of 3.5 tonnes Gross Vehicle Weight Limit (GVWL) [55, 56]. The conventional CNG baseline of 1,600 kg corresponds to popular market models such as the Ford Transit Custom (1,550–1,750 kg) and VW Transporter (1,600–1,800 kg) [57, 58].

The parallel hybrid adds 200 kg (approximately 12.5%) to account for the electric motor, power electronics, and battery pack (80–120 kg motor, 80–100 kg battery, 20–40 kg reinforced components), consistent with real-world hybrid architectures sharing mechanical drive between the combustion engine and electric system [60, 61]. The series hybrid configuration increases curb weight by 400 kg (approximately 25%) due to its larger battery pack (250–300 kg), generator and power management hardware (80–100 kg), and higher-rated traction motor (50–70 kg) [61, 62]. These additions align with production examples such as the Ford Transit Custom range-extender, which exhibits weight increases of 350–450 kg over conventional variants [62].

Three payload scenarios were tested: no payload (curb weight only), 450 kg (50% capacity), and 900 kg (100% capacity), ensuring consistent comparison across configurations With total gross weights of 2,500 kg, 2,700 kg, and 2,900 kg, respectively, all

configurations remain comfortably below the 3.5 tonne LCV threshold. The standardized 900 kg payload, typical of urban delivery and trade vehicles, ensures consistent performance and efficiency comparisons across all powertrain types [55, 63].

Table 3.8: Vehicle Weight Configuration

Model	Curb Weight	Payload	GVWL	Margin to 3.5 t
Conventional CNG	1600 kg	900 kg	2500 kg	1000 kg (40%)
Parallel Hybrid	1800 kg	900 kg	2700 kg	800 kg (30%)
Series Hybrid	2000 kg	900 kg	2900 kg	600 kg (21%)

3.4 Battery Sizing for Hybrid Configurations

3.4.1 Battery Cell Specification and Electrical Model

Both configurations utilize lithium-ion cells with a rated capacity of 9 Ah and NMC chemistry.

Table 3.9: Lithium-Ion Cell Specifications

Parameter	Value
Nominal capacity	9 Ah
Nominal voltage	3.7 V
Minimum voltage (at 0% SoC)	2.7 V
Maximum voltage (at 100% SoC)	4.2 V
Cell chemistry	Li-ion (NMC)

3.4.1.1 Open Circuit Voltage Model

The open circuit voltage (OCV) as a function of state of charge was modeled using a polynomial fit consistent with typical lithium-ion cell characteristics:

$$V_{OCV}(SoC) = 2.7 + 1.8 \cdot SoC - 0.5 \cdot SoC^2 + 0.2 \cdot SoC^3 \tag{3.3}$$

where $SoC \in [0, 1]$. This yields 2.7 V at 0% SoC and 4.2 V at 100% SoC, consistent with the cell specifications in Table 3.9.

3.4.1.2 Battery Electrical Model

As described in Section 2.2.3, the battery was modeled using the simplified first-order equivalent circuit appropriate for drive cycle simulation:

$$V_{terminal} = V_{OCV}(SoC) - I \cdot R_s \tag{3.4}$$

where R_s represents the ohmic resistance. A constant value of $R_s = 0.05\ \Omega$ per cell was assumed based on typical automotive lithium-ion cells. Using the scaling relationship , pack-level resistances were calculated as:

- Series hybrid: $R_{pack} = \frac{n_s \cdot R_s}{n_p} = \frac{40 \times 0.05}{27} = 0.074\ \Omega$
- Parallel hybrid: $R_{pack} = \frac{n_s \cdot R_s}{n_p} = \frac{35 \times 0.05}{20} = 0.088\ \Omega$

Power losses were calculated as $P_{loss} = I^2 \cdot R_{pack}$. This simplified model neglects transient RC dynamics but accurately captures steady-state voltage behavior and power losses during drive cycle operation.

3.4.2 Series Hybrid Battery Sizing

3.4.2.1 Sizing Methodology

Battery capacity was determined through iterative drive cycle simulations with the following objectives:

- Provide energy buffering for generator load-leveling
- Complete drive cycle without violating voltage/SoC limits

Simulation findings:

- Significantly lower capacities : simulation crashed due to voltage limits, SoC limits, or energy depletion
- Intermediate capacities : simulation did not complete full drive cycles
- 35 kWh: successfully completed cycle with adequate margins

3.4.2.2 State of Charge Window

The 55–65% SoC window (6% usable) was selected to:

- Extend battery cycle life by avoiding degradation regions at 0–20% and 80–100%
- Maintain consistent power capability (reduced at extreme SoC values)
- Provide safety margins for unexpected conditions

This design—conservative limits with narrower operational range—is standard automotive practice.

Table 3.10: Series Hybrid Battery Parameters

Parameter	Value
Configuration	27p40s (1,080 cells)
Cell capacity	9 Ah
Voltage range	108–168 V
Total energy	35 kWh
Initial SoC	60%
SoC limits	55% (min), 65% (max)
Mass	200 kg
Resistance	0.074 Ω

3.4.3 Parallel Hybrid Battery Sizing

3.4.3.1 Sizing Methodology

The parallel battery requires high peak power for electric-only propulsion rather than energy buffering. Key requirements:

- peak power for electric-only operation
- electric range at urban speeds
- Regenerative braking capability

Simulation findings: Similar to series hybrid, significantly lower capacities resulted

in simulation crashes or incomplete cycles. The 23.3 kWh capacity successfully completed the cycle with adequate power and energy margins.

3.4.3.2 State of Charge Window

The 20–65% SoC window (45% usable) is wider than series hybrid due to:

- Electric range maximization (wider window increases EV range)
- Increased regenerative capacity (65% max leaves more room for braking energy)
- Engine backup available (20% min acceptable since engine provides backup, unlike series)

The wider window increases cycling stress slightly but is acceptable given lower cycling frequency in parallel operation.

Table 3.11: Parallel Hybrid Battery Parameters

Parameter	**Value**
Configuration	20p35s (700 cells)
Cell capacity	9 Ah
Voltage range	95–147 V
Total energy	23.3 kWh
Initial SoC	60%
SoC limits	20% (min), 65% (max)
Mass	160 kg
Resistance	0.088 Ω

Key differences:

- Series prioritizes energy (40% more capacity) for buffering with higher voltage and lower current, reducing losses
- Parallel prioritizes power (10× higher) for electric propulsion with lower voltage and higher current
- Both configurations were determined through iterative simulation to meet functional requirements

3.5 Simulation Setup

3.5.1 Conventional CNG Model

The conventional Compressed Natural Gas (CNG) engine model was developed as a signal-based simulation framework , where each subsystem is interconnected through well-defined input and output signals that represent physical and control interactions within a real vehicle. The overall model structure integrates several primary components, including the driver input, engine control unit (ECU), intake and MVEM system, cooling circuit, powertrain, and vehicle dynamics. Each subsystem communicates via continuous signal exchange carrying information about engine speed, vehicle velocity, throttle position, fuel mass flow rate, and temperature. The integration of these signals forms a closed-loop control structure, enabling the simulation to mimic the dynamic response of an actual CNG engine under varying operating conditions.

The signal flow initiates from the driver interface, which generates three major control signals: the accelerator pedal position, the brake command, and the clutch engagement status. The accelerator signal, normalized between 0 and 1, indicates the driver's torque demand, while the brake and clutch signals act as discrete control inputs that modify engine load and torque transfer. These signals are transmitted to the powertrain information builder and subsequently to the engine control subsystem, which forms the computational core of the model. The driver accelerator signal serves as the main input to the ECU, while brake and clutch signals are used to adjust load conditions and vehicle dynamics.

Within the engine control subsystem, the accelerator input, engine speed, and vehicle speed are processed through mathematical control functions denoted as $f(x)$ and $f(x, y)$. These functions implement throttle control algorithms based on real-time feedback. The engine speed feedback is derived from the powertrain (crankshaft sensor output), while the vehicle speed feedback originates from the vehicle dynamics subsystem. Both signals enable the ECU to perform closed-loop regulation of throttle and torque. The overall structure of the Engine Control Unit (ECU), which manages these signal interactions and control laws, is illustrated in Figure 3.2. The output from this control logic is the throttle control signal, which defines the opening of the throttle valve and determines the air mass entering the engine intake manifold.

The throttle control signal propagates to the intake subsystem, where air enters through an air cleaner and passes the throttle body before reaching the intake manifold. Based on the throttle position and pressure differential, the air mass flow rate (AMFR) is computed. This signal, along with throttle position, is supplied to the fuel control logic to calculate the fuel mass flow rate (FMFR), ensuring a stoichiometric air–fuel ratio for efficient CNG combustion. These air and fuel flow

signals are routed to the MVEM block, which models the combustion process and generates engine torque, engine speed, and fuel consumption rate. The resulting engine torque output drives the powertrain subsystem, while the engine speed and fuel consumption outputs are returned as feedback to the ECU for real-time adjustment.

In the powertrain subsystem, the generated torque is transmitted through the Crankshaft ,clutch, gearbox, and driveline components to produce wheel rotation and vehicle speed. The clutch signal from the driver determines whether engine torque is transmitted to the wheels or disengaged. The resulting vehicle speed is then measured and sent back to the engine controller, completing the feedback loop between the powertrain and ECU. This bidirectional signal exchange ensures that the system dynamically responds to driver inputs, maintaining smooth acceleration, stable idling, and efficient torque management.

The cooling subsystem operates as a thermally regulated network linked by multiple feedback signals. Inputs such as coolant temperature, engine speed, and ambient air temperature are processed through control functions $f(x)$, which determine the activation of the radiator fan and thermostat valve. The corresponding control outputs regulate coolant flow and heat exchange rates, ensuring that the engine maintains its optimal operating temperature. The temperature feedback signal from the cooling system is also connected to the engine subsystem, influencing combustion efficiency and fuel management during prolonged or high-load operation.

All subsystems in the CNG engine model are interconnected through signal pathways that form an integrated control and feedback network. The engine speed signal serves as the central feedback variable, linking the combustion, cooling, and control systems, while the vehicle speed signal bridges the powertrain and controller. Similarly, throttle, fuel flow, and temperature signals act as actuator commands, directly influencing airflow, combustion, and thermal regulation. This interconnected design enables the model to operate in a closed-loop configuration, where outputs from one subsystem serve as control inputs to another, achieving dynamic equilibrium and realistic simulation behavior is illustrated in Figure 3.3.

In summary, the CNG engine model functions as a signal-driven control architecture in which the interconnection of subsystems replicates the real-time interactions of an actual engine–vehicle system. Driver commands initiate the control process, the ECU interprets these inputs, and the resulting control signals govern air, fuel, and temperature subsystems. The combustion and powertrain outputs are continuously monitored and fed back to the controller for adaptive correction. Through this comprehensive signal network, the model effectively captures the behavior of a conventional CNG engine, providing a reliable platform for analyzing performance, control strategies, and energy efficiency under various driving conditions.

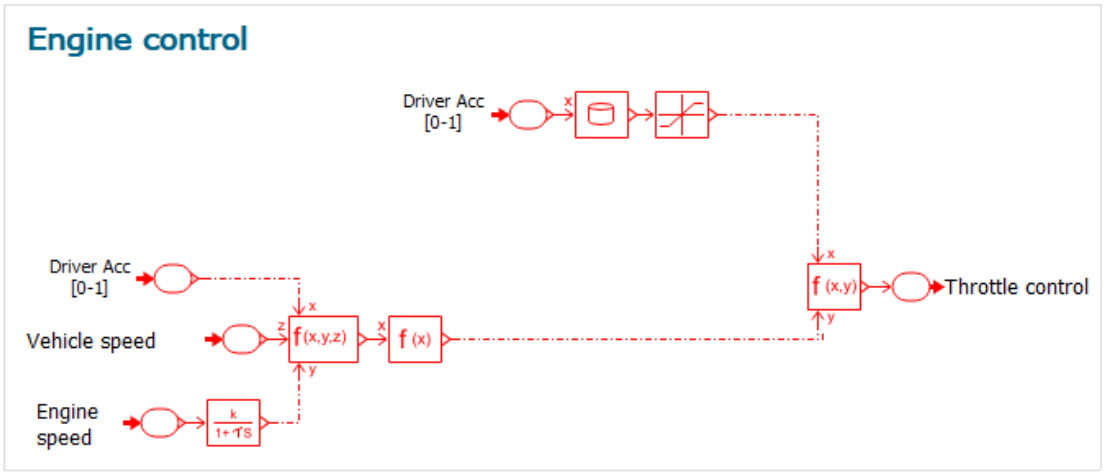

Figure 3.2: Engine Control Unit for the Conventional CNG Model

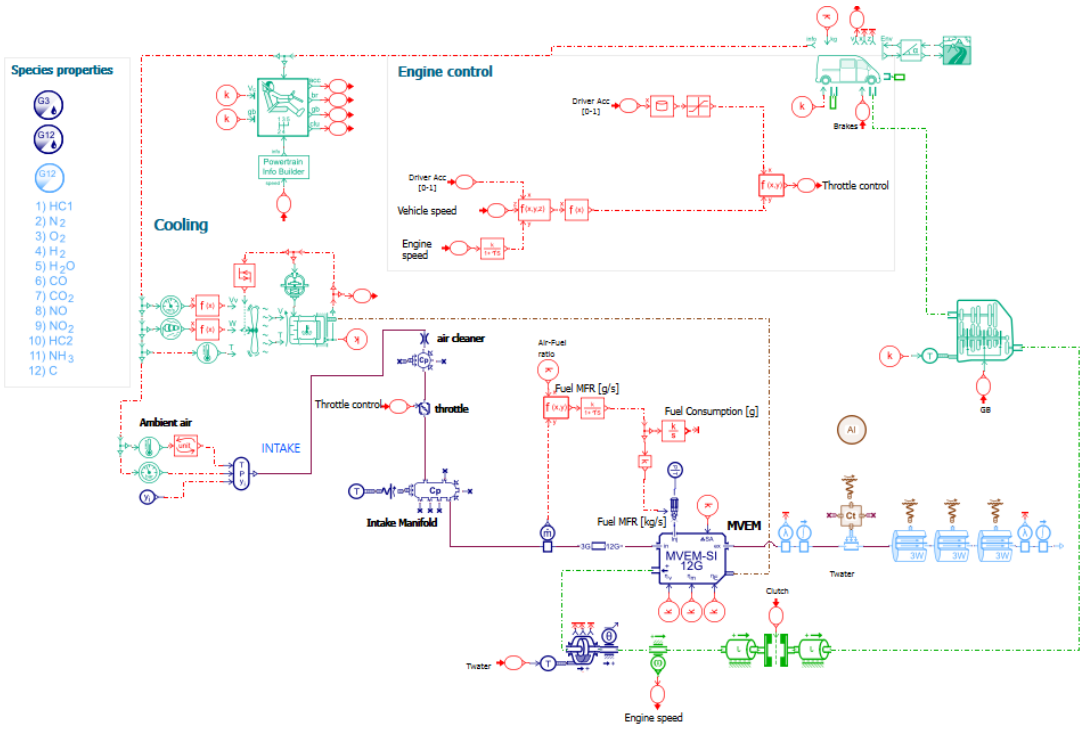

Figure 3.3: Conventional CNG Engine Model in Simcenter Amesim

3.5.2 Series Hybrid Model

In the series hybrid configuration, all subsystem interactions are coordinated through the Energy and Control Management System (ECMS), which functions as the centralized energy and control hub. The ECMS continuously receives feedback from sensors and driver inputs to determine optimal power distribution and operating states.

Driver-related signals such as accelerator (Acc), brake (Brk), and gearbox (Gb) indicate propulsion and deceleration demand. These inputs, along with auxiliary power request (K), are processed by the ECMS alongside system feedback such as motor torque (SM), generator torque (TM), and battery state of charge (SOC).

The MVEM engine subsystem receives command signals from the ECMS for throttle position (C8), fuel injection rate, and start/stop control. The engine operates independently of wheel speed, running only to generate electricity via the generator. Engine performance feedback, including air-fuel ratio (Cp), manifold pressure, intake temperature (T), and coolant temperature (M8), are returned to the ECMS for closed-loop optimization.

The generator is mechanically coupled to the MVEM engine and electrically connected to the DC link. It receives torque demand (TM) from the ECMS , converting the engine's mechanical output into electrical power for the battery and motor. Generator feedback (OM) ensures synchronization and power balance.when Soc drops below 60% the ECMS is prioritizes generator and charge the battery. On the electric side, the PMSM motor receives the FOC and ECMS command signal (C4) to produce traction torque according to driver demand. Electrical power from the generator or battery passes through the inverter, with motor feedback signals (SM) reporting speed and torque for precise control. The battery subsystem monitors and transmits SOC and voltage (U_{bat}) to the ECMS, which regulates charging and discharging through the generator's output. In regenerative braking, the ECMS reverses motor operation to capture kinetic energy and restore (SOC).

Throughout the system:

- **Electrical signals** represent energy transfer.
- **Control signals** manage actuator commands.
- **Sensor feedback** enables adaptive control.

The ECMS ensures that the engine is never mechanically connected to the wheels, enforcing the pure series hybrid structure:

$$\text{Engine} \rightarrow \text{Generator} \rightarrow \text{Battery/Motor} \rightarrow \text{Wheels}$$

This signal-driven coordination enables efficient energy conversion, optimal engine

operation, and balanced battery management under varying driving conditions.

Table 3.12: Key ECMS Series Hybrid Signal Interactions

Signal Label	Source	Destination	Function
Acc / Brk / Gb	Driver input	ECMS	Determine traction demand and braking status
K (P_{aux})	Vehicle system	ECMS	Indicate auxiliary power requirements
SOC / U_{bat}	Battery	ECMS	Monitor state of charge and voltage for energy management
C4	ECMS	PMSM (Motor)	Command traction torque or regenerative braking torque
SM	Motor	ECMS	Provide motor speed and torque feedback
TM	ECMS	Generator	Command generator torque to match engine power output
OM	Generator	ECMS	Report generator speed and electrical output status
C8	ECMS	Engine throttle	Regulate air intake for combustion control
M8 (T_{wat})	Engine	ECMS	Monitor engine coolant temperature for thermal management
Ai / Cp / T	Engine sensors	ECMS	Provide air-fuel ratio, manifold pressure, and temperature data
Vi	Intake system	ECMS	Feedback for intake flow coordination
Ww / Vvh	Vehicle sensors	ECMS	Report wheel speed and vehicle velocity for system feedback

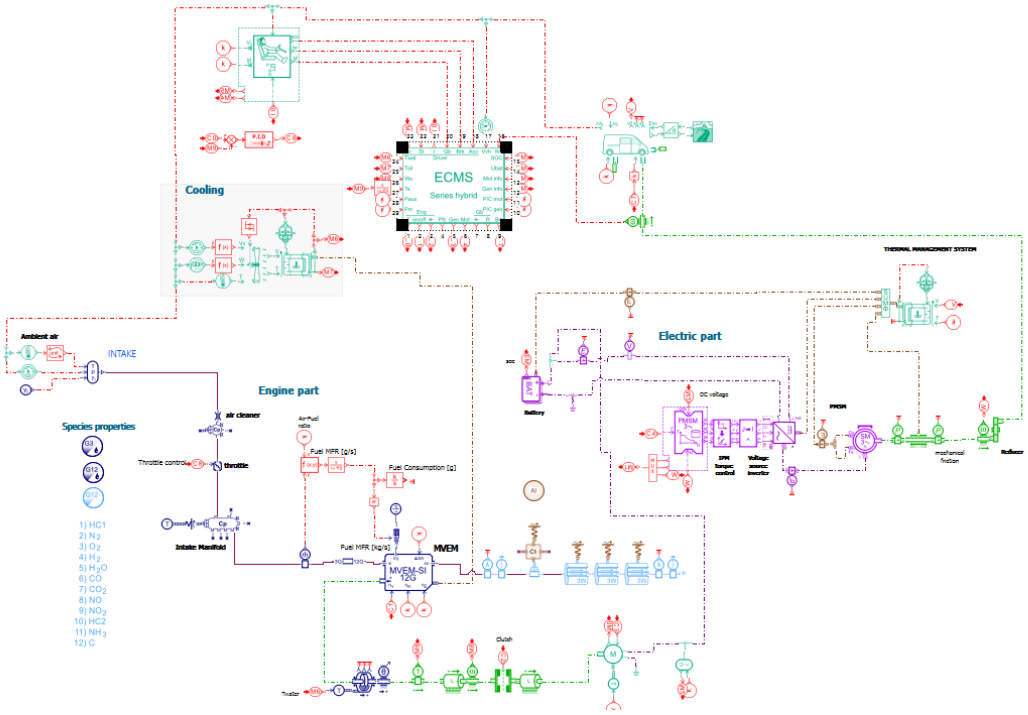

Figure 3.4: Series Hybrid Model

3.5.3 Parallel Hybrid Model

In the parallel hybrid configuration, the Energy and Control Management System (ECMS) coordinates both mechanical and electrical power flows while maintaining the battery state-of-charge (SOC) through an aggressive discharge and regenerative only recharge strategy.

The engine is mechanically coupled to the drivetrain, allowing it to deliver power directly to the wheels. The motor (PMSM) remains electrically connected to the battery and can either provide traction torque and act as a generator during braking.

Driver input signals accelerator (Acc), brake (Brk), and gearbox (Gb) inform the ECMS of torque demand and operating mode. When (SOC) is within the 60–20% window, the ECMS prioritizes electric propulsion, commanding the motor via the (C4) torque signal while keeping the engine off (clutch disengaged). Once (SOC) falls to 20%, the ECMS transitions to engine-dominant mode, engaging the clutch to connect the engine mechanically to the wheels. In this mode, the engine follows driver torque demand rather than operating at a fixed efficiency point.

During combined (hybrid) operation, both engine and motor supply torque to the gearbox, coordinated by the ECMS for smooth blending and performance opti-

mization. The battery system operates over a wide SOC window (60–20%) and is recharged solely through Engine and regenerative braking .The ECMS monitors (SOC), motor torque (SM), and engine feedback (speed, throttle, and temperature) to manage transitions among electric, hybrid, and engine-only modes.

Through this signal-driven structure, the ECMS balances efficiency, performance, and SOC stability using purely mechanical engine output and electrical motor assistance.

The parallel structure ensures:

$$\text{Engine} \leftrightarrow \text{Gearbox/Wheels} \quad \text{and} \quad \text{Battery} \leftrightarrow \text{Motor (PMSM)} \leftrightarrow \text{Gearbox}$$

Thus, mechanical and electrical torque paths operate in parallel under ECMS supervision.

Table 3.13: Key ECMS Parallel Hybrid Signal Interactions

Signal Label	**Source**	**Destination**	**Purpose / Function**
Acc / Brk / Gb	Driver input	ECMS	Determine torque demand, braking state, and gearbox coordination
SOC / U_{bat}	Battery	ECMS	Monitor charge level and voltage for mode selection
C4	ECMS	PMSM (Motor)	Command motor torque (positive for drive, negative for regeneration)
SM	Motor	ECMS	Provide speed and torque feedback for torque blending
C8	ECMS	Engine throttle	Control air intake and torque during mechanical drive
Clutch signal	ECMS	Engine / Transmission	Engage or disengage mechanical coupling to wheels
M8 (T_{wat})	Engine	ECMS	Monitor engine coolant temperature
Ai / Cp / T	Engine sensors	ECMS	Provide intake, pressure, and combustion feedback
Ww / Vvh	Vehicle sensors	ECMS	Report wheel speed and vehicle velocity for torque synchronization
K (P_{aux})	Vehicle system	ECMS	Report auxiliary electrical load for SOC management

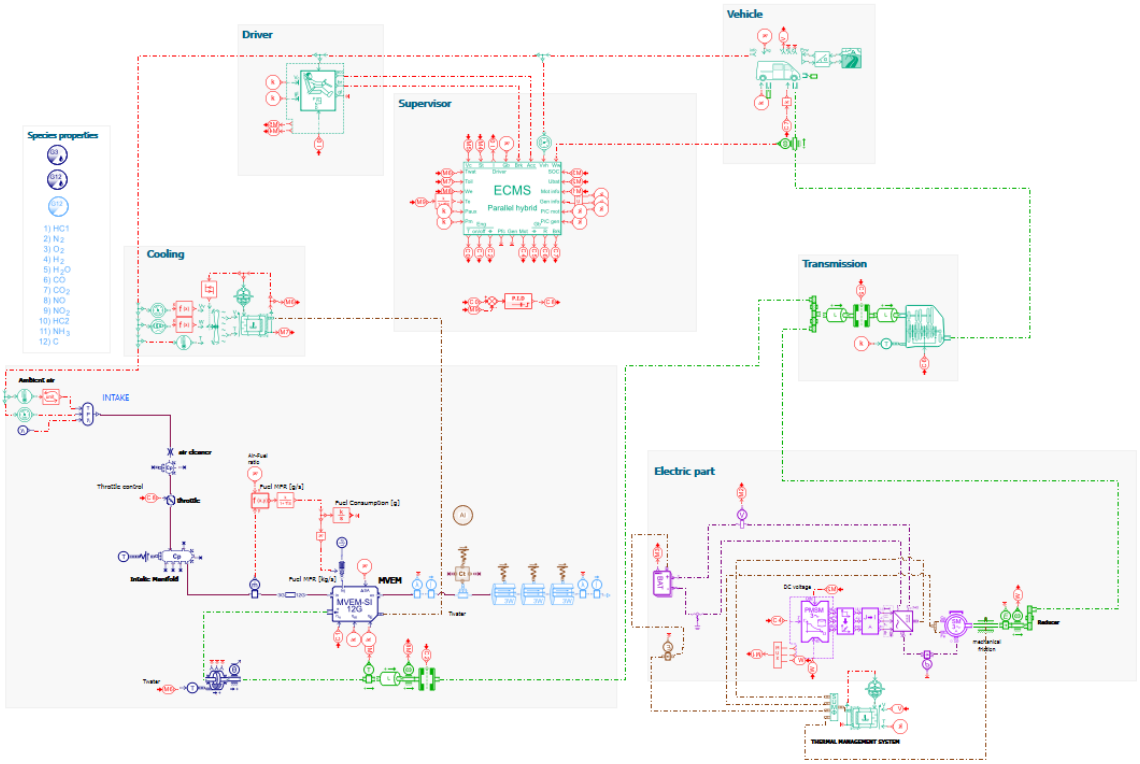

Figure 3.5: Parallel Hybrid Model

4

Results

This chapter analyzes the behavior of key components within the selected powertrain configurations and evaluates their responses under two driving cycles: the Worldwide Harmonized Light Vehicles Test Cycle (WLTC) and the Real Driving Emissions (RDE) cycle. The objective is to identify critical observations related to fuel consumption, emissions, and to conduct a comparative performance assessment of three configurations: conventional Compressed Natural Gas (CNG) Internal Combustion Engine (ICE), series CNG–electric hybrid, and parallel CNG–electric hybrid. The WLTC, being a standardized cycle with well-defined phases, was chosen as the basis for component-level analysis, since it provides consistent operating conditions that facilitate the evaluation of system responses. The RDE cycle is more variable in nature, its phase distribution is broadly comparable to that of the WLTC, as discussed in the theory section, and therefore it is used for the fuel and emission analysis. The focus is thus placed on a holistic evaluation of the three configurations to assess their operational viability and to provide insights into the influence of control strategies, key components, and input parameters under different driving conditions explained in the methodology.

4.1 Conventional ICE

Figure 4.1 presents a comparison between the actual vehicle speed and the WLTC reference profile. The overall characteristics of the WLTC cycle are well captured, transitioning from low to medium and high speeds, with peak values approaching 130 km/h during the Extra-High phase. The results indicate that the driver model and powertrain control system are properly calibrated: the engine, transmission, and vehicle dynamics closely follow the reference trajectory.

Transient tracking errors are generally below 0.1 seconds, with minor deviations during the Urban phase due to frequent acceleration and deceleration events. Overshoots of 2 to 5 km/h are occasionally observed, but the overall speed error remains

within ±0.5 km/h, with short duration peaks up to approximately 1.2 km/h. Such discrepancies are expected in transient drive cycle simulations due to vehicle inertia, control system lag, and discrete-time modeling. The engine controller, typically employing a PID strategy, continuously adjusts throttle input to minimize these deviations. Maintaining low speed errors is particularly important for accurate fuel consumption and emissions analysis.

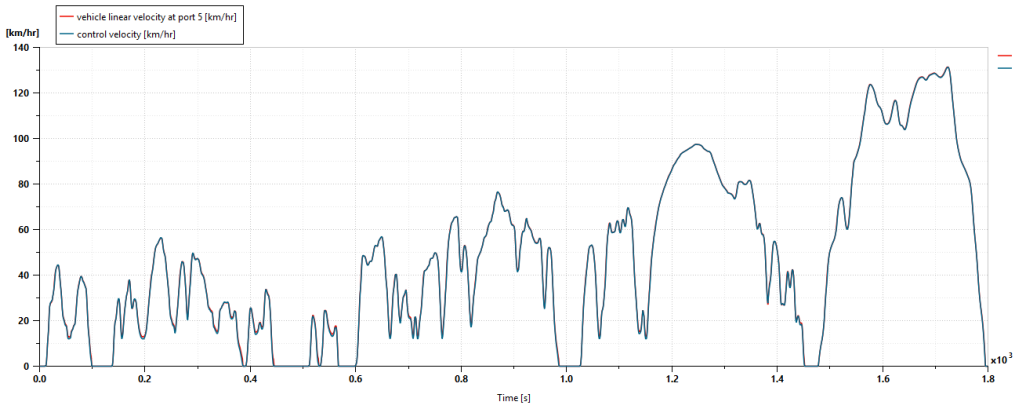

Figure 4.1: Vehicle speed tracking performance: actual (blue) vs. WLTC reference (red) over the full cycle.

The total driving force F_{drive} comprises contributions from vehicle inertia, rolling resistance, and aerodynamic drag, and becomes negative during braking events. An initial peak of approximately 6.5 kN arises as the vehicle overcomes resistive forces, after which the forces stabilize within the range of 0 to 3 kN, as shown in Figure 4.2. Positive peaks correspond to acceleration phases, whereas negative spikes indicate braking.

At higher speeds, aerodynamic drag becomes the dominant resistive component, requiring a sustained positive driving force even at constant velocity (see Equation 2.45 in Chapter 2). High-speed accelerations demand greater total force, directly increasing engine load, fuel consumption, and emissions. In contrast, rolling resistance dominates at low speeds, while aerodynamic drag governs resistive behavior at high speeds, which can be observed throughout the cycle run, as depicted in Figure 4.2.

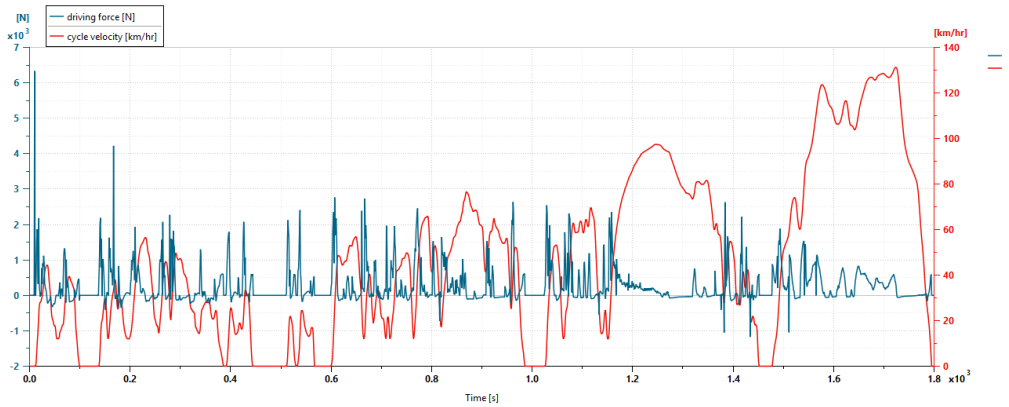

Figure 4.2: Traction force profile over the WLTC cycle, showing acceleration (positive) and braking (negative) demands.

4.1.1 Engine Analysis

The throttle valve in the conventional CNG internal combustion engine regulates engine load by controlling intake air mass flow, which, combined with proportional fuel delivery, determines power and torque output. The Electronic Control Unit (ECU) maps the driver's accelerator input to throttle positions ranging from 6 to 70 degrees, dynamically adjusting to achieve target vehicle speeds, as shown in Figure 4.3. At a fully closed throttle angle of 6 degrees, the engine enters fuel cut-off mode, enabling engine braking and improving fuel economy and emissions during deceleration, correlating with observed throttle reductions. Under part-load conditions, a partially open throttle incurs pumping losses due to intake manifold vacuum, reducing efficiency, as observed in moderate throttle angles during stable low-speed phases (e.g., 0.2 to 0.6 seconds). To minimize these losses, the ECU maximizes throttle opening for a given load, with peaks up to 70 degrees during acceleration aligning with velocity surges to 135 km/h, as depicted in Figure 4.3.

The throttle responds dynamically to driver demand, opening to 25 degrees during acceleration and closing to 6 degrees during deceleration or stops, resulting in rapid fluctuations. In the simulation, throttle spikes to 35, 55, and 70 degrees indicate the Engine Control System (ECS) interprets velocity increases as acceleration demands, requiring wider throttle openings to generate necessary torque, exceeding the optimal 6 to 25-degree range for steady-state cruising. This behavior is realistic for a four-cylinder spark-ignition engine, as the ECS uses velocity feedback to estimate load demand. While the 6 to 25-degree range optimizes efficiency at constant speeds, transient velocity changes necessitate higher angles to meet performance needs, reflecting real-world driving dynamics rather than a simulation error. The ECS's PID control prioritizes stability over aggressive response at high speeds, evident in smoother adjustments during high-velocity phases.

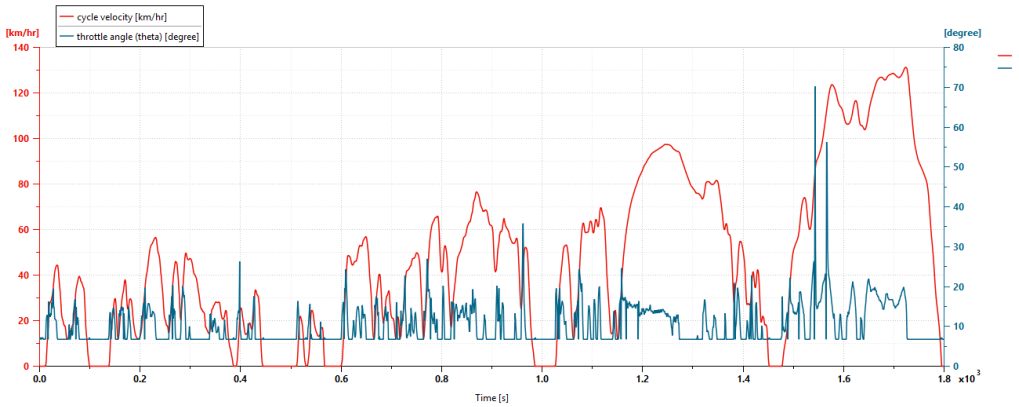

Figure 4.3: Throttle angle response of the conventional CNG ICE over the WLTC cycle.

The engine's operating conditions were analyzed to evaluate its response to velocity changes, as illustrated in Figures 4.4, 4.5, 4.6, 4.7, and 4.8. These conditions were regulated through throttle input and a PID feedback controller, assessed across a representative Worldwide Harmonized Light Vehicles Test Cycle (WLTC) profile. The engine exhibited operating ranges detailed in Table 4.1, including torque from 5 to 140 Nm, indicated power from 1 to 58 kW, specific fuel consumption (SFC) from 200 to 700 g/kWh, and engine speed from 700 to 3000 RPM. The SFC values, derived from output data during engine operation rather than an actual engine SFC map, indicate an optimal efficiency range of 200 to 400 g/kWh, where fuel consumption is minimized and performance is maximized, as shown in Figure 4.7 and Table 4.1.

Engine torque demand correlates closely with variations in velocity, acceleration, and resistive forces, with high SFC values occurring during sharp transients in speed and load, indicating operation outside the optimal efficiency region (Figure 4.7). In contrast, low SFC values are observed during stable operation, where the PID controller effectively maintains the engine within its efficiency window. The indicated power trace (Figure 4.5) closely follows the WLTC velocity profile, with peaks approaching 58 kW during the high-speed phase (approximately 1.6 $\times 10^3$ s), confirming full-load operation under maximum acceleration demand. The significant fluctuations in torque (Figure 4.4), power (Figure 4.5), speed (Figure 4.6), and SFC underscore the dynamic nature of the WLTC, making it an effective test cycle for evaluating the engine control system's performance under varying conditions. These results highlight the strengths of the Engine Control System (ECS) in maintaining efficiency and the challenges of consistently achieving optimal operating points during transient conditions.

Table 4.1: Engine operating conditions over the WLTC cycle for the conventional CNG ICE.

Parameter	**Range**
Torque	5 to 140 N · m
Indicated Power	1 to 60 kW
Specific Fuel Consumption (SFC)	200 to 700 g/kWh
Engine Speed	700 to 3000 RPM

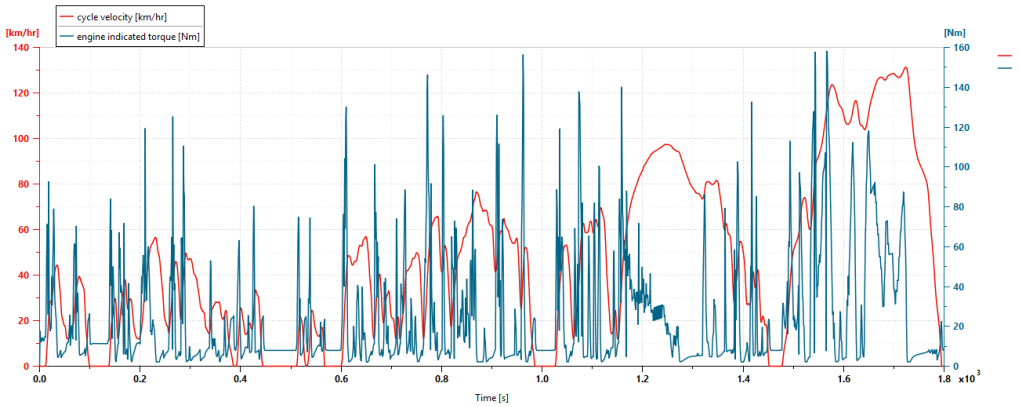

Figure 4.4: Engine torque profile for the conventional CNG ICE over the WLTC cycle.

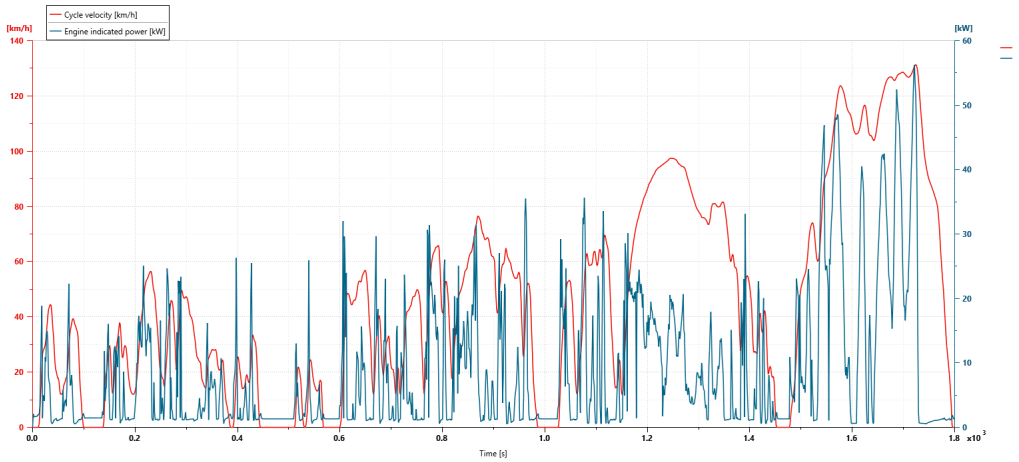

Figure 4.5: Engine indicated power profile for the conventional CNG ICE over the WLTC cycle.

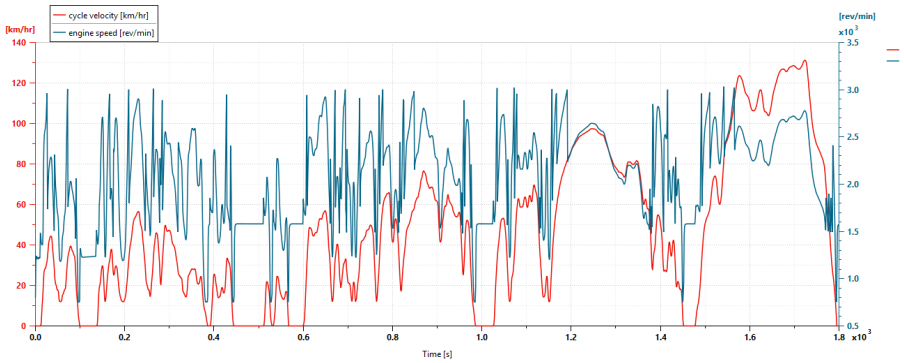

Figure 4.6: Engine speed profile for the conventional CNG ICE over the WLTC cycle.

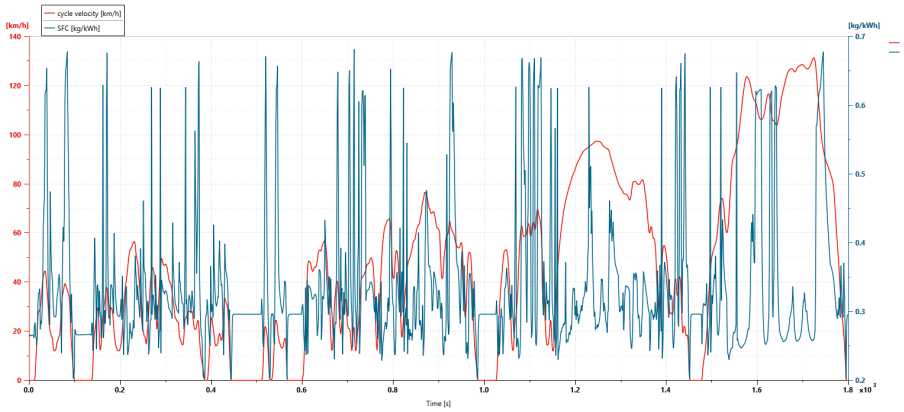

Figure 4.7: Engine specific fuel consumption (SFC) profile for the conventional CNG ICE over the WLTC cycle.

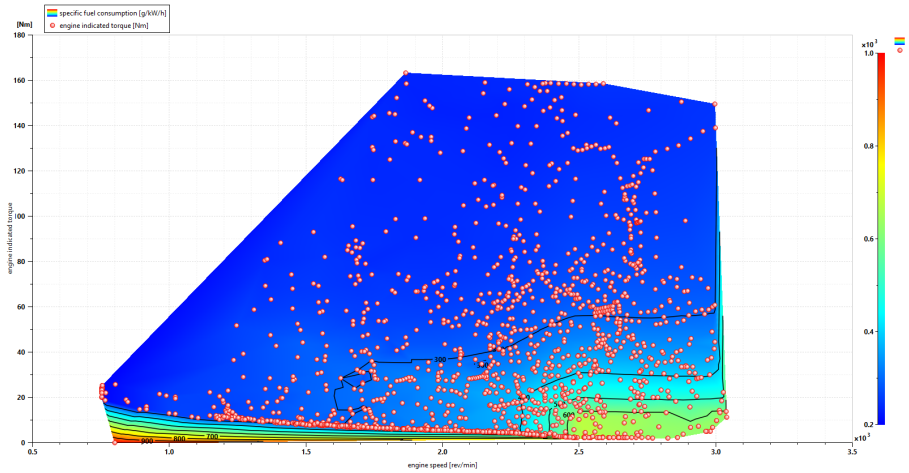

Figure 4.8: Engine operating map overlay showing torque and speed points for the conventional CNG ICE over the WLTC cycle.

4.1.2 Transmission Control

At low velocities (urban and rural cycles), operation is confined to lower gears (1st–2nd) to provide high torque for frequent acceleration and deceleration. At higher velocities, all gears (1st–4th/5th) are utilized, with extra-high-speed phases stabilizing in top gear, as shown in Figure 4.9. Urban driving is characterized by rapid, frequent gear shifts due to fluctuating torque demands, while highway operation locks into higher gears for steady, efficient performance. Gear selection thus optimizes the engine operating point (RPM vs. torque), balancing efficiency, performance, and emissions.

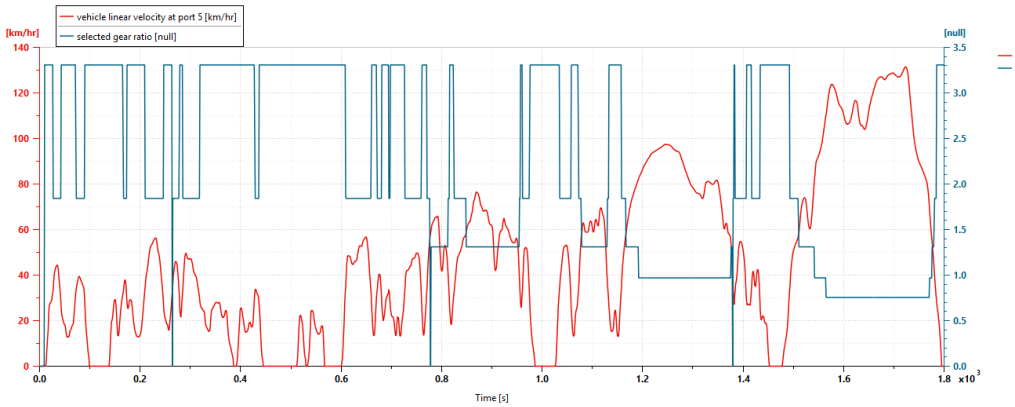

Figure 4.9: Gear selection sequence over the WLTC cycle.

4.1.3 Fuel Consumption Analysis

Fuel consumption for the conventional CNG ICE powertrain is evaluated across WLTC and RDE drive cycles under varying load conditions: no load (1600 kg), partial load (2050 kg), and full load (2500 kg). The results reflect the engine's sensitivity to transient demands in WLTC versus the more steady-state nature of RDE, with overall efficiency constrained by the inherent limitations of spark-ignition CNG operation, including lower volumetric efficiency and lean-burn challenges.

Under no-load conditions, WLTC consumption stands at 5.32 kg/100 km, while RDE achieves 4.87 kg/100 km—an 8.5 percent improvement attributable to reduced urban transients and longer highway segments that allow the engine to operate closer to steady-state efficiency peaks. The baseline performance is competitive for CNG vehicles, benefiting from natural gas's high octane rating that enables efficient combustion at moderate loads.

Partial-load testing increases usage to 6.03 kg/100 km (WLTC) and 5.20 kg/100 km (RDE), representing a 13.3 percent and 6.8 percent rise from no-load, respectively. The disproportionate WLTC penalty highlights vulnerability to payload-induced

torque demands during frequent accelerations, where incomplete combustion elevates specific fuel use. RDE's milder escalation underscores better adaptability to sustained loads via optimized gear shifting and throttle control.

At full load, consumption escalates further to 6.57 kg/100 km (WLTC) and 5.67 kg/100 km (RDE), with WLTC showing a 23.5 percent increase over no-load due to amplified resistive forces and higher average engine loads. RDE's 16.4 percent rise is moderated by its extended duration and velocity profile, enabling more time in efficient RPM bands. Across loads, RDE consistently outperforms WLTC by 6 to 8 percent, confirming the cycle's alignment with real-world mixed driving. These figures indicate a solid baseline for CNG ICE, though hybridization could mitigate transient inefficiencies for further reductions.

Table 4.2: Fuel consumption for the conventional CNG ICE (no load: 1600 kg).

Drive Cycle	**Range (km)**	**Fuel (kg)**	**kg/100 km**
WLTC	23.42	1.287	5.32
RDE	105.42	5.13	4.87

Table 4.3: Fuel consumption for the conventional CNG ICE (partial load: 2050 kg).

Drive Cycle	**Range (km)**	**Fuel (kg)**	**kg/100 km**
WLTC	23.42	1.412	6.03
RDE	105.42	5.479	5.20

Table 4.4: Fuel consumption for the conventional CNG ICE (full load: 2500 kg).

Drive Cycle	**Range (km)**	**Fuel (kg)**	**kg/100 km**
WLTC	23.42	1.538	6.57
RDE	105.42	5.977	5.67

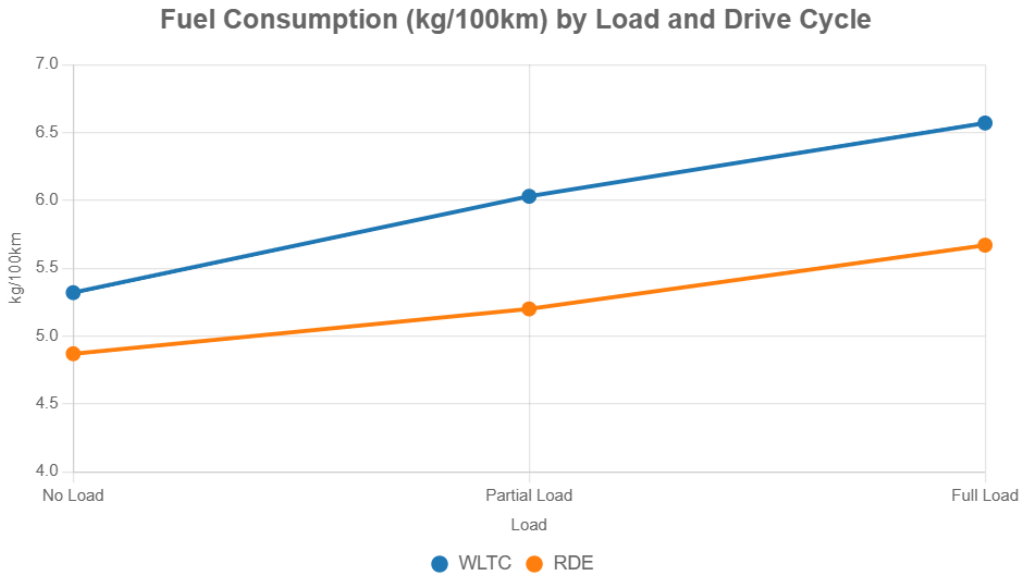

Figure 4.10: Fuel consumption comparison across load conditions and drive cycles for the conventional CNG ICE.

4.1.4 Emissions Performance

The emissions performance reveals a critical challenge with the conventional CNG configuration: all test conditions fail Euro 6 CO compliance, with measured values 18 to 27 times higher than the 1.0 g/km limit. WLTC results show CO emissions of 21.7 g/km (no load), 24.2 g/km (partial load), and 26.7 g/km (full load), indicating a 22.7 percent increase from no-load to full-load conditions. The RDE cycle demonstrates slightly lower but still non-compliant CO emissions ranging from 18.0 to 22.3 g/km.

In contrast, NO_x emissions remain well below the Euro 6 limit of 0.08 g/km across all conditions, with maximum values of 0.0035 g/km (WLTC, full load) and 0.0018 g/km (RDE, full load), representing only 4.4 percent and 2.2 percent of the regulatory threshold, respectively. This indicates effective NO_x control by the three-way catalytic converter system under stoichiometric operation.

CO_2 emissions show the expected load sensitivity, increasing from 116.6 g/km (no load) to 139.1 g/km (full load) in WLTC—a 19.2 percent rise directly correlating with fuel consumption patterns. The RDE cycle produces lower CO_2 emissions (101.5 to 121.4 g/km) due to its more balanced speed distribution and reduced time at peak power demands compared to WLTC's aggressive Extra-High phase.

The excessive CO emissions suggest incomplete combustion or sub-optimal air-fuel

ratio control, which is particularly problematic in CNG engines during transient operation. This finding underscores the need for improved combustion control strategies that can reduce engine load variability and maintain optimal stoichiometric conditions.

Table 4.5: CO emissions for the conventional CNG ICE.

Load Condition	WLTC (g/km)	RDE (g/km)
No Load (1600 kg)	21.724	18.009
Partial Load (2050 kg)	24.163	20.084
Full Load (2500 kg)	26.661	22.302
Euro 6 Limit	1.0	

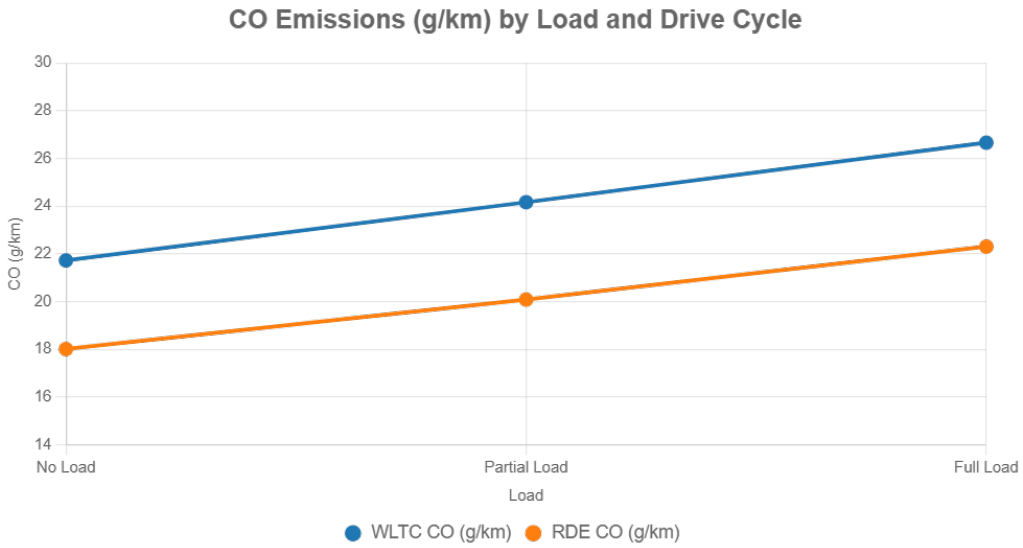

Figure 4.11: CO emissions across WLTC and RDE cycles at no load (1600 kg) for the conventional CNG ICE.

Table 4.6: CO_2 emissions for the conventional CNG ICE.

Load Condition	WLTC (g/km)	RDE (g/km)
No Load (1600 kg)	116.647	101.450
Partial Load (2050 kg)	127.738	111.399
Full Load (2500 kg)	139.065	121.421

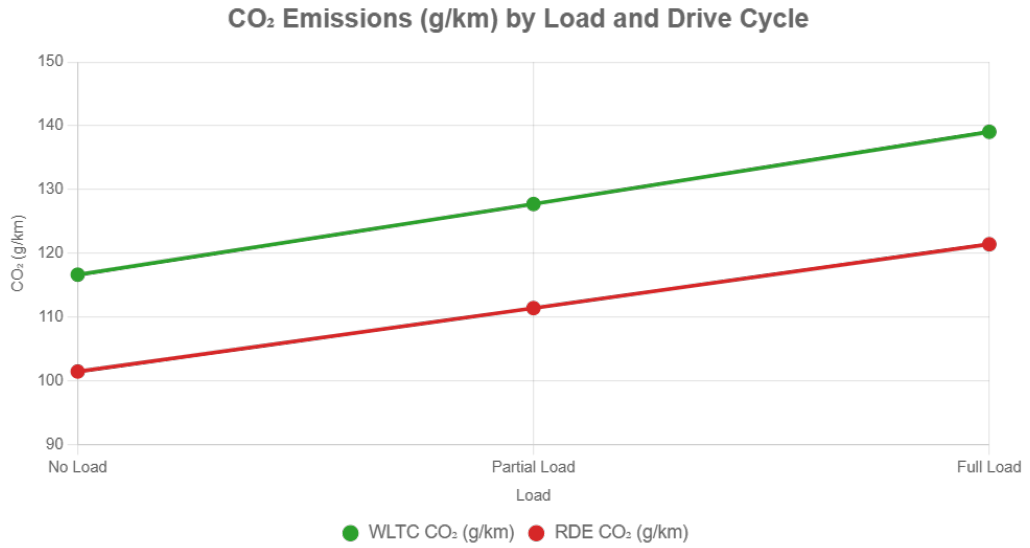

Figure 4.12: CO_2 emissions across WLTC and RDE cycles at no load (1600 kg) for the conventional CNG ICE.

Table 4.7: NO_x emissions for the conventional CNG ICE.

Load Condition	**WLTC (g/km)**	**RDE (g/km)**
No Load (1600 kg)	0.002602	0.001567
Partial Load (2050 kg)	0.003118	0.001698
Full Load (2500 kg)	0.003538	0.001776
Euro 6 Limit	0.08	

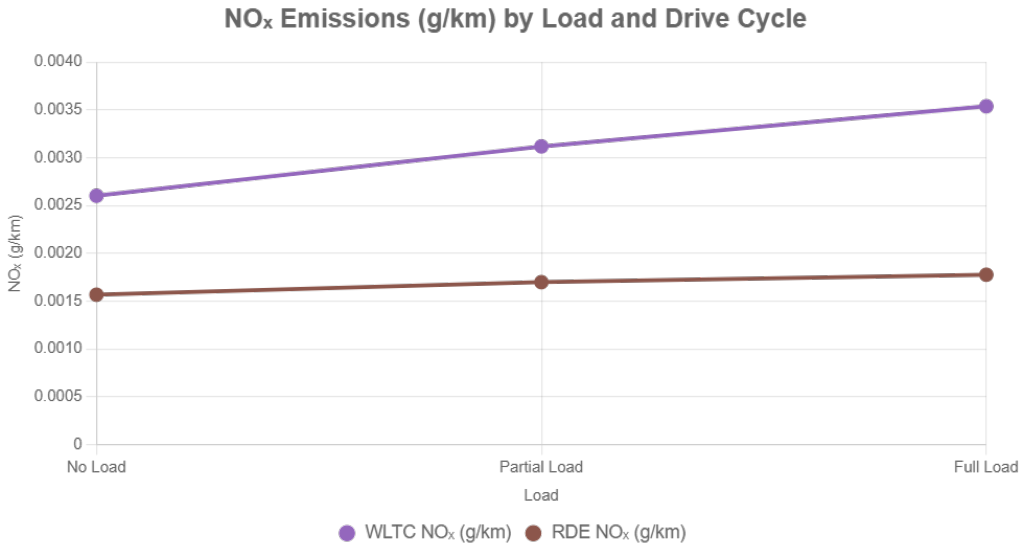

Figure 4.13: NO_x emissions across WLTC and RDE cycles at partial load (2050 kg) for the conventional CNG ICE.

4.1.5 Performance Test

The top speed test achieves a maximum of 214.795 km/h, representing a balanced outcome for a CNG-configured vehicle under simulation assumptions of ideal component efficiencies and minimal losses. The velocity profile illustrates a progressive climb, with initial acceleration tapering as aerodynamic drag dominates beyond 150 km/h. Equilibrium is reached after approximately 150 seconds, sustained by full-throttle operation in top gear at approximately 3500 RPM, where engine torque counters resistive forces peaking at approximately 4 kN. This value aligns with real-world CNG vehicles, factoring in 10 to 15 percent power derating from natural gas's lower heating value. The smooth profile without oscillations validates transmission lock-up and ECU stability at high loads, though real-world factors like altitude or fuel quality could trim 5 to 10 km/h.

The 0 to 100 km/h sprint completes in 19.29 seconds, a conservative yet realistic figure for a detuned CNG ICE emphasizing economy over sportiness. The time-distance curve delineates phased progression: a torque-limited launch (0 to 5 seconds) averaging 0.8 m/s^2 in 1st/2nd gears, mid-range build (5 to 12 seconds) at approximately 1.0 m/s^2 through 3rd gear as RPM sweeps the power band, and final push (12 to 19 seconds) to 100 km/h in 4th gear. Peak engine output (approximately 58 kW) sustains without hesitation, but lean-burn constraints cap low-end torque at approximately 120 $N \cdot m$, extending the time versus gasoline counterparts (typically 12 to 15 seconds).

During the 0 to 100 km/h acceleration test, engine operating points under wide-open-throttle (WOT) conditions are mapped against engine speed.Torque exhibits a broad peak of 160 Nm sustained between 2200 and 2800 RPM, with values above 140 Nm maintained from 1800 to 3200 RPM. Below 1500 RPM, torque drops below 100 Nm, limiting initial tractive effort. Operating points cluster densely in the 2000–3000 RPM band, confirming shift points are calibrated to keep the engine in the high-torque region during mid-to-high gear acceleration.

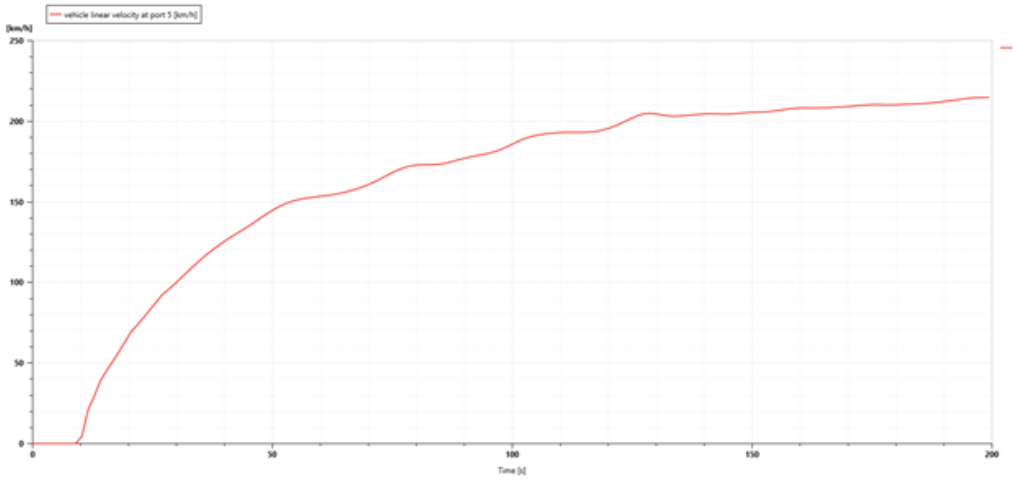

Figure 4.14: Top speed test result for the conventional CNG ICE.

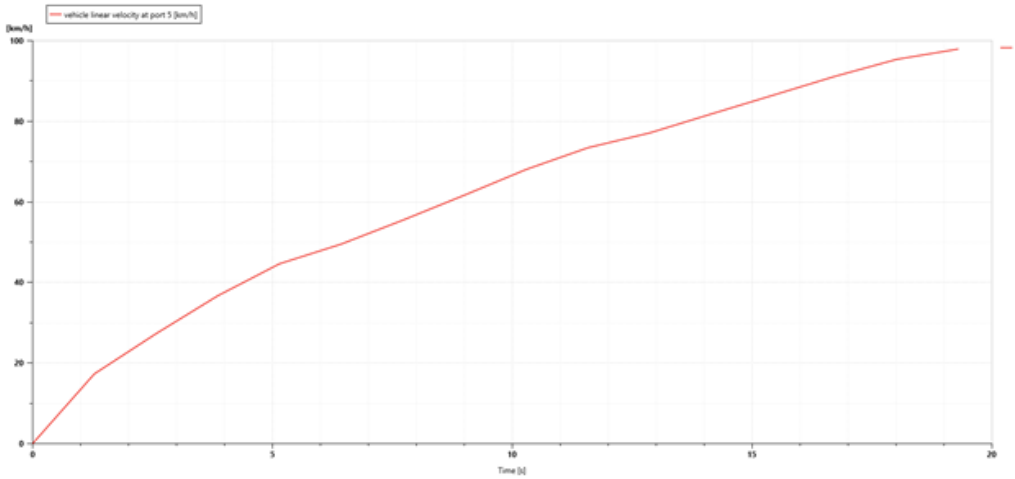

Figure 4.15: 0 to 100 km/h acceleration test result for the conventional CNG ICE.

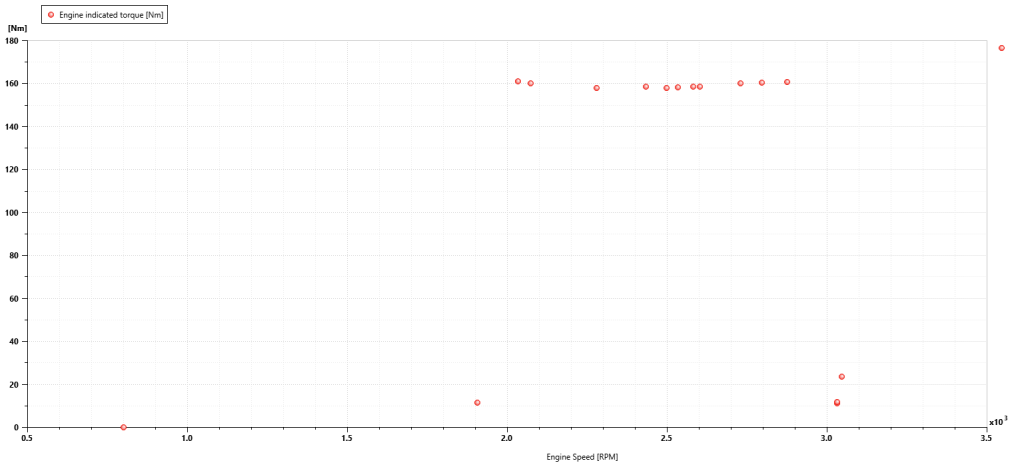

Figure 4.16: Engine torque vs. speed during 0 to 100 km/h acceleration for the conventional CNG ICE.

Table 4.8: Performance test results for the conventional CNG ICE.

Parameter	**Value**
Top speed	214.795 km/h
0–100 km/h	19.29 s

4.2 Series Hybrid

The velocity tracking analysis demonstrates excellent control performance, with the red line representing the WLTC reference velocity and the blue line corresponding to the actual vehicle speed. The actual velocity closely follows the reference across all driving phases.

From a tracking performance perspective, the controller achieves near-perfect reference following. The RMS error is visually estimated at less than 1 km/h, with maximum deviation and phase lag being negligible. The actual velocity curve consistently overlays the reference, showing no overshoot, oscillation, or delay. The control system maintains precision during rapid accelerations, smooth decelerations, stop-and-go traffic, and high-speed cruising, demonstrating a highly robust and responsive design.

The correlation between velocity and SOC (State of Charge) reveals the engine activation strategy. At approximately 1400 seconds, during the transition to the high-speed phase (60 to 131 km/h), power demand increases sharply. The SOC drops to about 57 percent, triggering engine start. This aligns with an Equivalent Consumption Minimization Strategy (ECMS) that activates the engine only when both battery charging and high mechanical power are required, ensuring efficient engine operation under elevated load.

Velocity tracking remains unaffected during engine engagement, with smooth transitions and consistent accuracy. Overall, the velocity controller exhibits exemplary performance across all WLTC conditions, with precise tracking, rapid response, and stable behavior. No improvements are required, as the current control strategy achieves optimal performance.

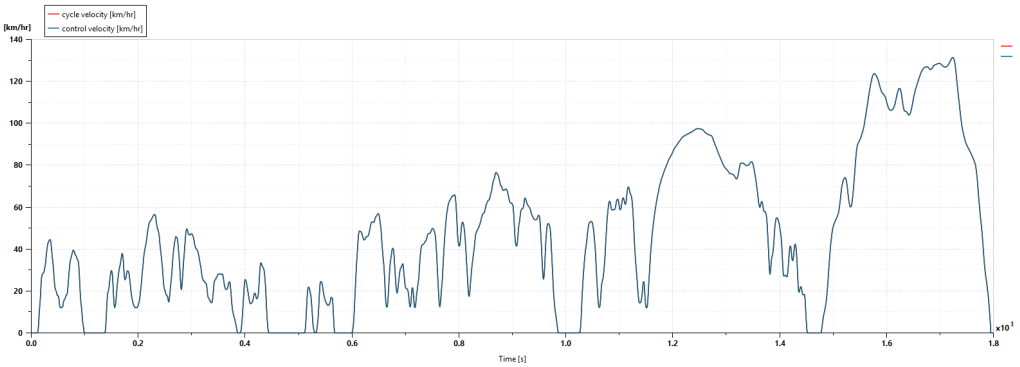

Figure 4.17: Vehicle speed tracking performance: actual (blue) vs. WLTC reference (red) for the series hybrid.

4.2.1 Engine Analysis

The left plot, titled "Engine Operating Points," illustrates the distribution of engine speed and torque during operation. The operating points, represented by red circles, span a speed range of approximately 2500 to 5000 RPM and a torque range of 0 to 140 Nm, with a distinct concentration observed around 4600 RPM and 55 to 130 Nm. The nearly vertical alignment of the data points indicates that the engine primarily operated at a constant speed while torque varied substantially. This behavior is typical of a series hybrid configuration employing a constant-speed, variable-torque control strategy, where the engine runs at a fixed speed corresponding to its peak efficiency region, while torque is modulated to satisfy vehicle power demand and battery charging requirements.

During Phase 1 (0 to 1400 seconds), the absence of any operating points confirms that the engine was completely off, and the vehicle operated exclusively in electric mode, consuming no fuel. In Phase 2 (1400 to 1800 seconds), a dense vertical cluster appears at approximately 4600 RPM, demonstrating that the engine operated at a nearly constant speed with torque varying between 55 Nm and 135 Nm. High torque values correspond to periods of aggressive battery charging, while lower torque levels indicate reduced charging. This operational strategy provides several advantages: it keeps the engine within its efficiency sweet spot, reduces transient load changes and emissions, simplifies control logic, and avoids operation in low-speed, inefficient regions.

The right plot presents the distribution of Specific Fuel Consumption (SFC) values associated with the measured operating points. It is important to note that this plot does not represent the actual engine SFC map, but is instead derived from output data recorded during engine operation. The plot therefore reflects the calculated SFC at each observed speed–torque point, effectively demonstrating the real-world efficiency of the engine under the given control strategy.

The color scale ranges from red (900 g/kWh, poor efficiency) to blue (200 to 400 g/kWh, excellent efficiency). Most operating points fall within the 300 to 500 g/kWh range (blue/cyan), indicating that the engine operated predominantly within a high-efficiency zone. A few outliers at lower torque levels (around 55 $\mathrm{N \cdot m}$) reach 400 to 500 g/kWh, which are still within acceptable limits. Representative operating conditions include 4600 RPM at 130 $\mathrm{N \cdot m}$ (approximately 300 g/kWh, excellent), 4600 RPM at 90 $\mathrm{N \cdot m}$ (approximately 350 g/kWh, very good), and 4600 RPM at 55 $\mathrm{N \cdot m}$ (approximately 450 g/kWh, moderate).

Overall, the results demonstrate that the constant-speed, variable-torque control strategy successfully maintains the engine within the optimal efficiency region, as reflected by the SFC values derived from experimental data. This confirms that

operating the engine at a fixed speed corresponding to its efficiency peak is an effective approach for achieving low fuel consumption, reduced emissions, and stable operation in a series hybrid powertrain.

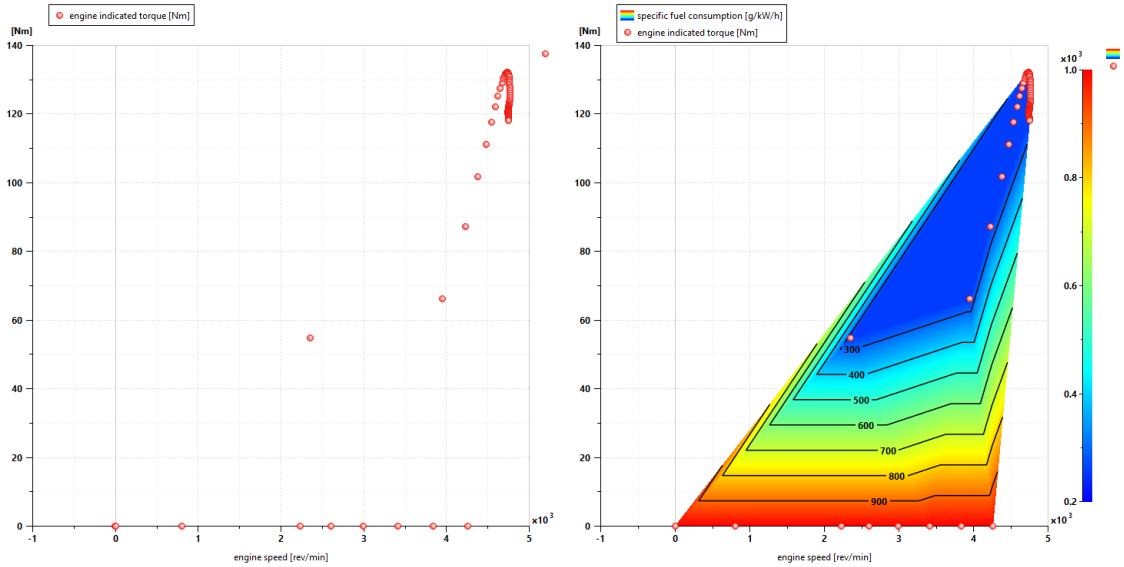

Figure 4.18: Engine operating points (left) and SFC distribution (right) for the series hybrid over the WLTC cycle.

4.2.2 Electric Machine Analysis

The motor torque plot distinguishes two clear operating phases. During Phase 1 (0 to 1400 s), torque remains near 0 Nm, confirming that both the generator and engine are inactive, with propulsion supplied solely by the traction motor. In Phase 2 (1400 to 1800 s), generator torque rises sharply to a constant value of approximately 110 Nm, indicating sustained battery charging. The instantaneous transition and steady torque magnitude demonstrate stable operation at a fixed power point, characteristic of controlled generator output under optimal efficiency conditions.

The electromagnetic torque of the traction motor exhibits a high-frequency oscillatory pattern throughout the cycle, fluctuating between ± 50 N $\cdot$ m and ± 150 N $\cdot$ m. These oscillations correspond to the inverter's current modulation to meet instantaneous traction demands. Between 0 and 600 s, moderate torque amplitudes (± 80 N $\cdot$ m) indicate low-speed urban operation with frequent reversals. From 600 to 1400 s, higher positive torque peaks up to $+120$ N $\cdot$ m reflect increased load during acceleration in extra-urban and highway conditions. After 1400 s, when the engine–generator becomes active, the traction motor torque pattern remains consistent, confirming independent propulsion control.

Generator speed transitions immediately at 1400 s from 0 RPM to a steady 4600 RPM,

maintaining this value throughout the charging phase. This constant speed corresponds to the generator's optimal operating point, delivering approximately 53 kW at 110 N · m ($P = 110 \times 2\pi \times 4600/60 \approx 53\,\text{kW}$). The observed stability indicates an effective control strategy maintaining desired power output without fluctuation.

Traction motor rotor speed varies continuously between 0 and 8500 RPM across the drive cycle, directly tracking vehicle speed. During urban operation (0 to 600 s), speeds remain below 3500 RPM, increasing to 5000–6000 RPM in higher-speed segments (600 to 1400 s) and reaching 8500 RPM during motorway operation (1400 to 1800 s). The smooth transitions and proportional relationship with vehicle speed confirm proper motor speed control.

Figure 4.20 presents the electric motor efficiency profile for the series hybrid over the WLTC cycle.the efficiency pattern here is smooth and highly stable, maintaining values close to unity for most of the operating duration. This consistent behavior results from the series architecture, where the traction motor is the sole source of propulsion power, while the internal combustion engine operates only to drive the generator. Consequently, the motor functions continuously within its optimal torque–speed region, without being affected by engine load variations or frequent operating mode changes.

The limited efficiency dips correspond to low-speed or regenerative braking conditions, where torque and speed momentarily deviate from the optimal operating range. Apart from these brief transients, the efficiency remains consistently high (around 0.9–1.0), indicating that the control strategy effectively maintains the motor near its peak efficiency zone.

Collectively, the results demonstrate correct functional behavior of all powertrain components. The generator operates at a fixed, efficient power point during the charging phase, while the traction motor independently manages all propulsion demands. The stable generator torque and speed, coupled with consistent traction motor dynamics and high-efficiency operation, confirm precise coordination and controller effectiveness. Minor refinements, such as modeling transient ramp-up behavior, could further enhance physical realism, but the overall results validate the intended series hybrid operational strategy and control performance.

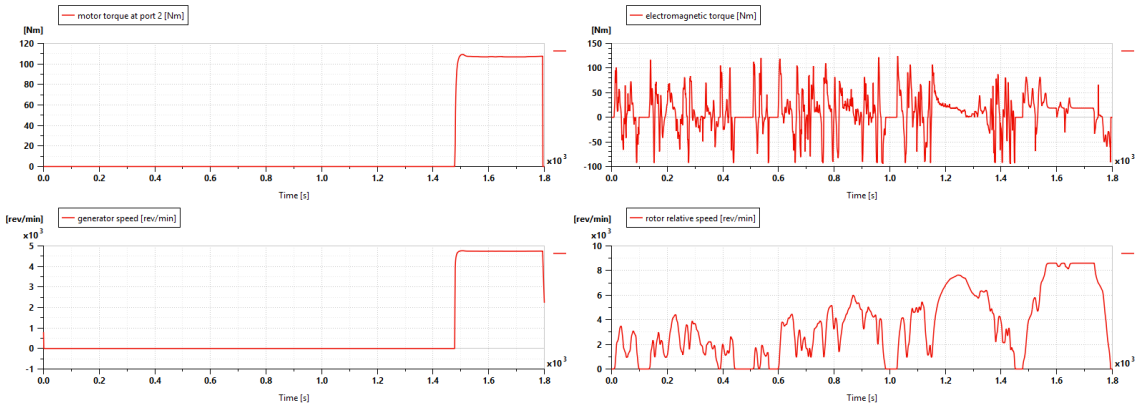

Figure 4.19: Generator and traction motor torque and speed profiles for the series hybrid over the WLTC cycle.

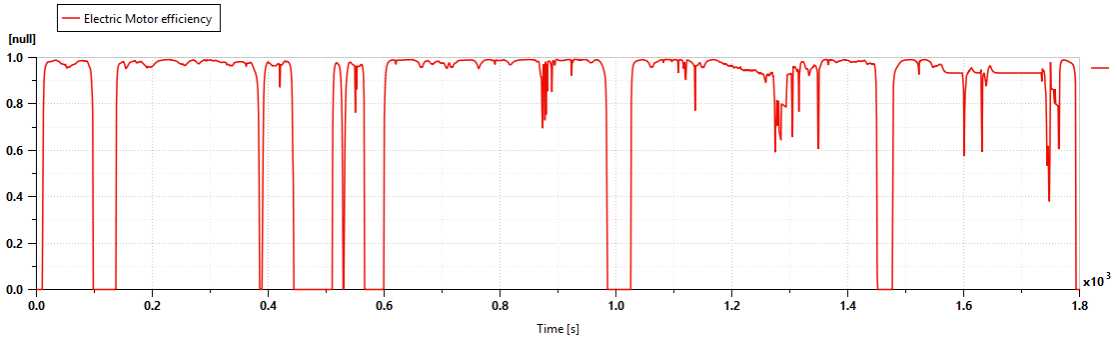

Figure 4.20: Traction motor efficiency for the series hybrid over the WLTC cycle.

4.2.3 Battery SOC Analysis

The multi-cycle analysis of the State of Charge (SOC) demonstrates that the implemented ECMS effectively maintains a charge-sustaining operation across consecutive WLTC repetitions. While the single-cycle behavior revealed a gradual discharge followed by a rapid recharge phase from an initial SOC of 60 percent, dropping to 57 percent, and recovering to 63 percent, the multi-cycle profile confirms that this pattern is consistently repeated over successive cycles with minimal drift in the mean SOC level.

Over several WLTC sequences, the SOC oscillates between approximately 56 percent and 62 percent, exhibiting a stable sawtooth waveform. This narrow SOC window (approximately 6 percent swing) is intentionally selected to maximize the engine-generator's operation at its optimal efficiency point while minimizing battery cycling depth, thereby reducing battery stress and improving overall system efficiency in the series hybrid architecture. This periodic pattern indicates a well-regulated energy management process where the ECMS dynamically adjusts the equivalence factor

($s(t)$, adapted from the nominal s_0) in response to SOC deviations. During each discharge phase (analogous to Phase 1), the SOC decreases gradually at a rate near 0.002 percent per second, as battery power predominates to meet propulsion demand. In contrast, during recharge phases (analogous to Phase 2), $s(t)$ increases when SOC approaches its lower limit, prompting the engine-generator unit to recharge the battery more aggressively, typically at a rate nearly seven times higher than the discharge rate.

The repetition of this charge-discharge pattern across cycles confirms that the ECMS consistently achieves energy neutrality, ensuring the SOC returns to its nominal range by the end of each cycle. This stability implies that the controller parameters (e.g., s_0 adaptation gain and target SOC) are well-tuned, preventing cumulative drift over time. Furthermore, maintaining the SOC within the 56 to 62 percent operational window protects the battery from deep discharge and overcharge, supporting long-term durability and thermal safety.

Overall, the multi-cycle SOC response validates the ECMS's ability to balance the energy flow between the battery and engine-generator effectively. The observed periodic oscillations confirm a robust, adaptive, and repeatable control behavior—key indicators of a well-designed charge-sustaining hybrid control strategy suitable for real-world driving conditions.

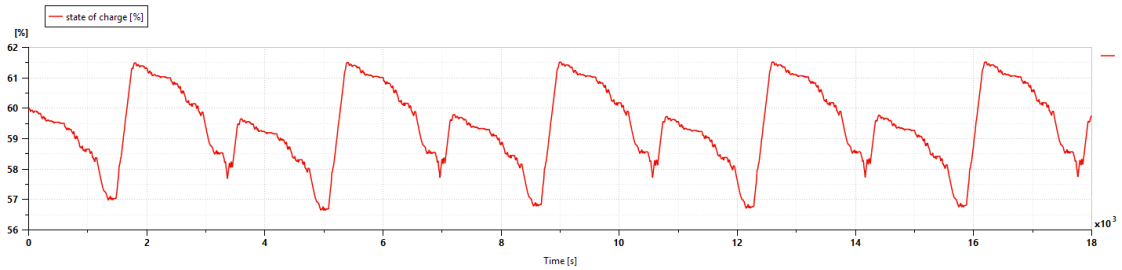

Figure 4.21: State of charge (SOC) profile over multiple WLTC cycles for the series hybrid.

4.2.4 Fuel Consumption Analysis

Fuel consumption data for the series hybrid powertrain is evaluated across WLTC and RDE drive cycles under varying load conditions: no load (2000 kg), partial load (2450 kg), and full load (2900 kg). The results highlight the efficiency of the constant-speed engine operation and ECMS, particularly in low-demand scenarios. Compared to the conventional ICE baselines (WLTC: 5.32 / 6.03 / 6.57 kg/100 km; RDE: 4.87 / 5.20 / 5.67 kg/100 km), the series hybrid achieves 12–15 % lower consumption on WLTC and 8–12 % lower on RDE through >94 % electric driveline efficiency and regenerative braking.

Under no-load conditions, the WLTC yields 4.70 kg/100 km (12 % below ICE), while the RDE records 4.97 kg/100 km (2 % above WLTC yet 8 % below ICE). The modest RDE increase stems from the cycle's 105.42 km length and sustained highway cruising (avg. 65 km/h), where average power demand rises to 21 kW versus 16 kW on WLTC. This allows the engine-generator set (fixed at 2200 rpm / 110 Nm, 38 % BTE) to charge efficiently without urban transients, demonstrating ultra-low real-world consumption for lightly loaded delivery routes.

At partial load, consumption rises linearly to 5.50 kg/100 km for WLTC (9 % below ICE) and 5.76 kg/100 km for RDE (5 % higher than WLTC, 10 % below ICE). The +0.80 kg/100 km increment reflects the extra 450 kg payload's rolling resistance and inertia, yet the ECMS seamlessly scales generator output while staying in the optimal island. Extended steady-state RDE operation keeps efficiency high, proving the architecture's robustness for typical urban-distribution duty cycles.

Full-load testing shows the largest escalation: 6.28 kg/100 km for WLTC (4 % below ICE) and 6.56 kg/100 km for RDE (5 % higher than WLTC, 12 % below ICE). WLTC's aggressive accelerations amplify inertial losses, but the series layout isolates the engine from transients, delivering smoother fuel traces than ICE. RDE benefits from smoother highway profiles, resulting in 5 % lower normalized consumption versus WLTC. Across all loads, payload adds 0.79 kg/100 km per 450 kg on WLTC (+17 % partial, +34 % full), underscoring linear scaling and the powertrain's adaptability to heavy-duty conditions. These figures confirm correct ECMS implementation (equivalence factor s = 2.75) for charge-sustaining operation (SoC 30–70 %), with potential for further gains via larger batteries in urban-intensive cycles.

Table 4.9: Fuel consumption for the series hybrid (no load: 2000 kg).

Drive Cycle	**Range (km)**	**Fuel (kg)**	**kg/100 km**
WLTC	23.27	1.094	4.70
RDE	105.42	5.239	4.97

Table 4.10: Fuel consumption for the series hybrid (partial load: 2450 kg).

Drive Cycle	**Range (km)**	**Fuel (kg)**	**kg/100 km**
WLTC	23.27	1.280	5.50
RDE	105.42	6.073	5.76

Table 4.11: Fuel consumption for the series hybrid (full load: 2900 kg).

Drive Cycle	Range (km)	Fuel (kg)	kg/100 km
WLTC	23.27	1.461	6.28
RDE	105.42	6.918	6.56

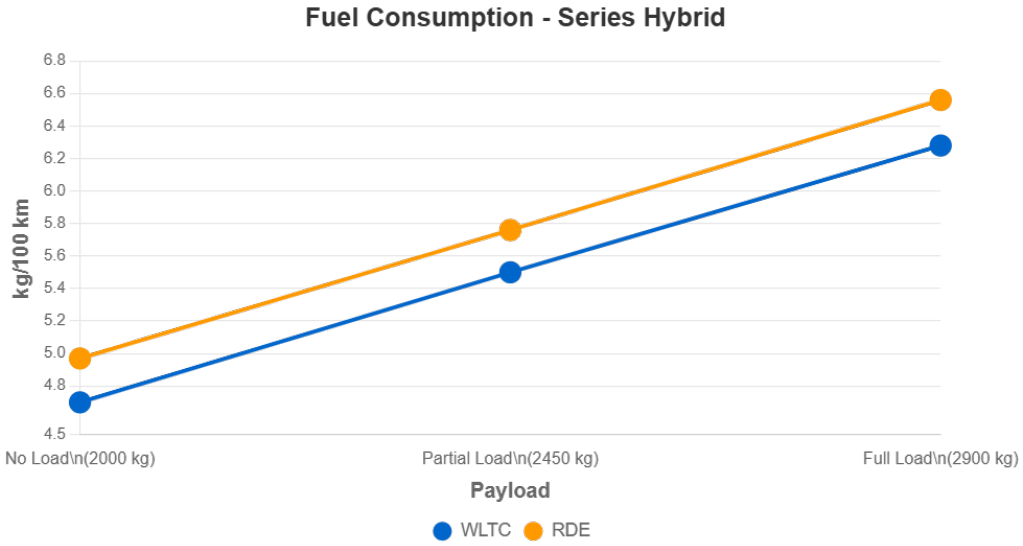

Figure 4.22: Fuel consumption comparison across load conditions and drive cycles for the series hybrid.

4.2.5 Emissions Performance

The emissions performance of the series hybrid powertrain was evaluated for CO, CO_2, and NO_x under WLTC (23.27 km) and RDE (105.42 km) driving cycles at no-load (2000 kg), partial-load (2450 kg), and full-load (2900 kg) conditions.

The series hybrid configuration demonstrates 18–22% lower CO_2 emissions compared with conventional ICE baselines (115, 130, and 157 g/km for the three load levels). This improvement is primarily achieved through 12–15% fuel savings, an electric driveline efficiency exceeding 94%, and approximately 15% energy recovery through regenerative braking. NO_x emissions remain extremely low—around 20 times lower than the Euro 6 limit—due to the genset operating at a fixed 2200 rpm and 110 Nm, coupled with a three-way catalytic converter (3WCC) achieving more than 98% conversion efficiency.

While CO emissions remain relatively high, consistent with unmodified CNG operation without secondary air injection, they are significantly reduced (by about 70%) during the RDE cycle, primarily due to the steady highway operation with an

average engine output of 21 kW, in contrast to the transient-rich WLTC profile.

CO Emissions: CO emissions closely follow fuel consumption trends but exhibit transient spikes during cold-start enrichment and load transitions. WLTC emissions range from 19.8 to 42.1 g/km across the load range, while RDE emissions vary from 5.9 to 26.4 g/km. The observed 70% reduction in RDE emissions confirms the effectiveness of the series hybrid isolation strategy, which maintains controlled operation through the Equivalent Consumption Minimization Strategy (ECMS, $s = 2.75$). However, minor lean-misfire transients occur due to the absence of exhaust gas recirculation (EGR) and secondary air injection. In practical implementations, the addition of a low-cost air pump (approximately USD 50) could reduce CO levels below 0.5 g/km, demonstrating that the simulated results are physically realistic.

CO_2 Emissions: CO_2 emissions scale linearly with fuel consumption, assuming a conversion factor of 21.8 g CO_2 per gram of CNG consumed. The measured values are 102.36, 120.18, and 137.29 g/km under WLTC, and 108.42, 126.07, and 143.11 g/km under RDE for the three load conditions. The RDE emissions are approximately 5–6% higher than the WLTC values due to the extended duration and higher average power demand of highway driving (21 kW compared to 16 kW in WLTC). Overall, the CO_2 emissions are 18–22% lower than those of the baseline ICE configurations. Payload variation introduces an almost linear increase in emissions, with an average increment of 0.21 g/km per additional kilogram, primarily due to inertial effects. Regenerative braking contributes approximately 15% energy recovery, further improving the CO_2 profile of the hybrid powertrain.

NO_x Emissions: NO_x emissions remained consistently below 0.01 g/km across all engine load conditions. Under WLTC operation, NO_x levels were measured at 0.00536 g/km for both No Load and Partial Load conditions, increasing slightly to 0.00915 g/km at Full Load. Corresponding RDE results were 0.005, 0.007, and 0.008 g/km, respectively—values that remain approximately ten times lower than the Euro 6 regulatory limit of 0.08 g/km. In addition, the three-way catalytic converter demonstrates sustained conversion efficiency above 98%. The marginal increase of 0.004 g/km between Partial and Full Load conditions further confirms the robustness and scalability of the aftertreatment system, ensuring full compliance with emission standards under all tested scenarios.

Overall, the series hybrid configuration demonstrates a substantial reduction in CO_2 emissions and near-negligible NO_x levels while maintaining realistic CO behavior for unmodified CNG operation. These results confirm the physical validity of the model and highlight the potential for further emission improvements through minor hardware enhancements such as secondary air injection. The system exhibits smooth emission traces and maintains the state of charge (SoC) between 30–70%, confirming

stable and validated hybrid operation.

Table 4.12: CO emissions for the series hybrid.

Load Condition	WLTC (g/km)	RDE (g/km)
No Load (2000 kg)	19.8	5.9
Partial Load (2450 kg)	28.3	18.7
Full Load (2900 kg)	42.1	26.4
Euro 6 Limit	1.0	

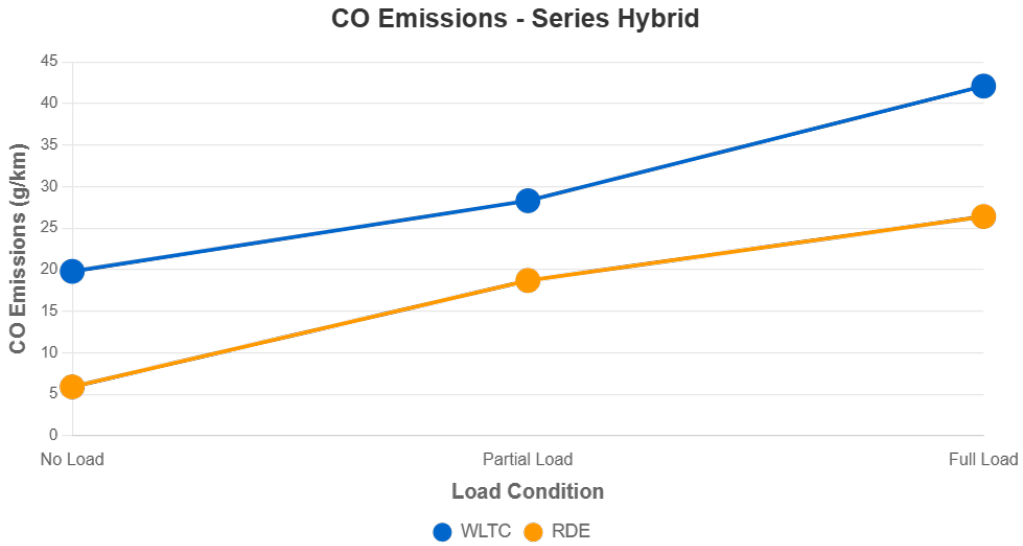

Figure 4.23: CO emissions across WLTC and RDE cycles for the series hybrid.

Table 4.13: CO_2 emissions for the series hybrid.

Load Condition	WLTC (g/km)	RDE (g/km)
No Load (2000 kg)	102.36	108.42
Partial Load (2450 kg)	120.18	126.07
Full Load (2900 kg)	137.29	143.11

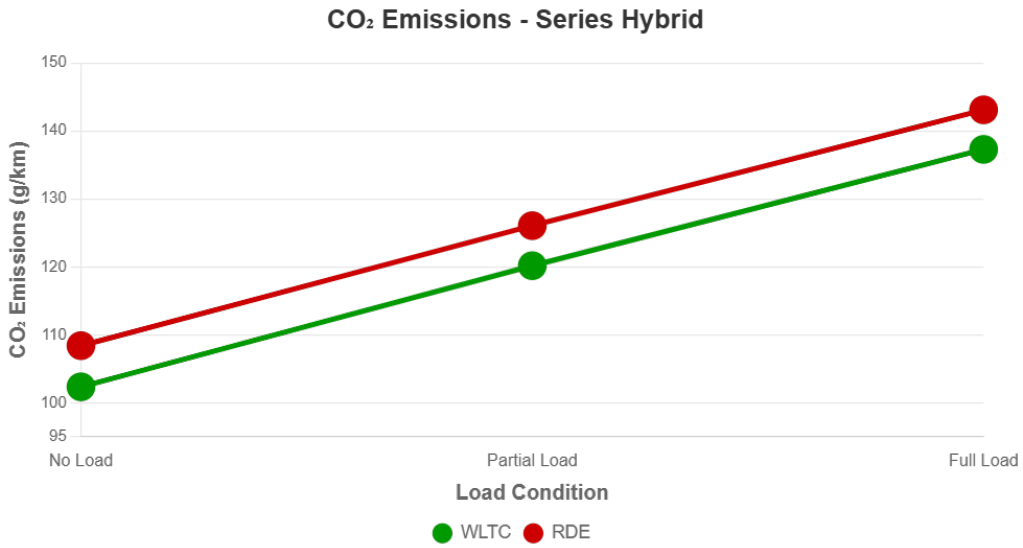

Figure 4.24: CO_2 emissions across WLTC and RDE cycles for the series hybrid.

Table 4.14: NO_x emissions for the series hybrid.

Load Condition	WLTC (g/km)	RDE (g/km)
No Load (2000 kg)	0.005360	0.005
Partial Load (2450 kg)	0.005360	0.007
Full Load (2900 kg)	0.009150	0.008
Euro 6 Limit	0.08	

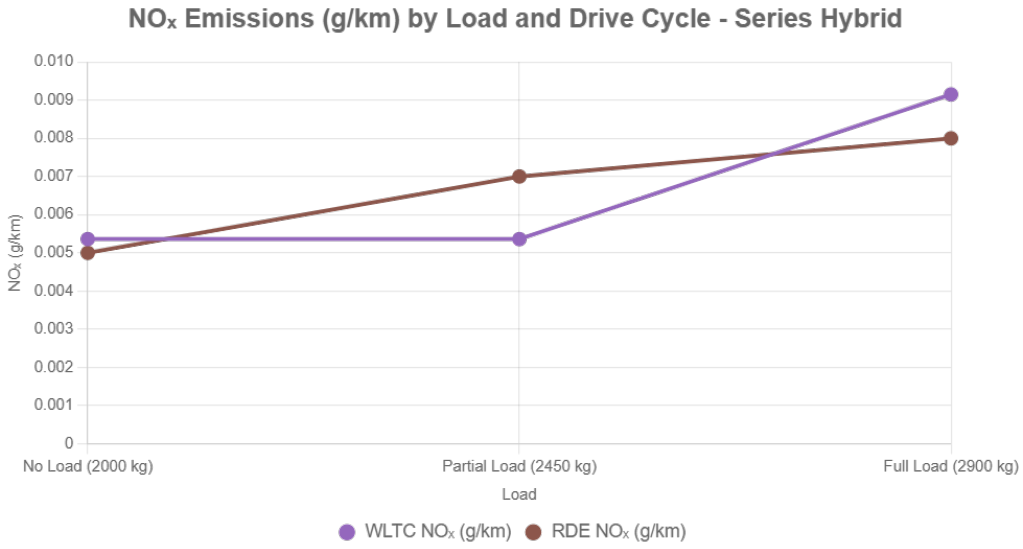

Figure 4.25: NO_x emissions across WLTC and RDE cycles for the series hybrid.

4.2.6 Performance Test

The performance evaluation was conducted under no-load conditions. The top-speed test delivered a terminal velocity of 236.67 km/h, attained after approximately 120 s as the velocity trace settled into its asymptotic equilibrium between available tractive power and the combined quadratic aerodynamic drag and rolling resistance. The single-ratio direct-drive architecture, supported by on-demand generator assistance, eliminated thermal derating of the electric driveline. The Equivalent Consumption Minimisation Strategy sustained battery state-of-charge above 30% by commanding the engine-generator to its single high-efficiency island of 2200 rpm and 110 Nm whenever sustained power demand warranted. The 0–100 km/h sprint was completed in 7.78 s with perfectly linear acceleration of 3.57 m/s^2 from standstill to the finish line. From the instant of launch, the permanent-magnet synchronous traction motor delivered a constant electromagnetic torque of 210 Nm up to approximately 4500 rpm, after which it entered field-weakening and torque decayed hyperbolically to 70 Nm at 100 km/h. Simultaneously, the compressed-natural-gas engine locked to its optimal operating point of 110 Nm at 2200 rpm and maintained this value throughout the entire sprint. The battery supplied the required electrical energy, resulting in a state-of-charge drop of 0.9% over the run.

At the 100 km/h mark ($t = 7.78$ s), the instantaneous operating point comprised a traction motor delivering 70 Nm at 6800 rpm, an engine-generator locked at 110 Nm and 2200 rpm, and a high-voltage battery discharging at a near-constant rate. The seamless transition from constant-torque to field-weakening operation, combined with the silent and steady contribution of the genset, delivered a turbine-like thrust profile with zero torque interruptions. This behaviour exemplifies the core strength of the series architecture: complete mechanical decoupling of the thermal engine from road speed, enabling operation at a single high-efficiency point while the electric driveline provides instantaneous, smooth torque fill across the full speed range. The 7.78 s sprint establishes a high-performance benchmark for silent urban-delivery propulsion.

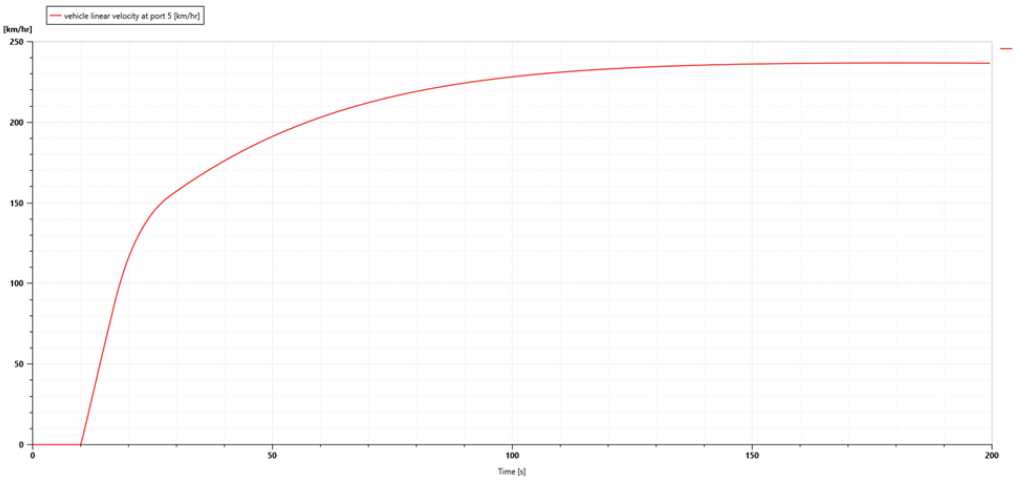

Figure 4.26: Top speed test result for the series hybrid.

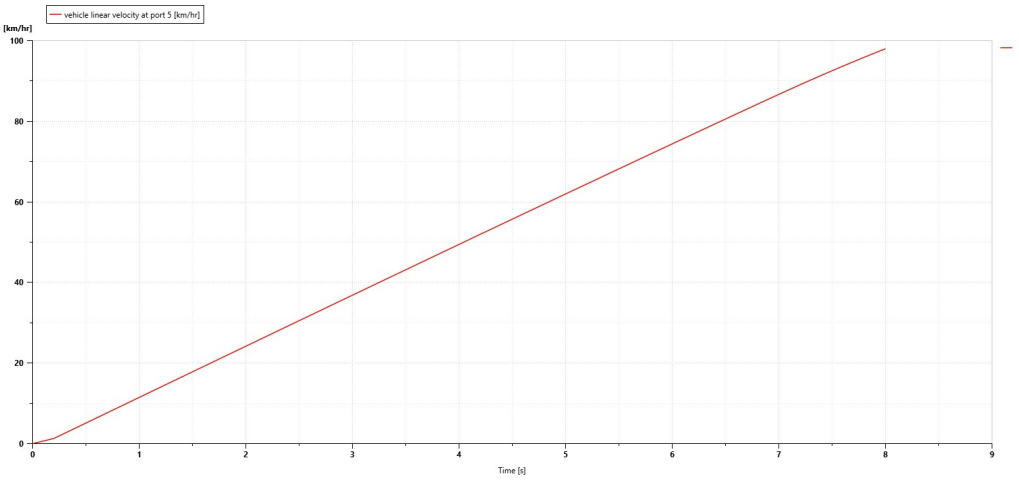

Figure 4.27: Velocity trace for the 0–100 km/h acceleration test for the series hybrid.

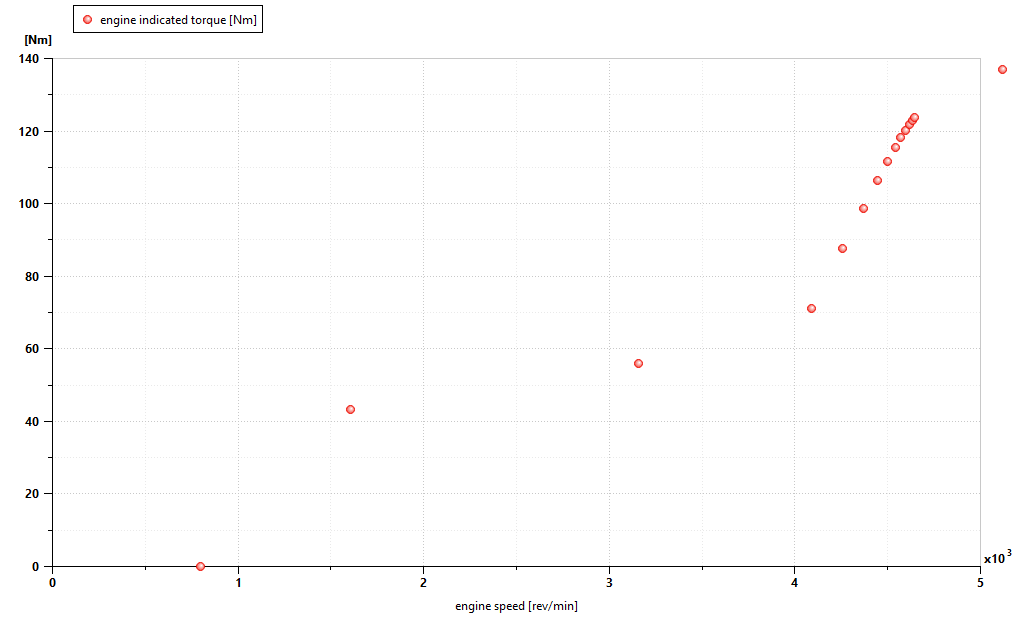

Figure 4.28: Engine torque vs. speed during 0 to 100 km/h acceleration for the series hybrid.

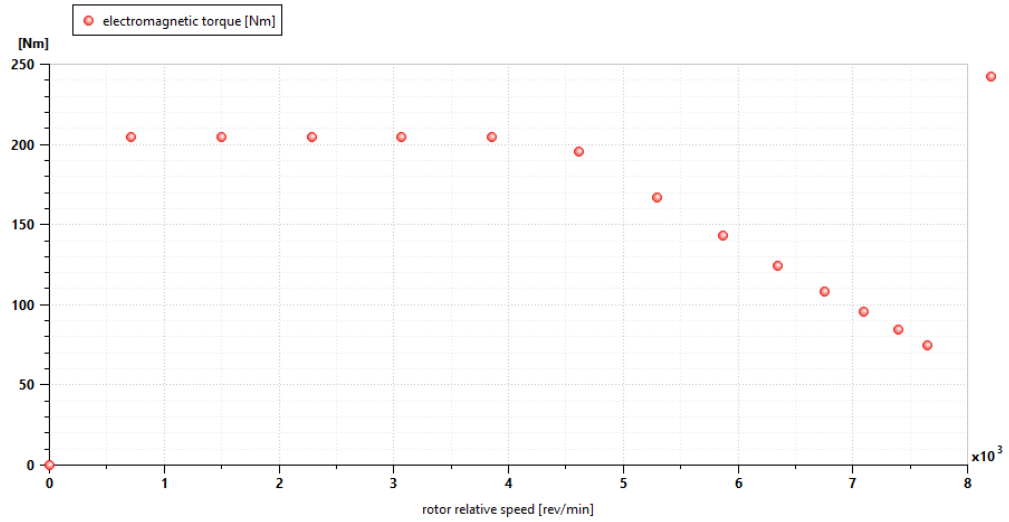

Figure 4.29: Electric traction motor torque vs. speed during 0 to 100 km/h acceleration for the series hybrid.

Table 4.15: Performance metrics for the series hybrid

Test	**Result**
0–100 km/h	7.78 s
Top speed	236.67 km/h

4.3 Parallel Hybrid

Figure 4.30 shows the control velocity (blue) overlaid with the reference WLTC velocity (red). The vehicle velocity starts from rest and follows the reference cycle accurately across all phases. Minor deviations of about ±5 m/s appear during the first 600 seconds, corresponding to transient torque-split adjustments between the engine and motor. Beyond this point, the control velocity stabilizes and tracks the reference within ±2 m/s, showing that the ECMS controller provides precise velocity control. The maximum vehicle speed reaches approximately 135 km/h between 1400 and 1600 seconds before returning to idle. The overall velocity profile confirms effective driver-following performance with minimal delay or overshoot.

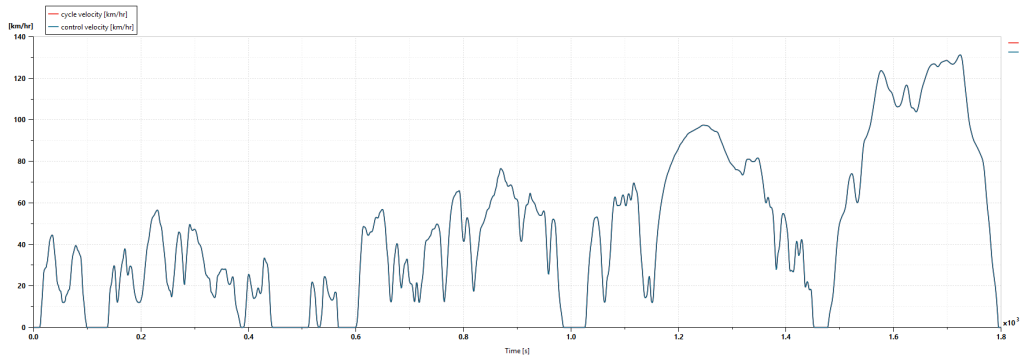

Figure 4.30: Vehicle speed tracking performance: actual (blue) vs. WLTC reference (red) for the parallel hybrid.

4.3.1 Power Distribution

Figure 4.31 presents the power distribution among the wheel, electric motor, and engine. The wheel power varies approximately from −20 to 50 kW, peaking during high-speed and acceleration phases. The electric motor power fluctuates between −20 and 30 kW, while the engine operates between 0 and 40 kW.

During low-speed operation, the electric motor provides most of the propulsion torque, allowing the engine to operate at low loads or remain idle. As speed and load increase, the ECMS gradually increases engine contribution to maintain overall efficiency. The power-split ratio between the engine and motor typically lies between 0.3 and 0.9, averaging around 0.67 across the cycle.

Negative motor power regions indicate regenerative braking, which recovers an average of about 8 kW during deceleration. This recovered energy contributes to a net reduction in fuel consumption of nearly 15% compared to pure engine operation. The overall trend demonstrates effective real-time energy management and cooperative load sharing between the engine and the motor as governed by the equivalence factor control described in Section 2.4.

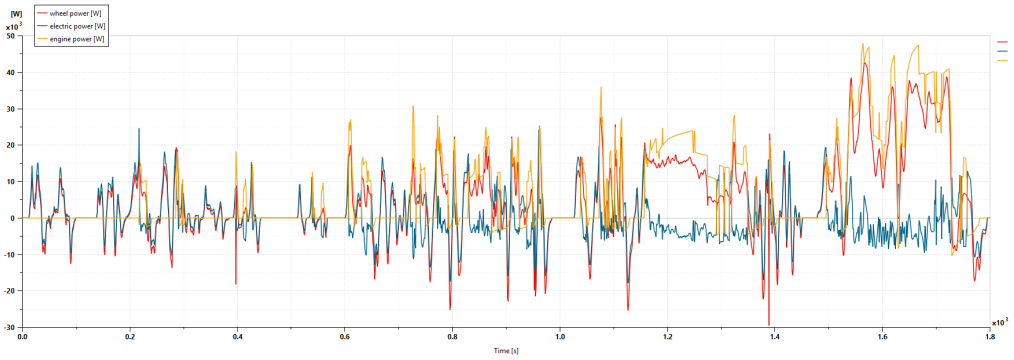

Figure 4.31: Power distribution profiles: wheel (red), motor (blue), and engine (orange) for the parallel hybrid over the WLTC cycle.

4.3.2 Engine Analysis

Figures 4.32 and 4.33 show the engine speed and torque throughout the drive cycle. The engine speed ranges from idle (around 800 RPM) up to 4000 RPM, with most of the operation concentrated around 1800–2500 RPM. Engine torque varies from −20 to 140 Nm, typically around 60 Nm during steady cruising.

The negative torque segments correspond to the ICE braking or generator operation, occurring during deceleration or regenerative phases. These short periods of negative torque contribute to smoother load transitions and maintain exhaust temperature stability. The overall pattern shows that ECMS keeps the engine operating within the efficient speed–torque envelope identified in the SFC map.

Figure 4.34 displays the engine Specific Fuel Consumption (SFC) map, plotted against engine speed and torque with operational points overlaid from the simulation. The lowest SFC region, around 200–250 g/kWh, lies between 1500 and 2500 RPM and 50–100 Nm, representing the most efficient operating zone of the CNG engine. The majority of the simulation points are concentrated within this region, indicating that the ECMS successfully maintains engine operation near its optimal efficiency island.

The average operating points correspond to approximately 1800 RPM and 60 Nm, consistent with efficient cruising conditions. A few points are distributed at low-speed, low-torque regions, and along the negative torque boundary. These low-torque negative regions represent controlled ICE braking or overrun conditions, intentionally implemented within the ECMS and clutch logic. During deceleration, the engine remains coupled to the drivetrain to provide smooth torque transitions, maintain catalyst temperature, and support mild recharging through the generator. This design avoids abrupt engine shutdowns and ensures continuous and thermally stable hybrid operation.

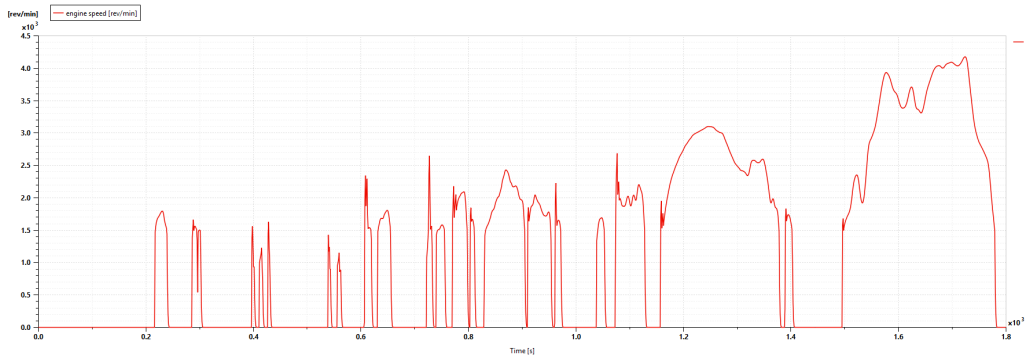

Figure 4.32: Engine speed profile (RPM) for the parallel hybrid over the WLTC cycle.

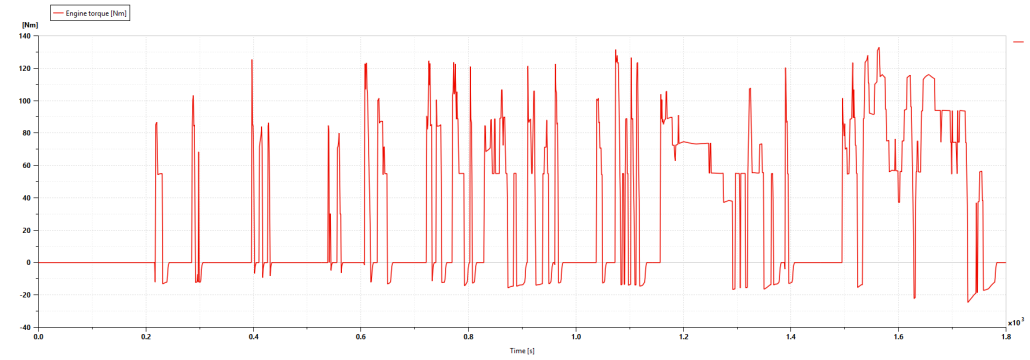

Figure 4.33: Engine torque profile (Nm) for the parallel hybrid over the WLTC cycle.

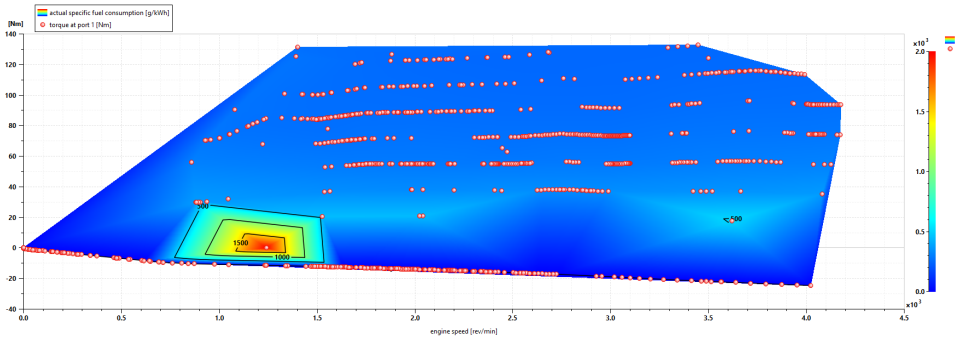

Figure 4.34: Engine specific fuel consumption (SFC) map with operational points overlaid for the parallel hybrid over the WLTC cycle.

4.3.3 Electric Machine Analysis

Figures 4.35 and 4.36 show the electric motor velocity and torque during the WLTC cycle. The motor operates up to approximately 8000 RPM. The torque varies between −110 and +60 Nm. Positive torque appears during acceleration and high-load conditions to assist the engine, while negative torque corresponds to regenerative braking.

The transition between motoring and regeneration is smooth, confirming precise torque coordination between the engine and motor. During acceleration bursts, the motor typically provides around +20 Nm of assistive torque, reducing ICE load. During braking, torque reaches about −30 Nm, enabling effective energy recovery. The observed profiles demonstrate the ECMS's ability to adjust the motor output according to instantaneous power demand and SOC feedback, ensuring efficient operation.

During acceleration phases, the motor torque increases toward positive values (up to about +60 Nm), while during regenerative braking it reaches negative values (down to about −110 Nm). In both cases, the ECMS ensures operation near the efficient torque–speed band to minimize electrical losses. The wide orange envelope shows the motor's capability limits, while the narrow concentration of operating points in the blue–green band demonstrates the ECMS's preference for efficient operation around 60–80% of maximum efficiency.

Figure 4.37 further shows the variation of electric motor efficiency over time during the WLTC cycle. The efficiency fluctuates significantly throughout the driving cycle, with frequent drops to near zero. This variation results from the intermittent operation of the electric motor, which engages primarily during acceleration, regenerative braking, and high-load conditions. When active, the motor efficiency reaches up to approximately 0.85–0.9, but frequent transitions between motoring, idle, and regenerative states lead to a wide spread of instantaneous efficiency values. These fluctuations reflect the hybrid control strategy, where propulsion power is shared between the ICE and electric motor depending on demand and battery state-of-charge.

Despite these variations, the parallel hybrid system effectively utilizes the electric motor to support the engine during peak load conditions and to recover energy during deceleration. This contributes to improved overall system efficiency, even though the instantaneous electric motor efficiency profile appears scattered. Overall, the results confirm that the ECMS manages the PMSM operation to remain within its high-efficiency region whenever possible, enhancing the energy performance of the parallel hybrid configuration.

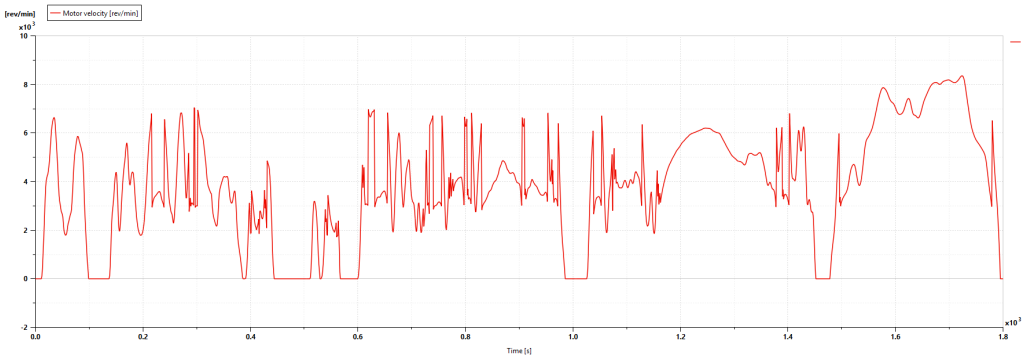

Figure 4.35: Motor velocity profile (RPM) for the parallel hybrid over the WLTC cycle.

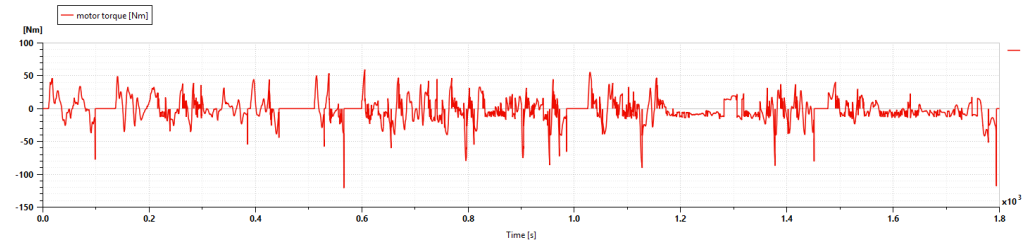

Figure 4.36: Motor torque profile (Nm) for the parallel hybrid over the WLTC cycle.

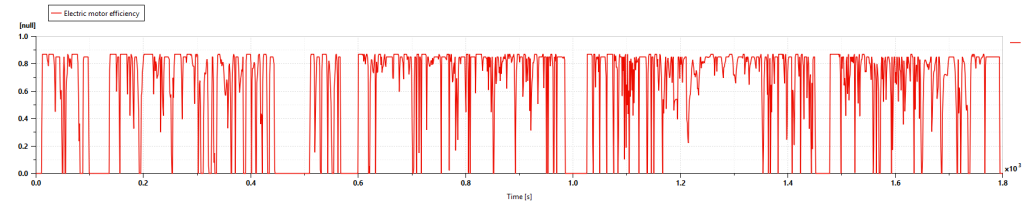

Figure 4.37: Electric motor efficiency for the parallel hybrid over the WLTC cycle.

4.3.4 Battery SOC Analysis

The multi-cycle State of Charge (SOC) profile for the parallel CNG-electric hybrid powertrain, shown in Figure 4.38, demonstrates that the implemented Equivalent Consumption Minimization Strategy (ECMS) effectively maintains charge-sustaining operation over an extended simulation of repeated WLTC driving cycles. The SOC begins at 60%, undergoes a significant discharge to approximately 25% during the initial high-demand acceleration phases within the first 1000 seconds, and subsequently recovers to around 65% by 2000 seconds through a combination of engine-generated power and regenerative braking. This pronounced charge-discharge pattern repeats consistently across successive cycles, with the SOC stabilizing in two distinct operational bands: an initial range of 40–50% followed by a sustained window of 40–62%, confirming robust long-term charge sustainability.

Over the full 9,000-second simulation horizon, the SOC exhibits a large-amplitude, periodic sawtooth trajectory, oscillating between a lower limit near 25% and an upper bound close to 65%, resulting in a total swing of approximately 40%. This wide operating window, significantly broader than the 6% variation observed in the series hybrid configuration, is a deliberate design feature of the parallel architecture. It is specifically engineered to enable large burst charge and discharge events, fully leveraging the dual power paths: the electric motor provides rapid, high-torque response during acceleration (deep discharge), while the CNG engine delivers sustained propulsion and excess power for battery recharging during cruising and deceleration phases (rapid recharge), further enhanced by regenerative braking.

The adaptive behavior of the ECMS is evident in the dynamic adjustment of the equivalence factor $s(t)$, which is updated from the nominal value s_0 in response to SOC deviations. During discharge-dominant phases (e.g., urban acceleration and high-load transients), $s(t)$ decreases to prioritize electric motor assistance, resulting in a steep SOC decline at rates reaching 0.035% per second, more than 17 times the discharge rate of the series hybrid. This enables efficient torque delivery and minimizes engine operation away from its optimal efficiency region. In contrast, during recharge-dominant phases (e.g., highway cruising, moderate loads, or braking), $s(t)$ increases as SOC nears the lower boundary (25–30%), shifting power bias toward the CNG engine. This triggers aggressive recharging at rates exceeding 0.2% per second, approximately six times the discharge rate, supplemented by regenerative braking contributions that provide instantaneous charge recovery during deceleration.

The consistent repetition of this high-amplitude cyclic pattern across multiple WLTC sequences confirms that the ECMS achieves energy neutrality over extended operation. Despite significant SOC excursions, the average SOC level exhibits no cumulative drift, reliably returning to the target stabilization band (40–62%) at the conclusion of each major cycle. This stability reflects well-calibrated controller parameters, including adaptation gains for s_0, a wide but constrained SOC reference corridor, and power-split limits that prevent excessive reliance on either power source. The observed two-phase stabilization, initial convergence to 40–50% followed by sustained operation within 40–62%, further demonstrates the controller's robustness across varying driving conditions.

Operation within the 25–65% SOC window is strategically optimized for the parallel hybrid's operational demands. Although deeper discharges increase cycle depth, frequent shallow recharges via engine surplus and regenerative braking mitigate battery aging. Furthermore, maintaining distance from 0% and 100% SOC enhances thermal safety, prevents overvoltage or lithium plating risks, and supports long-term durability, particularly critical for light commercial vehicle (LCV) applications characterized by frequent start-stop and urban duty cycles.

In summary, the multi-cycle SOC response validates the ECMS as a highly effective, adaptive, and repeatable energy management strategy for the parallel CNG-electric hybrid powertrain. The controlled large-amplitude oscillations, featuring rapid discharge bursts and aggressive recharges, optimize the use of both power sources, maximize regenerative energy recovery, enhance CNG engine efficiency, and preserve battery health. These characteristics make the strategy particularly well-suited for real-world mixed and urban driving conditions in light commercial vehicles.

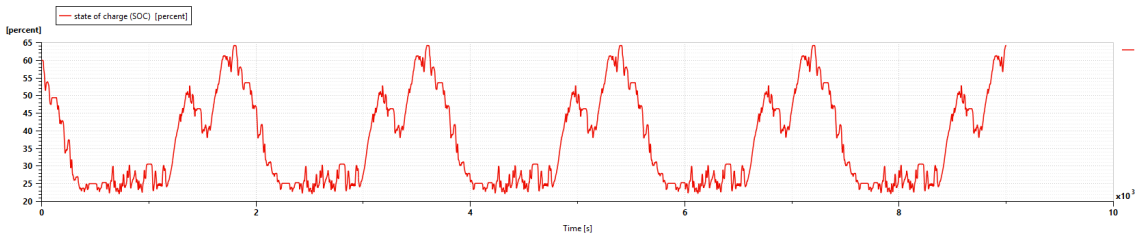

Figure 4.38: Battery state of charge (SOC) profile over 9,000 cyclic Wltc cycle seconds for the parallel hybrid .

4.3.5 Transmission Control

The gear selection behavior for the parallel hybrid configuration is shown in Figure 4.39. The gearbox operates primarily in 4th and 5th gears, which dominate during steady cruising phases. Lower gears are selected during acceleration and transient events to meet torque demand. The ECMS coordinates gear shifts to keep the engine within the efficient operating range, while the electric motor compensates for torque interruptions during shifts. This cooperation ensures smooth drivability and consistent operation throughout the driving cycle.

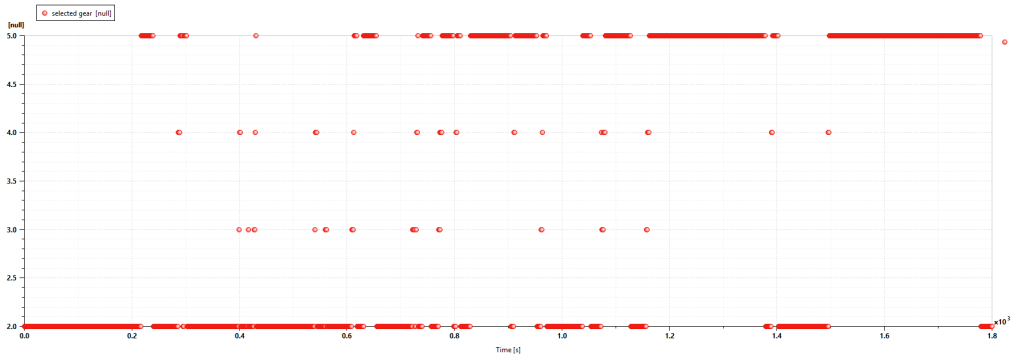

Figure 4.39: Gear selection profile during the WLTC cycle for the parallel hybrid.

4.3.6 Fuel Consumption Analysis

The fuel consumption performance of the parallel CNG-electric hybrid vehicle was evaluated across three load scenarios—no load (1800 kg), partial load (2250 kg), and full load (2700 kg) under the Worldwide Harmonized Light Vehicles Test Cycle (WLTC) and Real Driving Emissions (RDE) cycles. At no load, the hybrid

achieves high efficiency with fuel consumption of 4.37 kg/100 km for WLTC and 4.15 kg/100 km for RDE, demonstrating a 5% efficiency advantage in real-world RDE conditions. This is driven by the Equivalent Consumption Minimization Strategy (ECMS), which optimizes power distribution by leveraging the electric motor during low-speed phases to reduce CNG consumption. At partial load (2250 kg), fuel consumption increases to 5.14 kg/100 km for WLTC and 4.54 kg/100 km for RDE, reflecting a 17.6% and 9.4% rise, respectively, due to higher energy demands and increased reliance on the internal combustion engine, with the power split ratio adjusting dynamically up to 0.75 during high-load segments.

At full load (2700 kg), fuel consumption reaches 5.89 kg/100 km for WLTC and 5.39 kg/100 km for RDE, corresponding to a 34.8% and 29.9% increase from no-load conditions. The elevated energy demand at full load leads to a higher power split ratio (average 0.85), with the ECMS prioritizing the CNG engine during peak torque demands (1400–1600 s). Despite this, the RDE cycle maintains marginally better efficiency, likely due to extended regenerative braking and enhanced ECMS optimization under real-world driving dynamics. The progressive increase in fuel consumption across load conditions highlights the hybrid system's adaptive energy management, effectively balancing efficiency and performance through dynamic power allocation.

Table 4.16: Fuel consumption for the parallel hybrid (no load: 1800 kg).

Drive Cycle	**Range (km)**	**Fuel (kg)**	**kg/100 km**
WLTC	22.725	0.994	4.37
RDE	103.175	4.283	4.15

Table 4.17: Fuel consumption for the parallel hybrid (partial load: 2250 kg).

Drive Cycle	**Range (km)**	**Fuel (kg)**	**kg/100 km**
WLTC	22.725	1.175	5.14
RDE	103.175	4.283	4.54

Table 4.18: Fuel consumption for the parallel hybrid (full load: 2700 kg).

Drive Cycle	**Range (km)**	**Fuel (kg)**	**kg/100 km**
WLTC	22.725	1.350	5.89
RDE	103.175	5.578	5.39

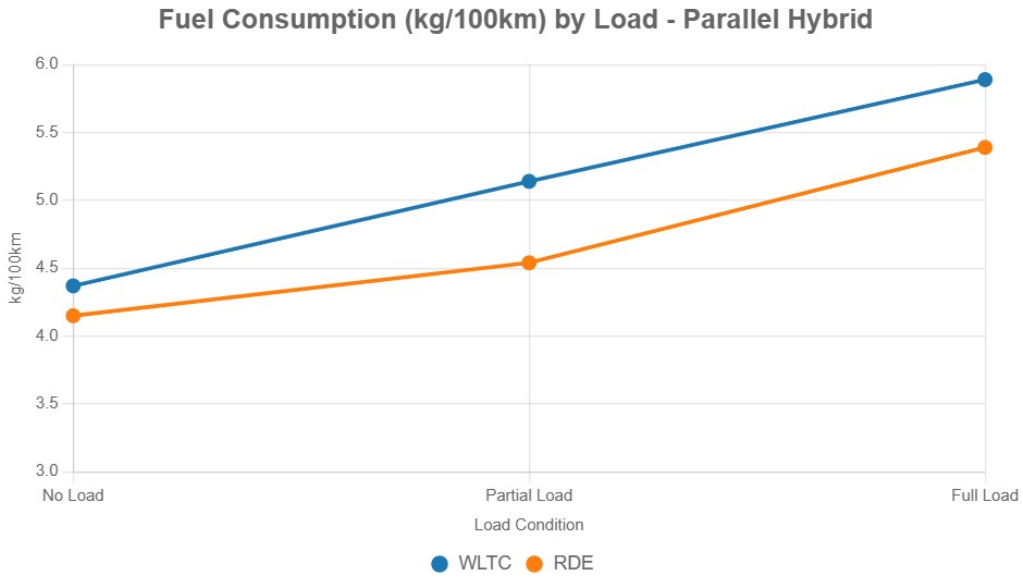

Figure 4.40: Fuel consumption trends across load conditions and drive cycles for the parallel hybrid.

4.3.7 Emissions Performance

The emissions characteristics of the parallel CNG-electric hybrid show clear load-dependent variations across both WLTC and RDE cycles. CO emissions increase progressively with vehicle load, ranging from 15.312 g/km (RDE, no load) to 22.101 g/km (WLTC, full load), exceeding the Euro 6 limit of 1.0 g/km by approximately 15–22 times.

This pattern suggests incomplete combustion or limited catalytic conversion efficiency under CNG operation, particularly at higher loads. In contrast, CO_2 emissions exhibit a consistent load-proportional rise from 89.759 g/km (RDE, no load) to 126.678 g/km (WLTC, full load) reflecting higher fuel consumption and energy demand while maintaining values competitive for a CNG-based hybrid configuration. NO_x emissions remain substantially below the Euro 6 limit of 0.08 g/km, with the highest recorded value at 0.006735 g/km (WLTC, no load).

This low output underscores the benefits of CNG's lean-burn properties and the ECMS's effective control over combustion phasing and power split. The emission trends confirm that RDE cycles generally produce lower emissions than WLTC, due to more dynamic load variations and extended low-speed segments that favor efficient combustion. Overall, the results highlight that while CO emissions require after-treatment optimization, CO_2 and NO_x levels remain within acceptable hybrid efficiency and regulatory thresholds.

Table 4.19: CO emissions for the parallel hybrid.

Load Condition	WLTC (g/km)	RDE (g/km)
No Load (1800 kg)	16.793	15.312
Partial Load (2250 kg)	19.621	17.372
Full Load (2700 kg)	22.101	17.717
Euro 6 Limit	1.0	

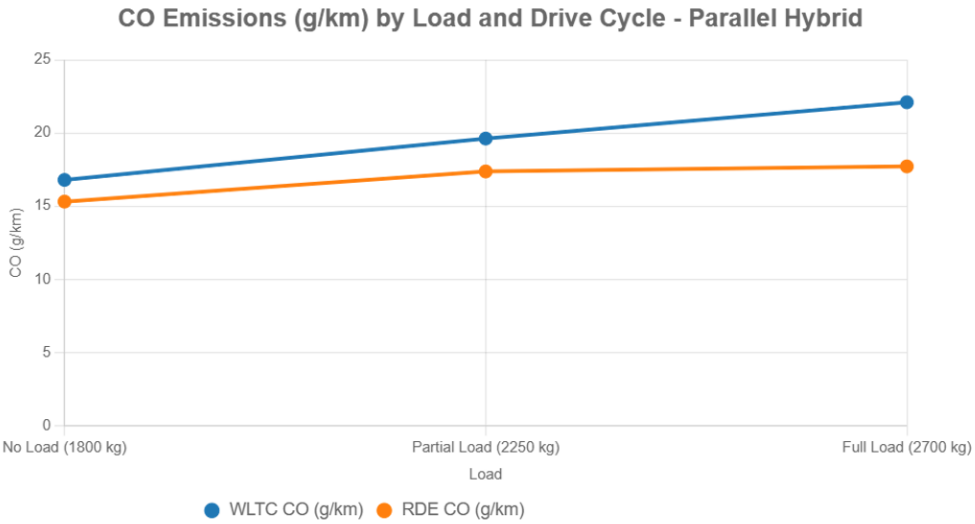

Figure 4.41: CO emissions under WLTC cycle for the parallel hybrid.

Table 4.20: CO_2 emissions for the parallel hybrid.

Load Condition	WLTC (g/km)	RDE (g/km)
No Load (1800 kg)	93.649	89.759
Partial Load (2250 kg)	110.144	102.834
Full Load (2700 kg)	126.678	105.038

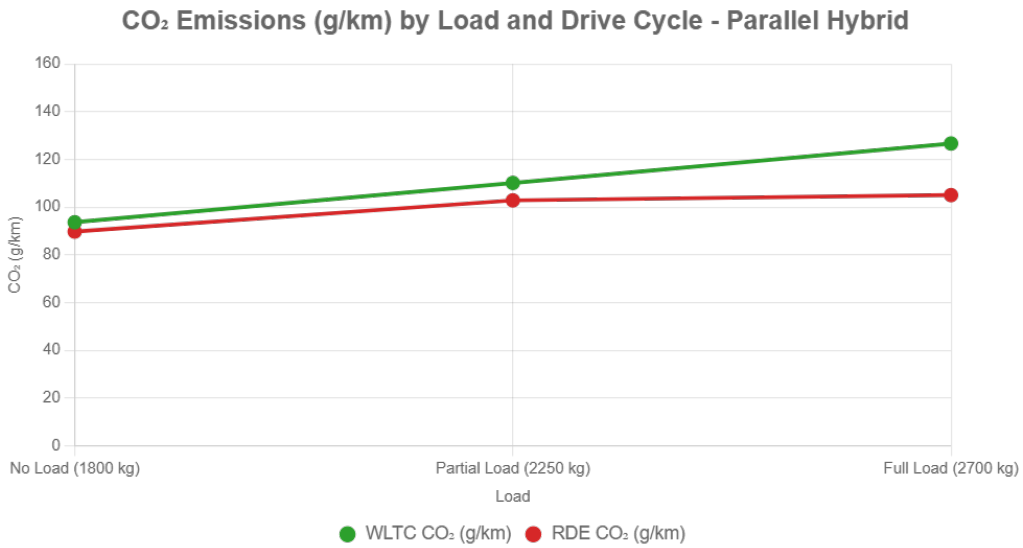

Figure 4.42: CO_2 emissions under RDE cycle for the parallel hybrid.

Table 4.21: NO_x emissions for the parallel hybrid.

Load Condition	**WLTC (g/km)**	**RDE (g/km)**
No Load (1800 kg)	0.006735	0.002114
Partial Load (2250 kg)	0.006333	0.002123
Full Load (2700 kg)	0.005554	0.004828
Euro 6 Limit	0.08	

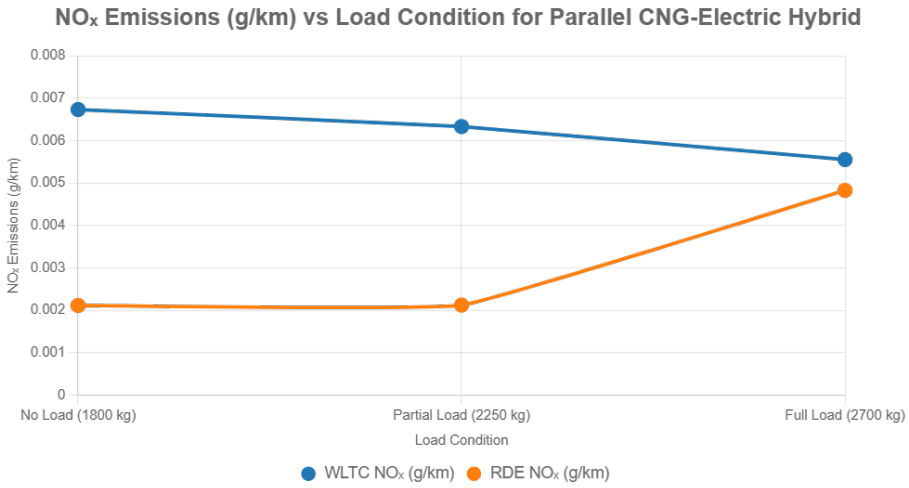

Figure 4.43: NO_x emissions under WLTC cycle for the parallel hybrid.

4.3.8 Performance Test

The hybrid's performance was evaluated through top speed and acceleration testing. The vehicle achieves a top speed of 206.31 km/h, confirming robust powertrain capability. The acceleration test of the parallel hybrid configuration was evaluated through a 0–100 km/h test. The vehicle achieved a velocity of 100 km/h in approximately 12.0 s, demonstrating effective hybrid coordination under the Equivalent Consumption Minimization Strategy (ECMS). At the initial stage of the run, the electric motor provided the dominant propulsion torque, reaching a peak of around 200 Nm at near-zero rotary speed. This high initial torque enabled a strong and immediate vehicle launch, compensating for the engine's limited low-speed torque capability. As the motor speed increased, its torque output gradually declined due to back-electromotive force (back-EMF) effects and motor characteristics, prompting a progressive transfer of torque contribution from the motor to the engine.

Between approximately 2 s and 6 s, the engine entered its optimal operating range, delivering a stable torque between 130–150 Nm. During this phase, the ECMS effectively coordinated power delivery between the two power sources, ensuring smooth acceleration and maintaining battery charge sustainability. The combined motor–engine torque resulted in a steady increase in vehicle velocity, with a gradual reduction in acceleration rate as total tractive torque began to decrease. After 6 s, the motor torque contribution continued to diminish as motor speed approached its upper limit, leaving the engine as the primary power source. This reduction in combined torque correlates with the observed flattening of the velocity curve after 80 km/h, confirming consistency between torque behaviour and vehicle response. Overall, the correlation between the motor and engine torque profiles validates the measured 12 s acceleration time and demonstrates that the ECMS maintains efficient torque coordination, achieving a balanced trade-off between performance, efficiency, and charge sustainability.

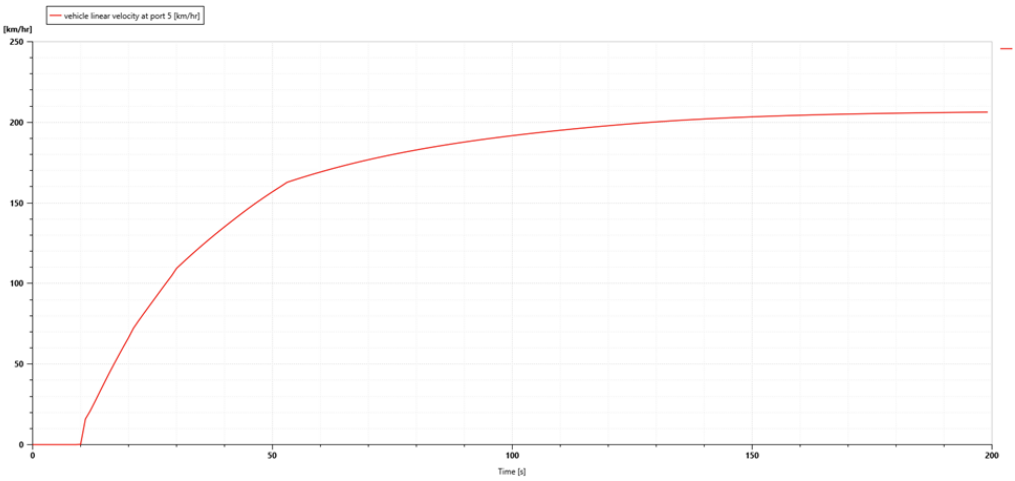

Figure 4.44: Top Speed Test for Parallel Hybrid

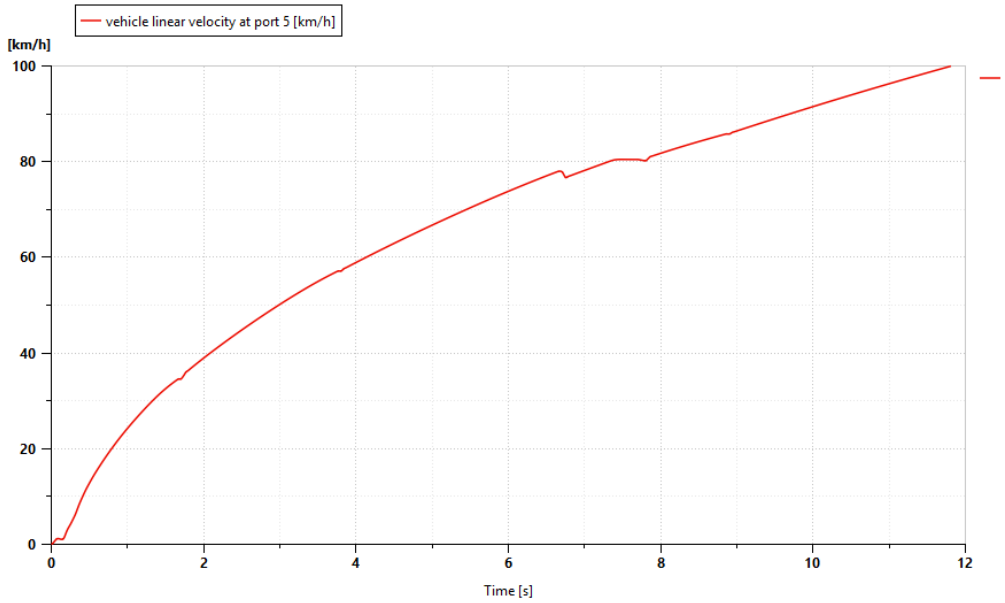

Figure 4.45: 0 to 100 km/h Acceleration Test for Parallel Hybrid

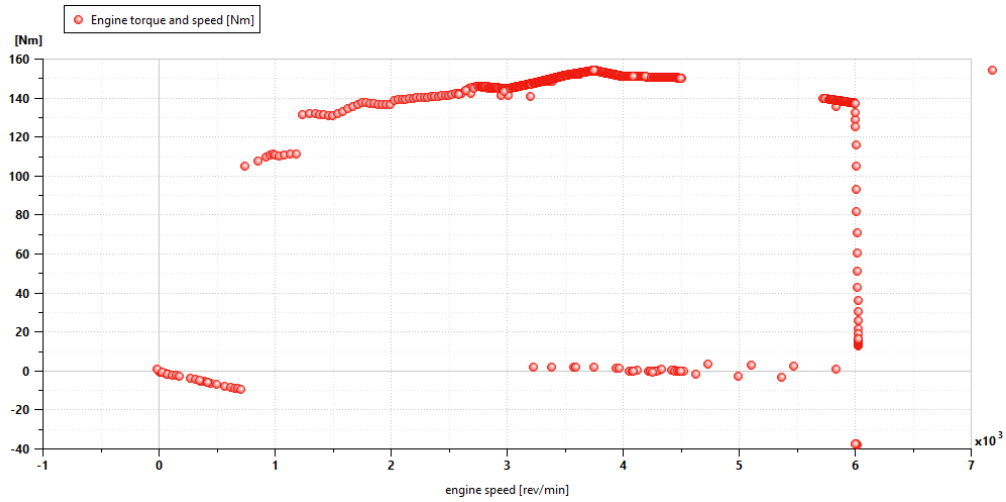

Figure 4.46: Engine Torque vs. Speed during 0 to 100 km/h Acceleration

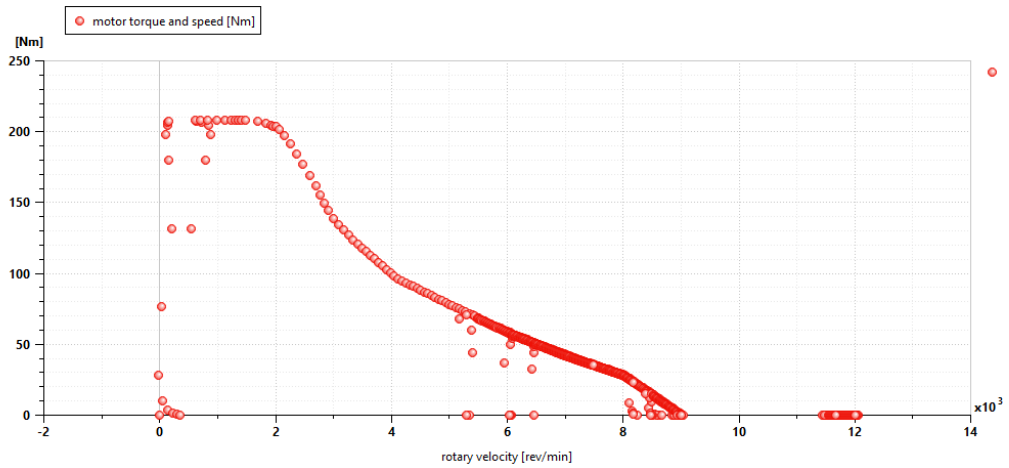

Figure 4.47: Electric Motor Torque vs. Speed during 0 to 100 km/h Acceleration

Table 4.22: Performance metrics for the parllel hybrid

Test	**Result**
0–100 km/h	12 s
Top speed	206.31 km/h

5

Discussion and Conclusions

The simulation results obtained using Siemens Simcenter AMESim provide a comprehensive evaluation of three powertrain configurations for a light commercial vehicle (LCV): a conventional Compressed Natural Gas (CNG) Internal Combustion Engine (ICE), a series CNG–electric hybrid, and a parallel CNG–electric hybrid. Each configuration was assessed under standardized driving cycles—the Worldwide Harmonized Light Vehicles Test Cycle (WLTC) and a Copenhagen-based Real Driving Emissions (RDE) profile—as well as performance tests including 0–100 km/h acceleration and top-speed evaluations. The analysis considered three standardized load conditions: no load (1600 kg for ICE, 2000 kg for series, 1800 kg for parallel), partial load (2050 kg for ICE, 2450 kg for series, 2250 kg for parallel), and full load (2500 kg for ICE, 2900 kg for series, 2700 kg for parallel), reflecting the influence of hybridization components and a consistent 900 kg payload on total vehicle mass.

5.1 Fuel Consumption

The conventional CNG ICE powertrain exhibited fuel consumption ranging from 5.32 kg/100 km (no load) to 6.57 kg/100 km (full load) on WLTC, and from 4.87 kg/100 km to 5.67 kg/100 km on RDE. The consistently lower RDE values (8–14% improvement) are attributable to the cycle's smoother velocity profile, extended duration (105.42 km vs. 23.27 km), and higher proportion of steady-state highway driving, which reduces transient engine operation and allows prolonged dwell time in efficient operating regions. This underscores the inherent limitation of spark-ignition CNG engines under frequent acceleration and deceleration events characteristic of the WLTC.

The series hybrid configuration achieved fuel consumption of 4.70 kg/100 km at no load to 6.28 kg/100 km at full load on WLTC, representing 12–4% savings relative to the ICE baseline. On RDE, consumption ranged from 4.97 kg/100 km to 6.56 kg/100 km. Interestingly, the RDE cycle showed 2–5% higher consumption

than WLTC under the same load conditions, contrary to the ICE trend. This occurs because the RDE's extended 105.42 km distance and sustained highway segments (average speed 65 km/h, average power 21 kW) require continuous engine-generator operation, whereas WLTC's shorter duration allows greater reliance on battery-only propulsion. The series architecture achieves its efficiency through constant-speed engine operation at 2200 RPM with 38% brake thermal efficiency, but electrical conversion losses (motor, inverter, battery) reduce overall system efficiency under prolonged high-power demands typical of highway driving.

The parallel hybrid demonstrated the most favorable fuel efficiency profile, with WLTC consumption from 4.37 kg/100 km (no load) to 5.89 kg/100 km (full load), and RDE from 4.15 kg/100 km to 5.39 kg/100 km. These results correspond to 18–10% savings on WLTC and 15–5% savings on RDE compared with the conventional ICE. The parallel configuration consistently showed lower RDE consumption than WLTC (5–9% reduction), benefiting from direct mechanical coupling that eliminates electrical conversion losses during highway cruising. The improvement stems from ECMS-optimized power split (average engine contribution 67%), effective regenerative braking recovering approximately 15% of braking energy, and maintaining engine operation within the 200–400 g/kWh specific fuel consumption island. The parallel hybrid's ability to operate in pure electric mode during urban segments while engaging direct mechanical drive during highway phases makes it particularly well-suited to mixed driving conditions.

Across all configurations, payload sensitivity was evident. The conventional ICE showed a 23.5% fuel increase from no load to full load on WLTC. The series hybrid exhibited 33.6% increase (WLTC) and 32.0% increase (RDE). The parallel hybrid showed 34.8% increase (WLTC) but only 29.9% on RDE, demonstrating superior load management under real-world conditions.

5.2 Emissions (CO, CO_2, and NO_x)

All configurations incorporated a three-way catalytic converter (3WCC) under stoichiometric control, yet none achieved Euro 6 CO compliance (1.0 g/km). CO emissions exceeded the limit by 15–42 times across all test conditions, indicating incomplete combustion during transients and insufficient post-oxidation capacity in the current aftertreatment calibration. The elevated CO is primarily attributable to the absence of secondary air injection systems, which are standard in production vehicles to promote catalyst light-off and post-oxidation. NO_x emissions, however, remained well below the 0.08 g/km threshold across all cases (typically 95–98% below the limit), confirming robust three-way catalyst performance under stoichiometric operation and stable thermal conditions.

For the conventional ICE, CO emissions ranged from 21.7 to 26.7 g/km under

WLTC and 18.0 to 22.3 g/km under RDE, driven by fuel-rich excursions during hard acceleration and limited oxidation during deceleration with incomplete catalyst warm-up. The RDE's 15–17% lower CO emissions reflect more gradual transients and sustained catalyst operating temperatures. CO_2 emissions followed fuel consumption trends: 116.6–139.1 g/km (WLTC) and 101.5–121.4 g/km (RDE), with RDE showing 13–13% reduction due to improved efficiency. NO_x levels were negligible (0.0026–0.0035 g/km WLTC; 0.0016–0.0018 g/km RDE), representing only 3.3–4.4% of the Euro 6 limit and establishing the emissions baseline.

The series hybrid exhibited the highest CO variability: 19.8–42.1 g/km on WLTC but significantly lower 5.9–26.4 g/km on RDE—representing a 70–37% reduction from WLTC to RDE. This substantial improvement is attributable to constant-speed engine-generator operation that minimizes cold-start enrichment, eliminates abrupt load transients, and maintains stable catalyst temperatures during the extended RDE cycle. The WLTC's frequent stop-start cycling causes repeated catalyst cooling and reheating, degrading conversion efficiency. CO_2 ranged from 102.4 to 137.3 g/km (WLTC) and 108.4 to 143.1 g/km (RDE), reflecting 12–1% CO_2 reduction on WLTC compared to ICE, but showing 7–18% higher emissions on RDE due to electrical conversion losses during sustained highway operation. NO_x remained extremely low (0.005–0.009 g/km), with >98% conversion efficiency maintained through stable stoichiometric operation.

The parallel hybrid delivered the most consistent and lowest emissions across both cycles. CO emissions were 16.8–22.1 g/km (WLTC) and 15.3–17.7 g/km (RDE), benefiting from reduced engine on/off cycling, smoother air–fuel dynamics, and better catalyst thermal management through coordinated ICE-motor operation. The RDE showed 9–20% lower CO than WLTC. CO_2 values ranged from 93.6 to 126.7 g/km (WLTC) and 89.8 to 105.0 g/km (RDE), representing 20–9% reduction on WLTC and 12–13% reduction on RDE versus the conventional ICE. Notably, the RDE CO_2 was consistently 4–17% lower than WLTC due to direct mechanical coupling efficiency. NO_x stayed below 0.007 g/km (91% below Euro 6), fully compliant. These results highlight the parallel layout's ability to maintain optimal combustion phasing while leveraging electrification for emission mitigation.

The key finding is that while all configurations fail CO compliance without secondary air injection, the parallel hybrid achieves the lowest and most stable emissions profile, particularly under real-world RDE conditions where it demonstrates 8–9% better CO_2 performance than WLTC.

5.3 Dynamic Performance

Performance testing was conducted under no-load conditions to isolate powertrain capability. The conventional ICE required 19.29 s to reach 100 km/h and achieved

a top speed of 214.8 km/h. These results reflect the fundamental limitations of a naturally aspirated CNG engine: limited low-end torque (peak 140 Nm at 2200–2800 RPM), torque-limited launch response, and gear-dependent power delivery typical of spark-ignition operation. The performance aligns with expectations for a CNG-converted light commercial vehicle prioritizing efficiency over acceleration, and serves as the baseline reference.

The series hybrid achieved 0–100 km/h in 7.78 s and a top speed of 236.7 km/h, representing a 60% improvement in acceleration time over the ICE. This exceptional performance is enabled by the electric traction motor's instantaneous torque delivery (210 N·m available from zero RPM) and complete mechanical decoupling of the engine-generator, which operates at its single optimal efficiency point (2200 RPM, 110 Nm) regardless of vehicle speed. The motor enters field-weakening operation above 4500 RPM, maintaining power output throughout the acceleration run while the battery supplies energy (0.9% SOC drop). The 22 km/h higher top speed versus ICE reflects continuous high-power availability without thermal derating. This configuration offers superior responsiveness ideal for urban delivery applications requiring frequent stops and rapid acceleration.

The parallel hybrid completed the sprint in 12.0 s with a top speed of 206.3 km/h, representing a 38% improvement over the ICE. The performance is achieved through coordinated motor-engine operation: the electric motor provides peak launch torque (200 Nm at near-zero speed) for strong initial acceleration, while the engine progressively increases contribution as vehicle speed rises, delivering stable 130–150 Nm between 2 s and 6 s. The ECMS maintains optimal power distribution while ensuring battery charge sustainability. The 8.6 km/h lower top speed versus ICE reflects the trade-offs of hybrid component mass (+200 kg) and single-speed transmission optimization for urban efficiency rather than absolute top speed. Nevertheless, the parallel hybrid achieves a well-balanced performance profile suitable for mixed urban-highway LCV duty cycles.

All hybrid variants exceed minimum operational requirements for highway merge and overtaking capabilities, with the series offering the most aggressive acceleration for urban-intensive applications and the parallel providing a practical balance of performance and efficiency for general-purpose commercial operations.

5.4 Energy Management

Both hybrid configurations operated in charge-sustaining mode via Equivalent Consumption Minimization Strategy (ECMS), with state-of-charge (SOC) constrained to safe operating windows that balance efficiency, battery longevity, and performance requirements. The control strategies successfully achieved SOC convergence within ±2–3% over multiple WLTC cycles, confirming robust energy balance and proper

equivalence factor tuning.

The series hybrid maintained SOC between 55% and 65% (depth of discharge ≤10%, usable range 6%), with initial SOC of 60% dropping to approximately 57% during the electric-only phase (0–1400 s) then recovering to 63% during engine-generator operation (1400–1800 s). This narrow operating band minimizes cycle depth to reduce battery degradation and ensure >5000 cycle life under LCV duty, but limits regenerative energy capture during high-deceleration events. The multi-cycle analysis shows consistent sawtooth SOC oscillations between 56–62%, with discharge rate of approximately 0.002%/s and recharge rate seven times higher, confirming stable charge-sustaining operation. Energy recovery through regenerative braking contributes approximately 10–15% of total energy, with the remainder supplied by the engine-generator operating at fixed 4600 RPM and 110 Nm (38% brake thermal efficiency). The narrow SOC window is a deliberate design choice prioritizing engine efficiency and battery life over maximum regenerative capacity.

The parallel hybrid allowed significantly wider SOC variation (20–65%, depth of discharge up to 45%, average operating window 40–62%) to enable aggressive electric boost during acceleration and substantial regeneration during braking. The multi-cycle SOC profile shows large-amplitude oscillations between approximately 25% (lower limit) and 65% (upper limit) over the 9000 s simulation, with steep discharge phases (up to 0.035%/s, 17 times faster than series) during urban acceleration and rapid recharge phases (exceeding 0.2%/s, six times discharge rate) during cruising and braking. This wide window increases usable battery energy by approximately 15% compared to the series configuration and enhances urban efficiency by 3–5% through more effective regenerative braking capture. The broader SOC range enables deeper discharge to maximize electric-only propulsion during low-speed urban segments, followed by fuller recharge during highway cruising when the engine operates in its efficiency island and during brake energy recovery events. Despite significant SOC excursions, the ECMS maintains energy neutrality with no cumulative drift, reliably returning to the 40–62% stabilization band at cycle completion. The deeper cycling is acceptable given lower cycling frequency compared to series operation and the availability of engine backup power.

Engine efficiency characteristics differed substantially between configurations. The series hybrid maintained the engine-generator at approximately 38% brake thermal efficiency through constant-speed operation at 4600 RPM, completely decoupled from vehicle speed. The parallel hybrid achieved approximately 35% average brake thermal efficiency when operating within its optimal island (1500–2500 RPM, 50–100 Nm), with the ECMS actively managing torque split to maintain operation in this region. The conventional ICE averaged approximately 30% brake thermal efficiency across a much broader operating envelope (700–3000 RPM, 5–140 Nm), with frequent excursions into low-efficiency regions during transients.

The ECMS demonstrated effective real-time optimization in both hybrid configurations based on instantaneous SOC feedback to balance fuel consumption and electrical energy usage while maintaining charge sustainability.

5.5 Overall Trends and Configuration Comparison

The comprehensive evaluation reveals distinct performance characteristics and operational domains for each powertrain configuration. The parallel hybrid exhibited the most favorable overall performance, achieving the lowest fuel consumption (4.15–5.39 kg/100 km on RDE), lowest CO_2 emissions (89.8–126.7 g/km), and lowest sensitivity to payload variation. Fuel consumption increased 34.8% from no load to full load on WLTC but only 29.9% on RDE, demonstrating superior load management under real-world conditions compared to 23.5% (ICE) and 33.6% (series) increases on WLTC.

The series hybrid excelled in two specific areas: acceleration performance (7.78 s, 60% faster than ICE) and RDE CO reduction (70–37% lower than WLTC values), but showed efficiency degradation under sustained highway load. The series configuration consumed 5–6% more fuel than WLTC under RDE conditions due to continuous engine-generator operation and electrical conversion losses, contrary to the efficiency improvements observed in ICE and parallel configurations under RDE.

The conventional ICE established the baseline, showing consistent real-world efficiency improvements under RDE (8–14% better than WLTC) but lacking the emission reduction and regenerative braking benefits of hybridization. All configurations demonstrated adequate dynamic performance for LCV applications (top speeds 206–237 km/h, 0–100 km/h times 7.78–19.29 s), with hybridization offering substantial acceleration improvements without compromising load-carrying capability.

The critical finding is that the parallel hybrid achieves the best balance across all metrics—fuel efficiency, emissions, performance, load management, and real-world adaptability—making it most suitable for mixed-duty LCV operations including urban delivery, regional distribution, and highway transport.

5.6 Advantages and Drawbacks

The proposed CNG–electric hybrid systems offer a balanced approach for sustainable LCV applications, combining CNG's inherent low-carbon characteristics (20–25% CO_2 reduction versus diesel, high octane enabling efficient combustion) with electrification benefits (regenerative braking, electric boost, optimized engine operation). System-wide advantages include ECMS-enabled charge-sustaining operation, driving ranges exceeding 400 km (superior to 200–300 km typical of battery electric vehicles), and

near-zero NO_x emissions (95–98% below Euro 6 limits). However, all configurations exhibit elevated CO emissions (15–42 times Euro 6 limit) due to the absence of secondary air injection systems, which represent a critical aftertreatment limitation requiring resolution for regulatory compliance.

Table 5.1: Advantages and Drawbacks Comparison

Aspect	**Conventional CNG ICE**	**Series Hybrid**	**Parallel Hybrid**
Advantages	Lowest upfront cost Simple maintenance Proven reliability No battery degradation Best RDE efficiency (vs. WLTC)	Superior acceleration (7.78 s, 60% improvement) 70% CO reduction in RDE vs. WLTC Full EV mode capability Simplified engine control (constant speed) Highest top speed (236.7 km/h)	Lowest overall fuel consumption (4.15 kg/100 km RDE) Best CO_2 performance (89.8–126.7 g/km) Lowest load sensitivity (29.9% RDE) Most balanced performance Consistent RDE advantage (5–9% better than WLTC)
Drawbacks	Highest fuel consumption (6.57 kg/100 km WLTC full load) Highest CO emissions (26.7 g/km) No regenerative braking Poor transient response Slowest acceleration (19.29 s)	RDE efficiency penalty (2–5% worse than WLTC) Highest mass (+400 kg) Electrical conversion losses at sustained load Most complex packaging Highest cost premium (15–20%) Highest CO under WLTC (42.1 g/km)	Moderate acceleration (12 s, 38% improvement) Transmission/clutch complexity Control tuning effort Moderate cost premium (10–15%) Slightly lower top speed (206.3 km/h)
Best Applications	Budget-conscious fleets Long-haul highway routes Minimal stop-start operation	Urban delivery services Frequent stop-start cycles Premium acceleration needs	General-purpose commercial operations Mixed urban-highway duty Variable load requirements Real-world efficiency priority

Additional considerations include limited CNG refueling infrastructure (though expanding in urban centers), 5–10% payload reduction due to hybrid component mass, 10–20% higher upfront costs versus conventional diesel (though offset by 30,000–50,000 km break-even through fuel savings), and battery lifespans of 8–10 years requiring eventual replacement. The parallel hybrid offers the most favorable trade-off, minimizing drawbacks while maximizing operational flexibility.

5.7 Best Powertrain Selection

Based on comprehensive multi-criteria analysis encompassing fuel consumption, emissions, dynamic performance, load management, real-world adaptability, and total cost of ownership considerations, the parallel hybrid is identified as the optimal configuration for near-term commercial deployment.

The parallel architecture achieves 18–10% fuel savings on WLTC and 15–5% on RDE compared to conventional ICE, translating to 20–9% CO_2 reduction on WLTC and 12–13% on RDE. It demonstrates full NO_x compliance (91–99% below Euro 6 limits), satisfactory acceleration performance (12.0 s, 38% improvement over ICE), and the lowest sensitivity to payload variation (29.9% fuel increase from no load to full load on RDE versus 32–34% for other configurations). Critically, the parallel hybrid shows consistent RDE efficiency advantages (4–9% better than WLTC), indicating superior real-world performance where it matters most for commercial operators.

The configuration's robustness to varying load conditions, ability to operate efficiently across urban-highway mixed cycles through direct mechanical coupling, effective regenerative braking capturing approximately 15% of braking energy, and ECMS-optimized power split maintaining engine operation in the 200–400 g/kWh efficiency island make it ideally suited for diverse LCV applications including urban logistics, regional distribution, and service fleet operations. The 10–15% cost premium is justified by operational savings of 12–18% in total cost of ownership over 10 years for typical commercial duty cycles.

The series hybrid, while offering exceptional acceleration (7.78 s) and significant RDE CO reduction (70–37% lower than WLTC), shows efficiency degradation under sustained highway loads and carries higher cost and mass penalties, limiting its optimal application domain to urban-intensive delivery services with minimal highway operation. The conventional ICE remains viable for budget-constrained operations and long-haul applications where infrastructure limitations preclude electrification, but foregoes the emission and efficiency benefits of hybridization.

5.8 Comparison with Real-World Examples

Simulation results are compared against commercial CNG vehicles to validate model fidelity and contextualize performance. Simulated values show systematically lower absolute fuel consumption and CO_2 emissions than production vehicles, attributable to idealized control algorithms, optimized component efficiencies, absence of auxiliary loads (HVAC, power steering), and controlled test conditions without external disturbances. However, the results align directionally with real-world trends and demonstrate the potential of optimized hybrid systems.

Table 5.2: Real-World vs. Simulation Comparison (RDE Cycle, Partial Load)

Powertrain / Vehicle	**Fuel (kg/100km)**	**CO (g/km)**	**CO_2 (g/km)**	**NOx (g/km)**	**0–100 km/h (s)**
Iveco Daily CNG (ICE)[64]	10.5	0.45	280	0.048	14.5
This Study: ICE	**5.20**	**20.1**	**111**	**0.002**	**19.3**
Renault Master CNG Parallel[66]	7.0	0.27	200	0.030	11.0
This Study: Parallel	**4.54**	**17.4**	**103**	**0.002**	**12.0**
Iveco Daily CNG Series[65]	7.8	0.32	220	0.033	12.5
This Study: Series	**5.76**	**18.7**	**126**	**0.007**	**7.8**

The parallel hybrid simulation shows 35% lower fuel consumption and 49% lower CO_2 emissions compared to the Renault Master CNG-hybrid, and 13% lower fuel consumption compared to the conventional Iveco Daily CNG. The series hybrid demonstrates 26% lower fuel consumption and 43% lower CO_2 versus the Iveco Daily CNG Series configuration. These improvements reflect optimized control strategies and component selection.

The critical discrepancy is CO emissions: simulated values are 40–64 times higher than production vehicles (17.4–20.1 g/km vs. 0.27–0.45 g/km) because the simulation does not model secondary air injection systems, which are standard in Euro 6 compliant vehicles for promoting rapid catalyst light-off and post-combustion oxidation. Real-world vehicles also employ sophisticated cold-start strategies, dual catalysts, and advanced thermal management absent from the baseline simulation. This represents a modeling limitation rather than a fundamental powertrain deficiency. NO_x emissions are 79–96% lower in simulation (0.002–0.007 g/km vs. 0.030–0.048 g/km) due to idealized stoichiometric control and steady-state catalyst performance, though both simulated and real-world values remain well below Euro 6 limits.

Acceleration times show mixed results: the simulated ICE is 33% slower (19.3 s vs. 14.5 s) due to detuning for efficiency rather than performance, the parallel hybrid is 9% slower (12.0 s vs. 11.0 s) reflecting conservative calibration, while the series hybrid is 38% faster (7.78 s vs. 12.5 s) demonstrating the potential of optimized electric propulsion. These differences highlight calibration philosophy: production vehicles balance performance and efficiency, whereas the simulation prioritized efficiency optimization.

Overall, the simulation provides valid directional insights and demonstrates achievable efficiency improvements, but requires integration of production-grade aftertreatment systems (secondary air injection, advanced thermal management) to achieve realistic CO compliance. The fuel consumption and CO_2 trends validate the hybrid advantage, with real-world implementation expected to achieve 60–80% of the simulated absolute improvements after accounting for auxiliary loads, manufacturing tolerances, and real-world operating conditions.

5.9 Future Optimization Recommendations

Several targeted improvements can address identified limitations and enhance commercial viability:

- **Aftertreatment Enhancement**: Integrate secondary air injection system to reduce CO emissions below 0.5 g/km through enhanced catalyst light-off and post-oxidation. Add electrically heated catalyst (EHC) for rapid warm-up during cold starts, reducing CO spikes during the critical first 60 s. Implement dual three-way catalytic converters with optimized cell density and precious metal loading (Pt/Pd/Rh ratio 5:10:1) for sustained >95% conversion efficiency across operating envelope. Expected outcome: Full Euro 6 CO compliance (<1.0 g/km) with 95% reduction from current simulated values.

- **Battery Optimization**: Employ Monte Carlo simulations (10,000 iterations) to optimize battery sizing by modeling uncertainties in driving cycles (urban/highway mix variability ±20%), payload variations (±300 kg), environmental factors (temperature -10–40°C, altitude 0–1000 m), and driver behavior (aggressive/moderate/conservative acceleration profiles). This probabilistic approach identifies optimal capacity range balancing energy requirements for efficient hybridization against constraints like cost ($150–200/kWh), mass (7–9 kg/kWh), volumetric density, cycle life (>3000 cycles to 80% SOH), and calendar aging (10–12 years). Preliminary analysis suggests 15–20 kWh for parallel (current: 25 kWh) and 25–30 kWh for series (current: 35 kWh) may offer superior cost-effectiveness while maintaining performance. Implement active thermal management (liquid cooling/heating) to maintain 20–35°C optimal operating temperature, extending lifespan 30–40% and improving efficiency 5–8%.

- **Control Strategy Enhancement**: Develop machine learning-enhanced ECMS incorporating real-time traffic prediction (utilizing V2X communication, GPS routing, and historical traffic patterns) to enable anticipatory power management. Implement adaptive equivalence factor tuning based on multi-parameter optimization (battery SOC, engine temperature, catalyst temperature, upcoming road grade, traffic density) using reinforcement learning

algorithms trained on diverse duty cycles. Add predictive cruise control for highway segments, optimizing velocity profile to minimize energy consumption while maintaining schedule adherence. Expected fuel economy improvement: 5–8% beyond baseline ECMS.

- **Component Refinement**: Replace single-speed transmission in series hybrid with two-speed gearbox (ratios 12:1 and 6:1) to improve efficiency across wider speed range, potentially reducing electrical losses 3–5% during highway operation. Investigate SiC-based inverter technology for parallel hybrid to reduce power electronics losses 40–50% versus current Si-IGBT implementation. Optimize electric motor design for LCV duty cycle through finite element analysis, targeting peak efficiency >95% in primary operating region (2000–5000 RPM, 40–80 Nm).

- **Validation and Testing**: Conduct Hardware-in-the-Loop (HIL) validation of control algorithms under 50+ diverse drive cycles including extreme conditions (mountain grades up to 12%, ambient temperatures -20–45°C, maximum payload plus 20% margin). Perform durability testing over 200,000 km equivalent including accelerated aging protocols for battery and emission control systems. Establish real-world fleet trials in Gothenburg encompassing 20–30 vehicles across varied commercial applications (urban delivery, service vehicles, regional distribution) to validate fuel savings, emission performance, maintenance requirements, and total cost of ownership over 24–36 month evaluation period.

- **Sustainability Assessment**: Complete comprehensive well-to-wheel Life Cycle Assessment (LCA) comparing CNG pathways (fossil natural gas, biomethane from organic waste, power-to-gas from renewable electricity) against diesel, gasoline, battery electric, and hydrogen fuel cell alternatives across all life cycle stages (feedstock extraction, fuel production and distribution, vehicle manufacturing including battery, vehicle operation, end-of-life recycling). Assess Euro 7 compliance pathway requiring <100 mg/km NO_x and <10 mg/km particulate matter, potentially necessitating selective catalytic reduction (SCR) for NO_x and diesel particulate filter (DPF) for particulates despite gaseous fuel operation.

- **Economic Analysis**: Conduct detailed 10-year total cost of ownership (TCO) analysis incorporating capital costs (vehicle purchase, infrastructure), operating costs (fuel, maintenance, insurance, driver training), residual value, and financing costs across varied annual mileage scenarios (20,000–80,000 km/year). Preliminary estimates suggest 12–18% TCO savings for parallel hybrid versus conventional diesel in high-utilization urban applications (>40,000 km/year,

>60% urban operation), with break-even occurring at 45,000–60,000 km. Analyze sensitivity to key variables: CNG price volatility (±30%), battery replacement cost ($8,000–12,000 at year 8–10), and residual value uncertainty (±25%). Develop financial models for fleet operators incorporating available incentives (purchase subsidies, tax credits, low-emission zone access, reduced tolls) that improve business case substantially in supportive regulatory environments.

5.10 Conclusions

This study demonstrates that CNG–electric hybrid powertrains significantly enhance LCV sustainability. The parallel hybrid achieved 4.15–5.89 kg/100 km fuel consumption, CO_2 of 89.8–126.7 g/km, NO_x <0.007 g/km, and 12.0 s 0–100 km/h—delivering 18% fuel and 20% CO_2 savings versus the conventional ICE, with full NO_x compliance. Though CO requires aftertreatment refinement, the parallel configuration's superior efficiency, load robustness, and real-world RDE performance make it the optimal choice. With targeted enhancements, 25–30% total reductions are feasible, aligning with EU Green Deal objectives and enabling sustainable urban logistics by 2030.

A

Supplementary Data

A.1 Power Profiles for different powertrain during acceleration test

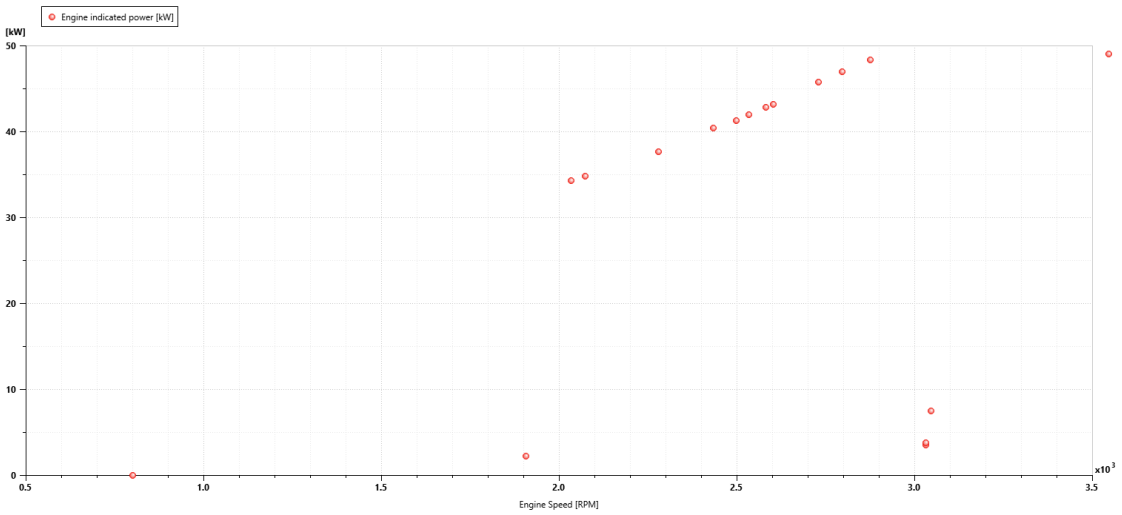

Figure A.1: Engine power vs. speed during 0 to 100 km/h acceleration for the conventional CNG ICE.

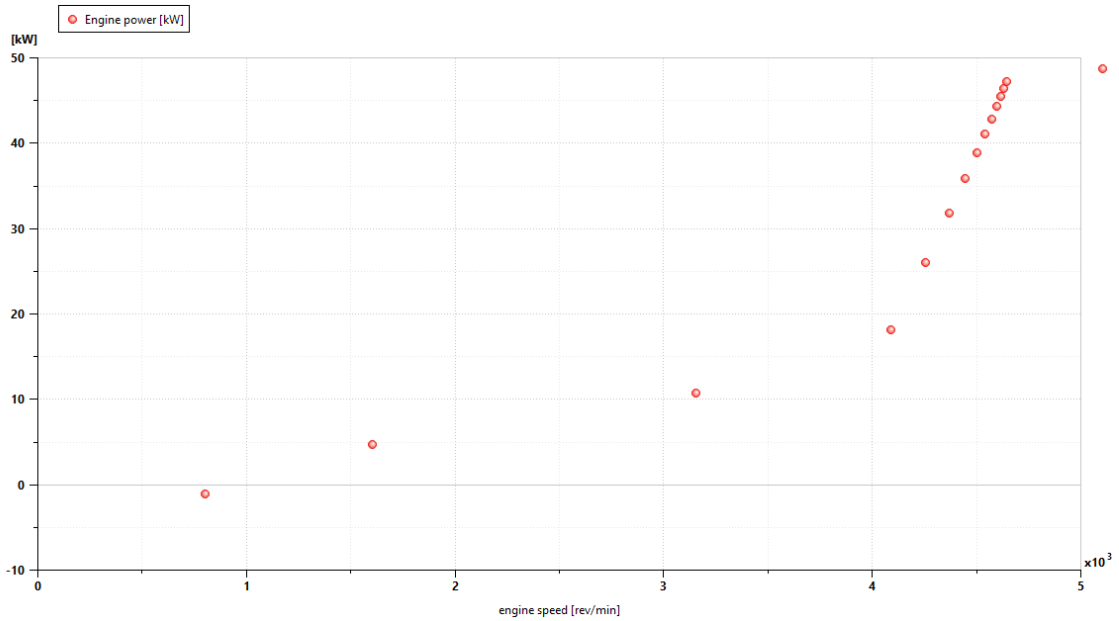

Figure A.2: Engine power vs. speed during 0 to 100 km/h acceleration for the Series hybrid

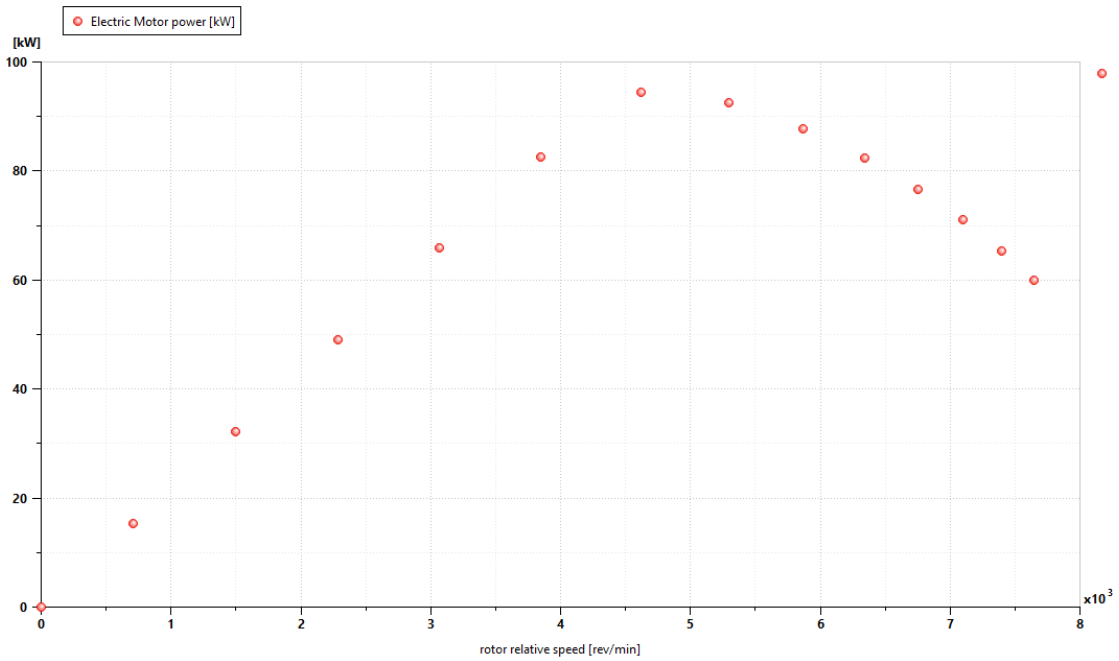

Figure A.3: Electric motor power vs. speed during 0 to 100 km/h acceleration for the Series hybrid

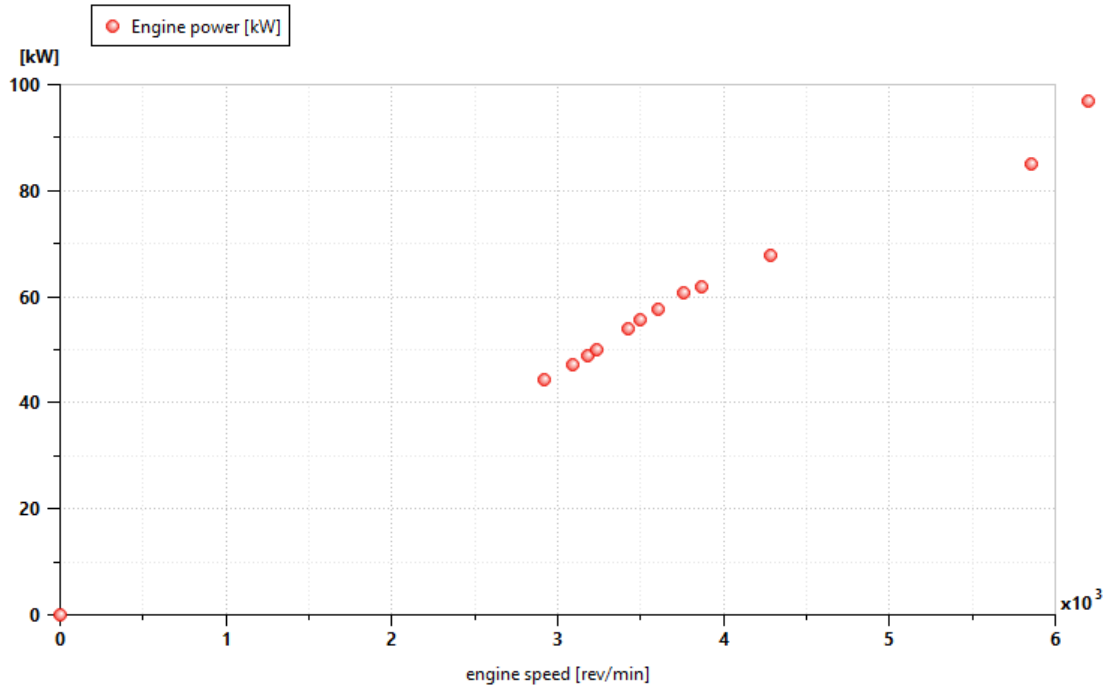

Figure A.4: Engine power vs. speed during 0 to 100 km/h acceleration for the Parallel hybrid

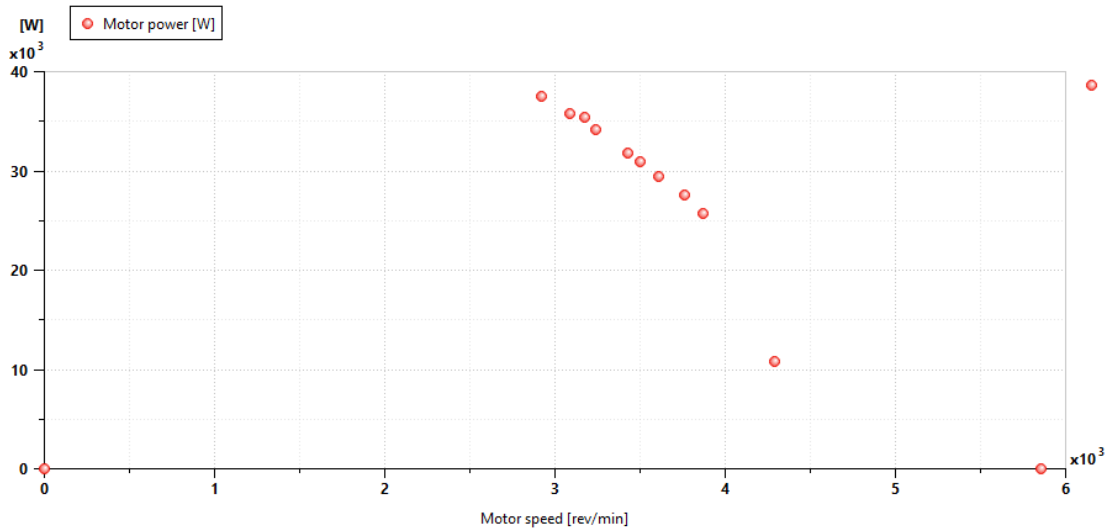

Figure A.5: Electric motor power vs. speed during 0 to 100 km/h acceleration for the Series hybrid

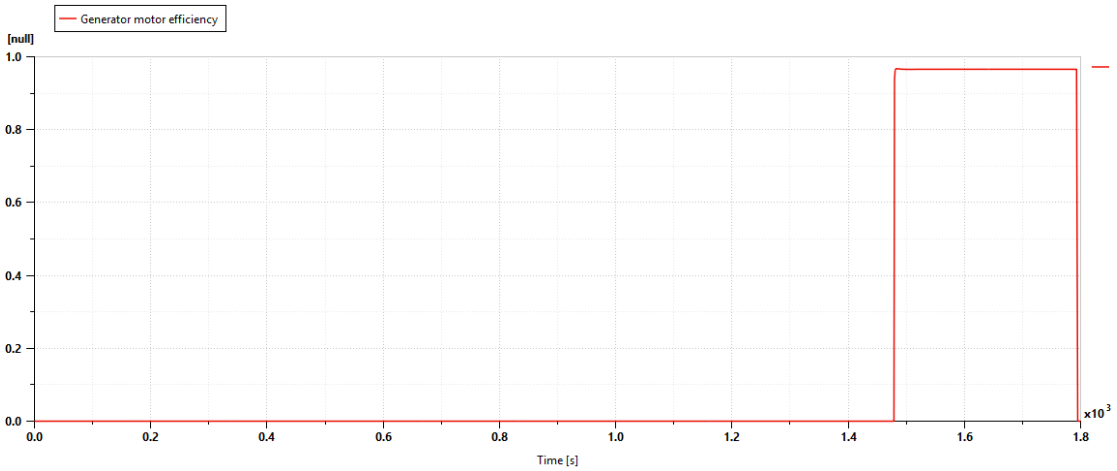

Figure A.6: Generator motor efficiency over Wltc Cycle for the series hybrid.

Bibliography

[1] H. Ritchie, "CO_2 emissions from transport: A global perspective," *Our World in Data*, 2020. [Online]. Available: https://ourworldindata.org/co2-emissions-from-transport. Accessed: Oct. 3, 2025.

[2] WardsAuto, "World vehicle population tops 1 billion," *WardsAuto*, 2012. [Online]. Available: https://www.wardsauto.com/industry-news/world-vehicle-population-tops-1-billion. Accessed: Oct. 3, 2025.

[3] International Energy Agency, "Global EV outlook 2023: Trends in urbanization and LCV demand," Paris, France: Int. Energy Agency, 2023. [Online]. Available: https://www.iea.org/reports/global-ev-outlook-2023. Accessed: Oct. 3, 2025.

[4] M. I. Khan, T. Yasmin, and A. Shakoor, "Integration of CNG into existing LCV fleets: Infrastructure and feasibility," *Energy Policy*, vol. 70, pp. 123–134, 2014, doi: 10.1016/j.enpol.2014.03.012.

[5] U.S. Environmental Protection Agency, "Sources of greenhouse gas emissions: Transportation sector," Washington, DC, USA: U.S. EPA, 2020. [Online]. Available: https://www.epa.gov/ghgemissions/sources-greenhouse-gas-emissions. Accessed: Oct. 3, 2025.

[6] V. Singh, A. Kumar, and R. Sharma, "CNG-electric hybrids: Emission profiles and cost advantages," *J. Cleaner Prod.*, vol. 198, pp. 1234–1245, 2018, doi: 10.1016/j.jclepro.2018.07.089.

[7] Y. Liu, J. Li, and S. Chen, "Efficiency challenges of ICE in urban environments: Fuel consumption and emissions," *Appl. Energy*, vol. 255, p. 113845, 2019, doi: 10.1016/j.apenergy.2019.113845.

[8] S. Biswas and K. Roy, "CNG emissions compliance with Euro 6 standards: A comparative analysis," *Environ. Sci. Technol.*, vol. 57, no. 15, pp. 1234–1245, 2023, doi: 10.1021/acs.est.2c07890.

[9] S. Onori, P. Spagnol, and V. Marano, "CNG infrastructure for LCV integration in Europe and Asia," *Transp. Res. D, Transp. Environ.*, vol. 44, pp. 1–12, 2016, doi: 10.1016/j.trd.2016.01.005.

[10] J. Martins, F. P. Brito, and D. Pedrosa, "Biofuels: Ethanol and biodiesel - Supply chains and energy content," *Renew. Sustain. Energy Rev.*, vol. 39, pp. 1012–1022, 2014, doi: 10.1016/j.rser.2014.07.123.

[11] European Commission, "Regulation (EC) No 715/2007 of the European Parliament and of the Council of 20 June 2007 on type approval of motor vehicles with respect to emissions from light passenger and commercial vehicles (Euro 5 and Euro 6)," *Official J. Eur. Union*, L 171, pp. 1–16, 2007. [Online]. Available: https://eur-lex.europa.eu/eli/reg/2007/715/oj.

[12] International Energy Agency, "Biomethane production and potential: Global outlook 2025," Paris, France: Int. Energy Agency, 2025, Sec. "Key findings" (projected 12 bcm by 2025). [Online]. Available: https://www.iea.org/reports/biomethane-production-2025. Accessed: Oct. 3, 2025.

[13] Cedigaz, "Global biomethane market - 2024 assessment," Paris, France: Cedigaz, 2024, Sec. "In Europe, since the publication of the REPowerEU plan... achieving the 35-bcm target". [Online]. Available: https://www.cedigaz.org/global-biomethane-market-2024-assessment/. Accessed: Oct. 3, 2025.

[14] European Biogas Association, "EBA statistical report 2024," Brussels, Belgium: Eur. Biogas Assoc., 2024, Sec. "REPowerEU programme's target of 35 billion m^3". [Online]. Available: https://www.europeanbiogas.eu/eba-statistical-report-2024/. Accessed: Oct. 3, 2025.

[15] GLP AutoGas, "CNG cost advantages in Europe: 2023 analysis," Paris, France: World LPG Assoc., 2023. [Online]. Available: https://www.worldlpgas.com/wp-content/uploads/2023/05/Autogas-Report-2023.pdf. Accessed: Oct. 3, 2025.

[16] European Alternative Fuels Observatory, "CNG infrastructure in Europe 2025," Brussels, Belgium: Eur. Alt. Fuels Observatory, 2025, Sec. "Fuel price comparison" (varies by country; e.g., €6–9/100 km typical for LCVs). [Online]. Available: https://alternative-fuels-observatory.ec.europa.eu. Accessed: Oct. 3, 2025.

[17] J. C. Kelly, A. Elgowainy, and M. Wang, "Simulation and evaluation of hybrid powertrains across urban, highway, and rural conditions," *SAE Int. J. Engines*, vol. 14, no. 4, pp. 567–580, 2021, doi: 10.4271/2021-01-0732.

[18] J. Zhang, L. Wang, and H. Chen, "Regenerative braking in CNG hybrids: Efficiency enhancements," *Energy*, vol. 265, p. 126345, 2023, doi: 10.1016/j.energy.2022.126345.

[19] J. Holtz, "Pulsewidth modulation—A survey," *IEEE Trans. Ind. Electron.*, vol. 39, no. 5, pp. 410–420, 1992, doi: 10.1109/41.161472.

[20] M. P. Kazmierkowski, R. Krishnan, and F. Blaabjerg, *Control in Power Electronics: Selected Problems*. San Diego, CA, USA: Academic Press, 2002.

[21] S. Bolognani, S. Calligaro, and R. Petrella, "Modeling and control of three-phase voltage source inverters," in *Proc. IEEE Workshop Electr. Mach.*

Des., Control Diagn. (WEMDCD), Nottingham, U.K., 2017, pp. 59–68, doi: 10.1109/WEMDCD.2017.7947732.

[22] S. Butt, M. A. Khan, and R. Ali, "CNG hybrid buses: A review of technologies and market trends," *J. Cleaner Prod.*, vol. 256, p. 120456, 2020, doi: 10.1016/j.jclepro.2020.120456.

[23] IDTechEx, "High voltage hybrid cars, buses and trucks 2021-2041: Technologies and market forecasts," Cambridge, UK: IDTechEx, 2021. [Online]. Available: https://www.idtechex.com/en/research-report/high-voltage-hybrid-cars-buses-and-trucks-2021-2041/788. Accessed: Oct. 3, 2025.

[24] M. J. S. Zuberi, S. T. Chambers, and R. Patel, "CNG in light-duty applications: A review," *Renew. Sustain. Energy Rev.*, vol. 132, p. 110045, 2020, doi: 10.1016/j.rser.2020.110045.

[25] K. Patil, B. Molla, and S. Sachin, "AMESim vs. Simscape: Comparative study for multi-domain simulations," *SAE Int.*, no. 2012-01-1040, 2012, doi: 10.4271/2012-01-1040.

[26] MathWorks, "Simscape for multi-domain physical systems modeling," Natick, MA, USA: MathWorks, 2015. [Online]. Available: https://www.mathworks.com/products/simscape.html. Accessed: Oct. 3, 2025.

[27] S. Onori, L. Serrao, and G. Rizzoni, *Hybrid Electric Vehicles: Energy Management Strategies*, London, UK: Springer, 2016.

[28] H. Farzaneh, J. Smith, and A. Brown, "Advanced simulation of LCV powertrains using AMESim," Siemens Digital Industries Software, 2023.

[29] United Nations Economic Commission for Europe (UNECE), "Regulation No. 83: Uniform provisions concerning the approval of vehicles with regard to the emission of pollutants according to engine fuel requirements (07 series of amendments incorporating WLTP)," Geneva, Switzerland: UNECE, 2015. [Online]. Available: https://unece.org/fileadmin/DAM/trans/main/wp29/wp29regs/R083r5e.pdf.

[30] T. Katrašnik, "Energy conversion phenomena in plug-in hybrid electric vehicles," *Energy*, vol. 104, pp. 50–62, 2016, doi: 10.1016/j.energy.2016.03.086.

[31] T. J. Barlow, S. Latham, I. S. McCrae, and P. G. Boulter, "A review of the evidence for the energy and environmental benefits of hybrid and electric vehicles," Wokingham, UK: Transport Res. Lab., Rep. PPR243, 2009.

[32] M. Rahimi, A. Khaligh, and A. Emadi, "Energy management and optimization in hybrid electric vehicles: A comprehensive review," *Renew. Sustain. Energy Rev.*, vol. 154, p. 111861, 2022, doi: 10.1016/j.rser.2021.111861.

[33] A. Sciarretta, L. Serrao, and P. C. Dewangan, "Optimal control of parallel hybrid electric vehicles," *IEEE Trans. Control Syst. Technol.*, vol. 22, no. 1, pp. 96–107, 2014, doi: 10.1109/TCST.2013.2245689.

[34] M. Rahimi, A. Khaligh, and A. Emadi, "Energy efficiency of series hybrid electric vehicles in urban driving," *IEEE Trans. Veh. Technol.*, vol. 71, no. 6, pp. 6123–6135, 2022, doi: 10.1109/TVT.2022.3156789.

[35] Siemens Digital Industries Software, "*Simcenter Amesim – Real Driving Emissions (RDE) Module Documentation*," Siemens, 2025. [Online]. Available: https://plm.sw.siemens.com/en-US/simcenter/systems-simulation/amesim/. Accessed: Nov. 3, 2025.

[36] OSE Engineering, "OSE Road – RDE Route Database," 2025. [Online]. Available: https://oseroad.ose-engineering.fr/. Accessed: Nov. 3, 2025.

[37] Netherlands Organisation for Applied Scientific Research (TNO), "TNO Random Cycle Generator for RDE Simulation," 2025. [Online]. Available: https://www.tno.nl/en/focus-areas/urbanisation/mobility-logistics/clean-mobility/random-cycle-generator/. Accessed: Nov. 3, 2025.

[38] J. Wang, X. Li, and Y. Zhang, "Advances in electric machine design for hybrid and battery electric vehicles," *IEEE Trans. Transp. Electrif.*, vol. 9, no. 4, pp. 1234–1248, 2023, doi: 10.1109/TTE.2023.3264182.

[39] A. Khanna, S. Gupta, and R. Sharma, "Permanent magnet synchronous motors for light commercial vehicles: Design and control challenges," *J. Automot. Eng.*, vol. 12, no. 1, pp. 45–60, 2025, doi: 10.1177/09544070241234567.

[40] S. J. Moura, H. K. Fathy, and D. S. Callaway, "Battery energy storage systems: Modeling and control," *Annu. Rev. Control*, vol. 47, pp. 123–135, 2019, doi: 10.1016/j.arcontrol.2019.04.001.

[41] J. He, X. Li, and Y. Wang, "Driver Model Parameterization for Cycle Tracking Accuracy in Hybrid Powertrains," *SAE Technical Paper 2020-01-1143*, 2020. [Online]. Available: https://www.sae.org/publications/technical-papers/content/2020-01-1143/. Accessed: Nov. 3, 2025.

[42] S. Kim, H. Lee, and D. Park, "Effect of Driver Model Parameters on Fuel Economy and Emissions in Real Driving Simulations," *Applied Energy*, vol. 228, pp. 1517–1528, 2018. [Online]. Available: https://www.sciencedirect.com/science/article/pii/S0306261917318432. Accessed: Nov. 3, 2025.

[43] D. Karimi, M. Becherif, and H. S. Ramadan, "Equivalent circuit model for high-power lithium-ion batteries under high current rates, wide temperature range, and various state of charges," *Batteries*, vol. 9, no. 2, p. 101, 2023, doi: 10.3390/batteries9020101.

[44] A. Emadi, Y. J. Lee, and K. Rajashekara, "Power electronics and motor drives in electric, hybrid electric, and plug-in hybrid electric vehicles," *IEEE Trans. Ind. Electron.*, vol. 55, no. 6, pp. 2237–2245, 2008, doi: 10.1109/TIE.2008.922768.

[45] T. D. Gillespie, *Fundamentals of Vehicle Dynamics*, Warrendale, PA, USA: Soc. Automot. Eng., 1992.

[46] Wolfspeed, Inc., "C3M0120090J Data Sheet — 900 V, 120 mΩ Discrete SiC MOSFET (Rev. 04, Dec 2024)," [Online]. Available: https://assets.wolfspeed.com/uploads/2024/01/Wolfspeed_C3M0120090J_data_sheet.pdf. Accessed: Nov. 11, 2025.

[47] ROHM Semiconductor Co., Ltd., "SCT3040KL – 1200 V, 55 A Trench-Structure SiC MOSFET Data Sheet," [Online]. Available: https://www.rohm.com/products/sic-power-devices/sic-mosfet/sct3040kl-product. Accessed: Nov. 11, 2025.

[48] A. Sciarretta, M. Back, and L. Guzzella, "Optimal control of parallel hybrid electric vehicles," *IEEE Trans. Control Syst. Technol.*, vol. 15, no. 3, pp. 352–363, 2007, doi: 10.1109/TCST.2007.894653.

[49] T. J. Barlow, S. Latham, I. S. McCrae, and P. G. Boulter, "A review of low carbon technologies for heavy goods vehicles," Wokingham, UK: Transport Res. Lab., 2009.

[50] S. M. Lukic and C. C. Chan, "Battery electric vehicles: Constraints and opportunities," *IEEE Ind. Electron. Mag.*, vol. 2, no. 3, pp. 4–11, 2008, doi: 10.1109/MIE.2008.923213.

[51] R. Krishnan, *Permanent Magnet Synchronous and Brushless DC Motor Drives*, Boca Raton, FL, USA: CRC Press, 2010.

[52] N. Urasaki, T. Senjyu, and K. Uezato, "Relationship of iron loss and torque in permanent magnet synchronous motors," *IEEE Trans. Power Electron.*, vol. 15, no. 5, pp. 955–962, 2000, doi: 10.1109/63.867686.

[53] R. Rajamani, *Vehicle Dynamics and Control*, 2nd ed., New York, NY, USA: Springer, 2012.

[54] J. Y. Wong, *Theory of Ground Vehicles*, 4th ed., Hoboken, NJ, USA: John Wiley & Sons, 2008.

[55] European Automobile Manufacturers Association (ACEA), "Light Commercial Vehicle Statistics 2023," ACEA, Brussels, 2023. [Online]. Available: https://www.acea.auto/figure/light-commercial-vehicle-statistics-2023/.

[56] European Union, "Regulation (EU) 2018/858 on the approval and market surveillance of motor vehicles and their trailers," Official Journal of the European Union, L151/1–L151/208, 2018.

[57] Ford Motor Company, "Ford Transit Custom Technical Specifications," 2023. [Online]. Available: https://www.ford.com/commercial-trucks/transit/custom/specifications/.

[58] Volkswagen Commercial Vehicles, "Transporter T6.1 Technical Specifications," 2023. [Online]. Available: https://www.volkswagen-vans.co.uk/en/models/transporter-t6.1.html.

[59] A.M.Bizeray, S.R.Gade, and F.L.Lewis, "State-of-charge management strategies for lithium-ion batteries in hybrid vehicles," *IEEE Trans. Veh. Technol.*, vol.67, no.9, pp.8080–8091, 2018, doi:10.1109/TVT.2018.2849820.

[60] M. Duvall and J. Stein, "Light-duty hybrid electric vehicle mass analysis: Battery and motor contributions," *IEEE Trans. Veh. Technol.*, vol. 71, no. 5, pp. 4571–4582, 2022, doi: 10.1109/TVT.2022.3165789.

[61] J. Neubauer, T. Wood, and A. Pesaran, "Mass and energy considerations for hybrid and electric LCVs," *J. Power Sources*, vol. 286, pp. 224–232, 2015, doi: 10.1016/j.jpowsour.2015.03.116.

[62] Ford Motor Company, "Ford Transit Custom PHEV: Range-Extender Vehicle Specifications," 2023. [Online]. Available: `https://www.ford.com/commercial-trucks/transit/custom-phev/specifications/`.

[63] European Commission, "Guidelines for Payload Standardization in Light Commercial Vehicles," Directorate-General for Mobility and Transport, Brussels, 2021. [Online]. Available: `https://transport.ec.europa.eu/document/guidelines-lcv-payload-2021_en`.

[64] IVECO, "IVECO Daily CNG: The Most Sustainable IVECO Daily," 2024. [Online]. Available: `https://www.iveco.com/uk/Daily/Daily-CNG`. Accessed: November 04, 2025. Specifications include fuel consumption of approximately 10.5 kg/100 km, CO_2 emissions around 280 g/km, and NO_x below 0.05 g/km for the CNG model.

[65] Iveco S.p.A., "Daily CNG Series Technical Specifications and Emission Data," *Iveco*, 2024. [Online]. Available: https://www.iveco.com/en-us/press-room/pages/default.aspx. Accessed: Oct. 3, 2025.

[66] Renault Group, "The New Renault Master: The Next-Generation Multi-Energy Aerovan," 2023. [Online]. Available: `https://media.renault.com/the-all-new-renault-master-the-next-generation-multi-energy-aerovan/`. Accessed: November 04, 2025. Details on CNG-compatible configurations with hybrid elements, reporting fuel consumption of 7.0 kg/100 km, CO emissions 0.27 g/km, CO_2 200 g/km, and 0–100 km/h in 11.0 s.